AD-754 449

MIXED PHASE EFFECTS IN ALUMINUM

Vernon L. Bailey, et al

Physics International Company

Prepared for:

Defense Nuclear Agency

January 1973

DNA 2992F
PIFR-246

MIXED PHASE EFFECTS IN ALUMINUM

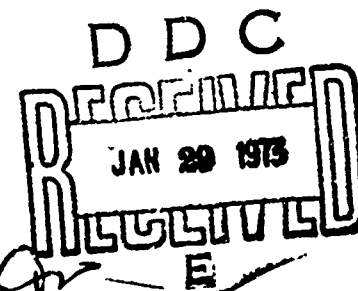# FINAL REPORT

January 1973

by
Vernon L. Bailey and Andrew Lutze

Prepared for

Defense Nuclear Agency
Washington, D.C. 30205

Under Contract No. DASA-01-70-C-0114

Approved for public release;
distribution unlimited.

Details of illustrations in
this document may be better
studied on microfiche

PHYSICS INTERNATIONAL COMPANY
2700 MERCED STREET • SAN LEANDRO • PHONE 357-4610 (415) • TWX 891-9689 (415)

DOCUMENT CONTROL DATA - R&D		
(Security classification of title, body of abstract and indexing annotation must be entered when the overall report is classified)		

1 ORIGINATING ACTIVITY (Corporate author)	2a REPORT SECURITY CLASSIFICATION
Physics International Company 2700 Merced Street San Leandro, California 94577	Unclassified
	2b GROUP

3 REPORT TITLE

Mixed Phase Effects in Aluminum

4 DESCRIPTIVE NOTES (Type of report and inclusive dates)

Final Report, April 15, 1970 through October 31, 1972

5 AUTHOR(S) (Last name, first name, initial)

Bailey, Vernon L. and Lutze, Andrew

6 REPORT DATE	7a. TOTAL NO. OF PAGES	7b. NO. OF REFS
January 1973	~~185~~ 188	15

8a CONTRACT OR GRANT NO.	9a. ORIGINATOR'S REPORT NUMBER(S)
DASA-01-70-C-0114	
b PROJECT NO. NWER Code: A	PIFR-246
c Task and Subtask Code: C321	9b OTHER REPORT NO(S) (Any other numbers that may be assigned this report)
d Work Unit Code: 09	DNA 2992F

10 AVAILABILITY/LIMITATION NOTICES

Approved for public release; distribution unlimited.

11 SUPPLEMENTARY NOTES	12. SPONSORING MILITARY ACTIVITY
Details of illustrations in this document may be better studied on microfiche	Director Defense Nuclear Agency Washington, D. C. 20305

13 ABSTRACT A combined experimental and theoretical investigation of the radiation-induced impulse and stress generation characteristics of aluminum has been carried out for cases where a significant portion of the blowoff material was in the liquid-vapor state. Intense pulsed electron beams were used as a source of rapid (50 nsec) high-energy-density loading to produce mixed-phase effects in aluminum. Impulse measurements were obtained with a ballistic pendulum for peak doses of up to 3800 cal/gm. Manganin gauges and the laser interferometer were used to obtain stress time records adjacent to the region of energy deposition.

A detailed comparison of the PUFF-V, GRAY, and PHILCO-FORD equation-of-state models was carried out for aluminum. The experimental data were compared with the predictions of the LINEAR FLUID, PUFF-V, GRAY, and PHILCO-FORD equation-of-state models. The PHILCO-FORD equation-of-state model gave the best data representation. The PUFF-V model, which includes a vapor state, and the LINEAR-FLUID model, which does not, gave approximately the same results for the same input conditions. For the experimental conditions obtained, the impulse in aluminum was dominated by the behavior of the equation of state of aluminum in the liquid region.

The laser interferometer data for the high-fluence conditions and the predictions of the GRAY equation-of-state model suggested the possible existence of a double wave structure in the propagated stress

DD FORM **1473**
1 JAN 64

ABSTRACT (cont.)

pulse. This phenomenon was attributed to the recompression of the
liquid layer by the overlying vapor layer after the initial drop
to zero pressure in the liquid.

KEY WORDS	LINK A		LINK B		LINK C	
	ROLE	WT	ROLE	WT	ROLE	WT
Impulse						
Stress generation						
Equation of state						
Mixed-phase						
Electron beams						
Rapid energy deposition						
Aluminum						
Hydrodynamic codes						

INSTRUCTIONS

1. ORIGINATING ACTIVITY: Enter the name and address of the contractor, subcontractor, grantee, Department of Defense activity or other organization (corporate author) issuing the report.

2a. REPORT SECURITY CLASSIFICATION: Enter the overall security classification of the report. Indicate whether "Restricted Data" is included. Marking is to be in accordance with appropriate security regulations.

2b. GROUP: Automatic downgrading is specified in DoD Directive 5200.10 and Armed Forces Industrial Manual. Enter the group number. Also, when applicable, show that optional markings have been used for Group 3 and Group 4 as authorized.

3. REPORT TITLE: Enter the complete report title in all capital letters. Titles in all cases should be unclassified. If a meaningful title cannot be selected without classification, show title classification in all capitals in parenthesis immediately following the title.

4. DESCRIPTIVE NOTES: If appropriate, enter the type of report, e.g., interim, progress, summary, annual, or final. Give the inclusive dates when a specific reporting period is covered.

5. AUTHOR(S): Enter the name(s) of author(s) as shown on or in the report. Enter last name, first name, middle initial. If military, show rank and branch of service. The name of the principal author is an absolute minimum requirement.

6. REPORT DATE: Enter the date of the report as day, month, year; or month, year. If more than one date appears on the report, use date of publication.

7a. TOTAL NUMBER OF PAGES: The total page count should follow normal pagination procedures, i.e., enter the number of pages containing information.

7b. NUMBER OF REFERENCES: Enter the total number of references cited in the report.

8a. CONTRACT OR GRANT NUMBER: If appropriate, enter the applicable number of the contract or grant under which the report was written.

8b, 8c, & 8d. PROJECT NUMBER: Enter the appropriate military department identification, such as project number, subproject number, system numbers, task number, etc.

9a. ORIGINATOR'S REPORT NUMBER(S): Enter the official report number by which the document will be identified and controlled by the originating activity. This number must be unique to this report.

9b. OTHER REPORT NUMBER(S): If the report has been assigned any other report numbers (either by the originator or by the sponsor), also enter this number(s).

10. AVAILABILITY/LIMITATION NOTICES: Enter any limitations on further dissemination of the report, other than those imposed by security classification, using standard statements such as:

(1) "Qualified requesters may obtain copies of this report from DDC."

(2) "Foreign announcement and dissemination of this report by DDC is not authorized."

(3) "U. S. Government agencies may obtain copies of this report directly from DDC. Other qualified DDC users shall request through

_____."

(4) "U. S. military agencies may obtain copies of this report directly from DDC. Other qualified users shall request through

_____."

(5) "All distribution of this report is controlled. Qualified DDC users shall request through

_____."

If the report has been furnished to the Office of Technical Services, Department of Commerce, for sale to the public, indicate this fact and enter the price, if known.

11. SUPPLEMENTARY NOTES: Use for additional explanatory notes.

12. SPONSORING MILITARY ACTIVITY: Enter the name of the departmental project office or laboratory sponsoring (paying for) the research and development. Include address.

13. ABSTRACT: Enter an abstract giving a brief and factual summary of the document indicative of the report, even though it may also appear elsewhere in the body of the technical report. If additional space is require a continuation sheet shall be attached.

It is highly desirable that the abstract of classified reports be unclassified. Each paragraph of the abstract shall end with an indication of the military security classification of the information in the paragraph, represented as (TS) (S) (C) or (U)

There is no limitation on the length of the abstract. However, the suggested length is from 150 to 225 words.

14. KEY WORDS: Key words are technically meaningful terms or short phrases that characterize a report and may be used as index entries for cataloging the report. Key words must be selected so that no security classification is required. Identifiers, such as equipment model designation, trade name, military project code name, geographic location, may be used as key words but will be followed by an indication of technical context. The assignment of links, roles, and weights is optional.

MIXED PHASE EFFECTS IN ALUMINUM

FINAL REPORT

January 1973

by

Vernon L. Bailey and Andrew Lutze

Prepared for

Defense Nuclear Agency
Washington, D.C. 30205

Under Contract No. DASA-01-70-C-0114

Preparing Agency

Physics International Company
2700 Merced Street
San Leandro, California 94577

ABSTRACT

A combined experimental and theoretical investigation of the radiation-induced impulse and stress generation characteristics of aluminum has been carried out for cases where a significant portion of the blowoff material was in the liquid-vapor state. Intense pulsed electron beams were used as a source of rapid (50 nsec) high-energy-density loading to produce mixed-phase effects in aluminum. Impulse measurements were obtained with a ballistic pendulum for peak doses of up to 3800 cal/gm. Manganin gauges and the laser interferometer were used to obtain stress time records adjacent to the region of energy deposition.

A detailed comparison of the PUFF-V, GRAY, and PHILCO-FORD equation-of-state models was carried out for aluminum. The experimental data were compared with the predictions of the LINEAR FLUID, PUFF-V, GRAY, and PHILCO-FORD equation-of-state models. The PHILCO-FORD equation-of-stat   del gave the best data représentation. The PUFF-V model, which includes a vapor state, and the LINEAR-FLUID model, which does not, gave approximately the same results for the same input conditions. For the experimental conditions obtained, the impulse in aluminum was dominated by the behavior of the equation of state of aluminum in the liquid region.

The laser interferometer data for the high-fluence conditions and the predictions of the GRAY equation-of-state model suggested the possible existence of a double wave structure in the propagated stress pulse. This phenomenon was attributed to the recompression of the liquid layer by the overlying vapor layer after the initial drop to zero pressure in the liquid.

CONTENTS

CONTENTS (cont.)

ILLUSTRATIONS

ILLUSTRATIONS (cont.)

ILLUSTRATIONS (cont.)

TABLES

SECTION 1

INTRODUCTION

The response of materials to rapid energy deposition is a complex process which depends on a combination of physical phenomena. The rapid energy deposition can be the result of a nuclear explosion, deposition of electrons by intense electron beams, or the heating and compression of a D-T pellet by pulsed laser irradiation for controlled thermonuclear fusion applications. All of these energy sources are capable now or in the near future of providing internal energy densities in excess of the vaporization energy of most materials. The characteristic heating time for these sources can vary from a few tens of pico-seconds to a few hundred nanoseconds.

The ability to predict and understand the response of materials to rapid energy deposition depends strongly on having an equation of state of the material that is able to follow the series of thermodynamic states through which the material passes both during and after the rapid energy deposition. The rapid heating combined with high internal energy densities can result in pressures in the megabar range and temperatures on the order of up to a few electron volts. When the material expands adia-batically from the initial high-temperature high-pressure state after energy deposition, the density, pressure, and temperature drop. The equation of state in this expanded volume region is important in determining the impulse* imparted to the material as a result of the rapid energy deposition.

_____

*As used throughout this report, impulse is defined as change in momentum per unit area.

1

Uncertainties in the equation-of-state models in the expanded volume region can lead to large differences in impulse calculations. Unfortunately there are no good experimental data available in the expanded volume region of most materials on which to base an equation-of-state model.

The objective of this work was to experimentally and theoretically investigate the impulse and stress generation characteristics of aluminum that are the result of rapid energy deposition of internal energy densities in excess of the vaporization enthalpy of aluminum at one atmosphere. For this condition a significant portion of the blowoff material was in the liquid-vapor state. This work is an extension of that reported in DASA-2596, Equation of State Evaluation, April 1972, DASA-2475, Melt Dominated Impulse Experiments and Calculations, September 1970. The purpose of the program was to investigate the contribution of material in the liquid-vapor state to the material response of aluminum. The experimental data were intended to provide a data base for the evaluation of existing multi-phase equation-of-state models and provide a basis for making appropriate modifications of the multi-phase equations of state when indicated by the data.

Aluminum was used as a sample material for several reasons: 1) it is a relatively easy-to-obtain, inexpensive metal and 2) it has no major solid-solid phase transitions, nor is it particularly rate-sensitive.

Intense pulsed electron beams were used as the source of rapid (50 nsec) high-energy-density loading to produce mixed-phase effects in aluminum.

SECTION 2

EXPERIMENTAL PROCEDURES AND RESULTS

The experimental procedures and results are presented in this section. Description of electron beam diagnostics will not be discussed in detail here since an adequate account appears in Reference 1. However, a discussion of the backscatter correction to measured total beam energy is given in Appendix A. The backscatter correction was applied to the data in this program.

Metallic beam guides, vented to reduce spurious impulse from anode debris, will be discussed here.

Material response data, consisting of impulse, stress histories and mass loss, taken over a peak dose range from 300 to 3800 cal/gm, will comprise the bulk of this section.

2.1 BEAM TRANSPORT AND SPURIOUS IMPULSE

High-current electron beams generated by Physics International's Model 738 Pulserad were used to irradiate aluminum samples. Dynamic loads were induced in the test material by rapid deposition of electrons (50 nsec FWHM of beam power curve) in the front surface of targets. Peak energy dose levels were varied from 300 to 3800 cal/gm by changing the intensity (fluence) of 200 to 400 keV mean electron energy beams. Active beam diagnostics, described in Reference 1, were

3

used to characterize the electron beam environment and to compute energy deposition as a function of material depth.

Peak dose in the material was varied by changing the electron beam fluence. The method of varying fluences for a specified mean electron energy (and hence, for fixed total beam calories) consists of concentrating the total calories in the beam, H, into different uniform irradiation areas, $\bar{A}$. The test matrix specified the mean electron energy and the fluence. For a given mean electron energy the total machine output in calories is fixed. Therefore, the required irradiation area was then determined by $\bar{A} = H/\bar{\Phi}$.

Metallic beam guides and gas focusing were used for beam transport and fluence control. Background gas pressure in the electron beam drift chamber governs the magnitude of the net current and hence the degree of beam pinching due to self-magnetic fields. Metallic guide cones were used to shape the gaussian fluence at the anode into a uniform distribution over the sample placed at the cone exit. Two beam guide geometries were used to achieve a broad range of fluences. The beam guide for low-to-medium fluences (approximately 10 to 50 cal/cm^2) was a 20-cm long, straight, stainless-steel cone with slotted walls (Figure 1). The high-fluence beam guide (Figure 2) consisted of a short, solid, graphite-lined, stainless-steel cone with a curved, slotted pipe attached to its exit.

4.4 cm

1.6 cm
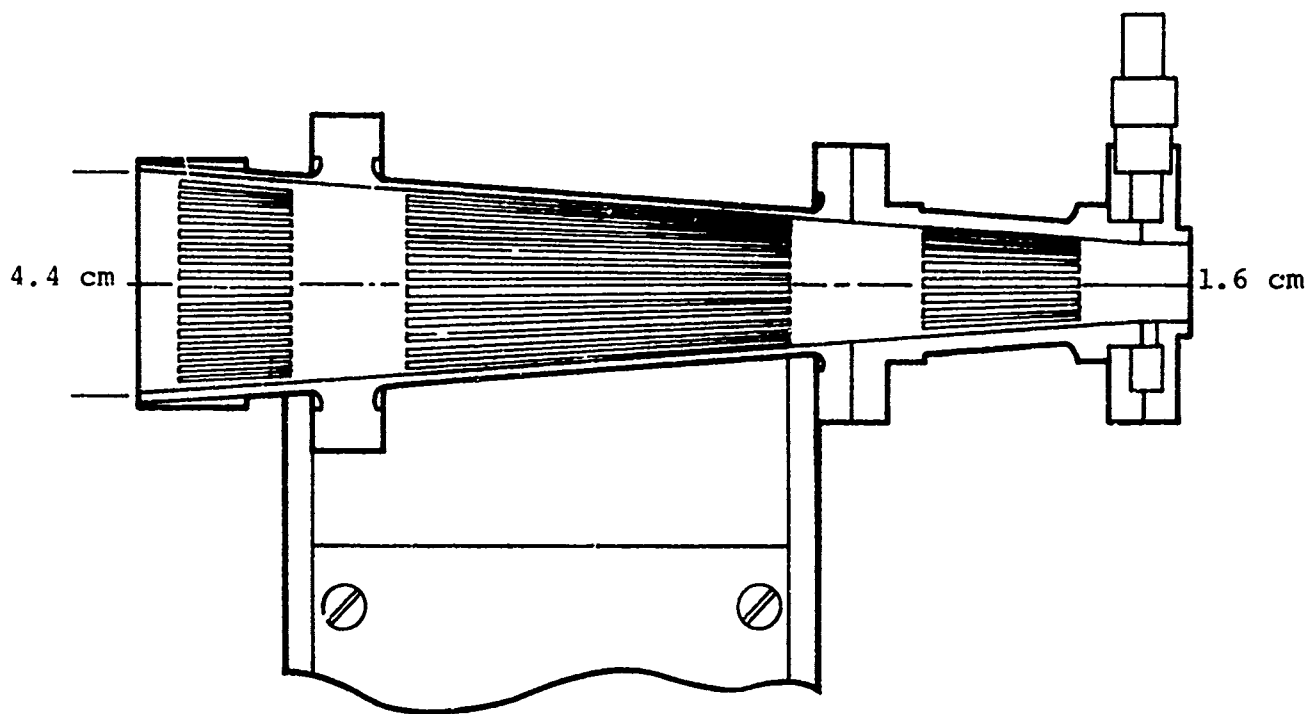
Figure 1   Beam guide cone.

5
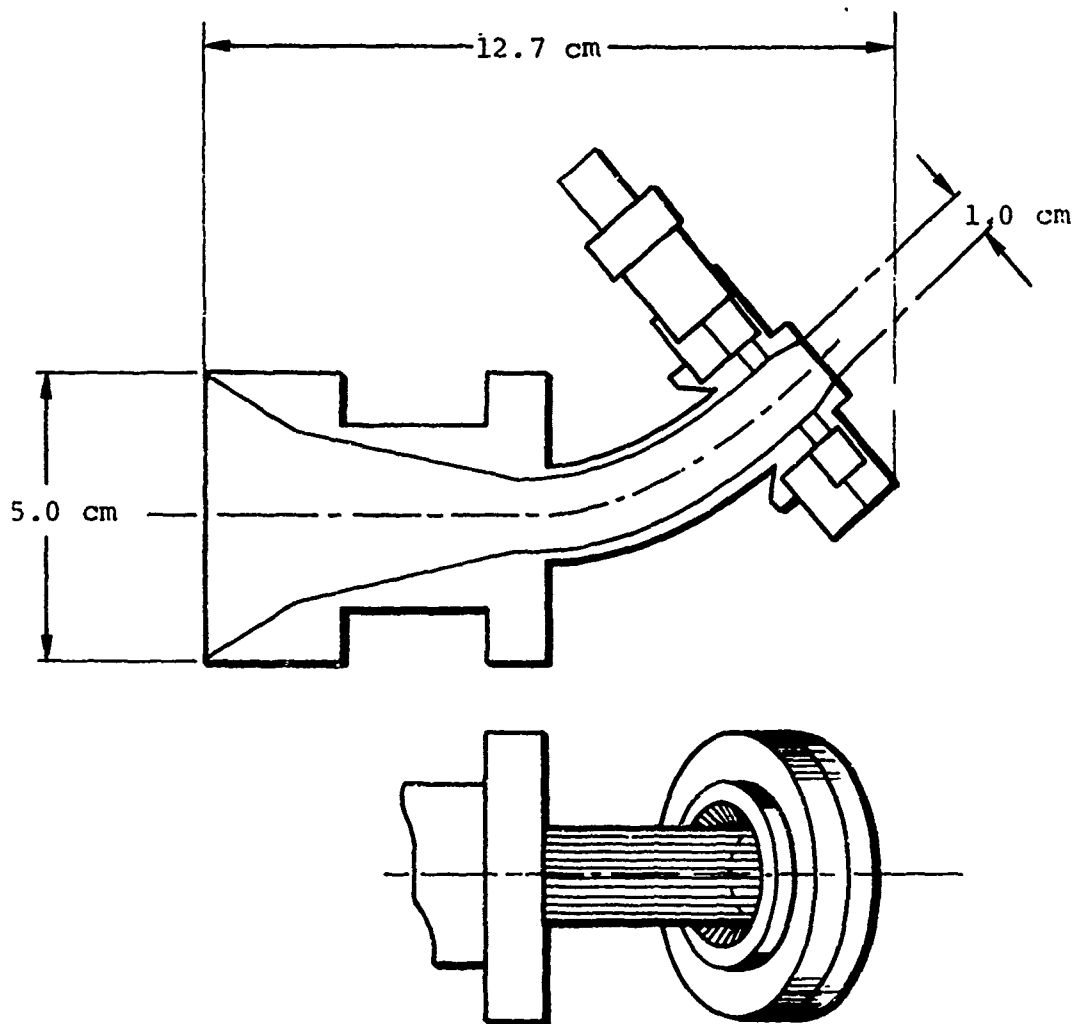
Figure 2   High-fluence beam guide.

6

The slots in the beam guide walls were designed to minimize spurious impulse from anode debris, the source of which will be discussed below. The location of slots in the low-to-medium fluence beam guide (Figure 1) needs no explanation. The function of the slotted pipe attached to the exit of the high-fluence beam guide was to bend the beam (through approximately 45 degrees) away from its original axis while allowing anode debris, collimated by the cone, to escape through the slots in the pipe walls.

The following experiments were performed to demonstrate the negligible anode-debris contribution to impulse.

The anode of the 738 Pulserad is a 1/4-mil sheet of aluminized Mylar. Anode material covering the injection area of the guide cones is vaporized on every shot because of energy deposition in the aluminized Mylar. Half of the vaporized mass of anode material expands into the drift chamber and hence into the guide cone. If the 0.01 gram of anode debris, moving at sufficient velocity, were to impact the sample in a pendulum bob at the end of the guide cone, the pendulum could record spurious impulse. Vented (i.e., slotted) beam guides have been used to demonstrate that the anode-debris-induced impulse level is less than 100 taps.

For the low-to-medium fluence beam guide, the beam environment chosen was one for which quartz gauge data for aluminum was available. These traces typically show triangular stress pulses with less than 0.2-μsec duration (base-to-base). Guided by these data, a 70-mil-thick aluminum disk (flier) was attached with a thin film of vacuum grease to the rear surface of a

7

larger diameter, 50-mil-thick aluminum disk (sample). This "sandwich" was placed in an annular pendulum bob, so that only the sample was held, while the flier was free to fly off unimpeded. The array was placed at the end of the straight, slotted guide cone used in low-to-medium fluence experiments (Figure 1). Each time beams were fired into such arrays, the fliers separated, while the bobs holding the samples showed zero deflection.

The separation time of the flier subsequent to electron beam deposition in the sample (sample thickness plus twice the flier thickness) was chosen to be 1.08 µsec. At the time of separation, the flier became a momentum trap capable of containing more than the measured stress pulse under similar beam conditions. Thus, 1.08 µsec after deposition time, the sample at the cone exit was in position to receive any spurious impulse and record it as a pendulum deflection. No deflections were recorded.

Arrival of anode debris at the sample in less than 1.08 µsec would require 40 times the available energy in the electron beam and would result in impulse levels an order of magnitude greater than the highest ever recorded at Physics International. Therefore, we concluded that no spurious impulse due to anode debris can occur less than 1.08 µsec after beam deposition time. Also, no measurable spurious impulse occurred after 1.08 µsec, at the exit of the 20-cm, slotted guide cone used for low-to-medium fluence material response experiments.

8

The absence of spurious impulse due to anode debris could not be demonstrated for the high-fluence beam guide in the same way as for the low-to-medium fluence guide cone. Since there is reason to expect long time impulse generation in aluminum for the liquid-vapor, mixed-phase regime, no criteria existed for a momentum trap thickness such that all the real impulse would be carried off by the flier well before possible anode debris arrival. The alternative demonstration consisted of firing a beam (less than 1000 cal/gm peak dose) into a graphite sample in the pendulum at the exit of the beam guide. No pendulum deflection was observed, suggesting that spurious impulse due to anode debris through the high-fluence beam guide is less than measurable by the ballistic pendulum used in this program.

2.2 IMPULSE MEASUREMENTS

The impulse data presented here were obtained using the ballistic pendulum technique described in Reference 1.

The linear fluid model of impulse generation in aluminum was shown to be valid in the melt-dominated regime (Reference 2). It states that

$$I = 0.04186 \ \frac{\Gamma}{2C_k} \ \phi \ \exp\left(- \ \frac{C_k \tau}{2R}\right) \tag{1}$$

where

I = impulse in ktap
C_k = bulk sound speed ($C_k = \sqrt{K/\rho_o}$) in cm/μsec
Γ = Gruneisen coefficient
ϕ = fluence in cal/cm^2

9

τ = deposition time in μsec

R = electron range in cm

K = adiabatic bulk modulus in mbar

ρ_o = density in gm/cm^3

Accordingly, the generated impulse depends, not only on fluence, but on deposition time and electron range as well, at least in the melt-dominated regime. The body of impulse data, in this program, was collected over a 200 to 400 keV mean electron energy spread with a corresponding spread of electron ranges in the test samples. Furthermore, since fluence control was achieved with gas focusing, the variation of background gas pressure introduced varied degrees of beam-front erosion (Reference 3). Consequently, the beam pulse (deposition time) at the sample location varied according to the gas pressure used to achieve the fluence. In short, each measurement of impulse can be expected to have its individual fluence, deposition time, and electron range. In these circumstances, the linear fluid model for melt-dominated impulse generation predicts an artificial scatter of the data when impulse is plotted versus only fluence--without regard to dependences on electron range (mean electron energy) and deposition time.

The preceding discussion was intended to support the view that a comparison of model predictions with impulse data, generated in electron beams, using impulse versus fluence plots as the arena of comparison is not appropriate. Such comparisons must be done on a point-by-point basis since each impulse measurement can have its individual set of loading conditions (e.g., fluence, energy deposition range and deposition time) on which impulse generation may depend. Therefore, a plot of

10

impulse versus fluence for the electron beam data does not give
a valid representation of the scatter in the data, and such
gr..phs can only be used to present general trends.

The data summary is shown in Table 1, and the notations
employed in it are as follows:

$\langle E \rangle$ = Mean electron energy (keV) calculated as
described in Reference 1.

$\langle \theta \rangle$ = Mean angle of incidence (degrees) of the beam
electrons from the calculation in Reference 3.

τ = Full width at half maximum (FWHM) of the power
curve.

H = Total beam calories impinging on target.

$\overline{A}$ = Crater (mass removal) area in the target (cm^2).

$\overline{\phi}$ = Average fluence (cal/cm^2) defined as $H/\overline{A}$.

$\Delta(MV)$ = Momentum change (kilo-dyne-sec) imparted to the
ballistic pendulum in which the target is
mounted.

$\overline{I}$ = Impulse per unit area (ktap) defined as $\Delta(MV)/\overline{A}$.

ΔM = Mass (gm) lost by the target.

Parentheses indicate approximate values. The peak dose in
the target was estimated by the product of fluence, $(\overline{\phi})$, and the
normalized peak dose characteristic of $\langle E \rangle$ and $\langle \theta \rangle$. It was
demonstrated in Reference 4 that $\langle E \rangle$ and $\langle \theta \rangle$ are sufficient to
identify the appropriate normalized energy deposition profile in
a material.

TABLE 1

DATA SUMMARY

Shot	$\langle E\rangle$ (keV)	$\langle\theta\rangle$ (°)	τ (nsec)	H (cal)	$\bar{A}$ (cm²)	$\bar{\phi}$ (cal/cm²)	Δ(MV) (kds)	I (ktap)	ΔM (gm)	Approx. Peak Dose (cal/gm)
12008	257	53	(55)	112	2.8 ±0.3	40±4	7.30	2.6±0.3	0.154	1000
12214	219	49	(55)	116	3.48±0.38	35±4	7.19	2.1±0.2	0.1381	1100
12217	220	50	(55)	88	2.97±0.67	30±6	5.44	1.8±0.4	0.1190	1000
12218	266	44	(55)	166	3.30±0.30	50±5	9.05	2.7±0.3	0.1544	1100
13550	353	60	(55)	183	4.0 ±0.4	46±5	13.17	3.3±0.3	0.242	800
13551	(386)	60	(55)	213	3.8 ±0.4	56±6	13.63	3.6±0.4	0.2411	800
13554	371	51	(55)	198	3.9 ±0.4	51±5	17.08	4.4±0.5	0.2788	800
13556	620	59	(55)	393	3.7 ±0.4	106±11	31.25	8.5±0.9	0.5366	1000
14010	348	43	36	138	1.05±0.25	132±30	12.60	12.0±3.0	---	2000
14011	296	40	35	122	0.9 ±0.2	136±40	8.56	9.5±3.0	---	2500
14012	289	44	34	95	0.8 ±0.2	120±30	6.14	7.7±2.0	---	2100
14013	303	38	35	98	1.2 ±0.2	82±15	7.31	6.1±0.8	---	1500
14016	290	39	35	95	1.10±0.3	86±30	7.07	6.4±2.0	---	1600
15041	402	50	55	201	3.87±0.32	52±4	12.34	3.2±0.3	0.2165	700
15165	(220)	37	56	28	1.97±0.4	14±3	0.60	0.6±0.1	0.0355	300
15393	275	58	51	159	2.85±0.20	56±4	9.40	3.3±0.3	0.1630	1400
15494	284	42	45	100	0.64±0.10	156±30	3.73	5.8±0.7	0.0330	3500
15497	329	47	43	156	0.74±0.20	211±40	7.95	10.1±2.0	0.0725	3800
15510	301	30	38	66	1.83±0.30	36±5	5.30	2.9±0.4	0.0855	600
15511	317	33	51	119	1.24±0.20	96±20	6.73	5.4±1.0	0.0797	1400
15593	220	36	67	33	0.6 ±0.1	14±2	0.34	0.3±0.05	0.0145	400
15595	212	36	66	32	0.9 ±0.1	11±1	0.33	0.3±0.05	0.0160	300
17608	264	58	28	107	0.9 ±0.1	126±15	4.30	4.5±0.5	0.0470	3200
17609	293	59	34	121	0.9 ±0.1	134±20	5.50	6.1±0.9	0.0663	3400
17610	(268)	51	34	97	0.7 ±0.1	138±30	4.70	6.7±1.0	0.0428	3300

12

2.3 STRESS MEASUREMENTS

The laser interferometer and the manganin gauge techniques which were used to record stress histories at the rear surface of samples are described in Appendices B and C, respectively.

The geometry of the manganin foil gauges is illustrated in Figure 3.
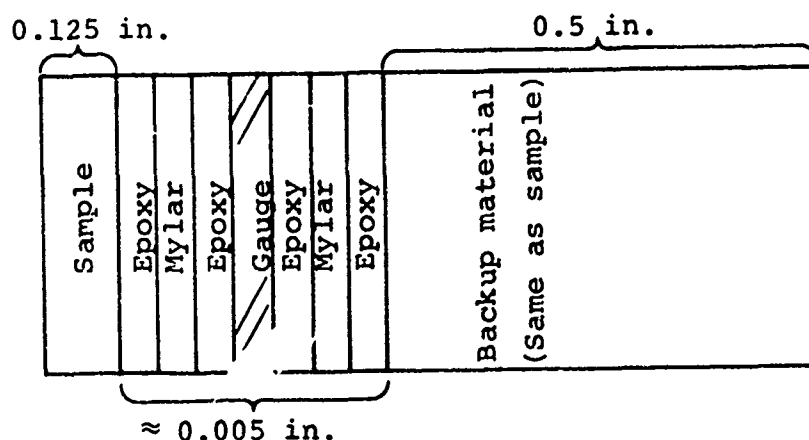
Figure 3 Manganin gauge geometry.

The gauge package was placed inside the bob of a ballistic pendulum in order to make simultaneous measurements of impulse and stress (see Appendix C). Five data points were taken at peak doses of approximately 2000 cal/gm. A typical gauge signal is shown in Figure 4. Qualitatively, the stress histories consisted of sharp, triangular spikes of approximately 200 to 300 nsec followed by a long, shallow tail which lasted for the entire gauge readtime (10 μsec).
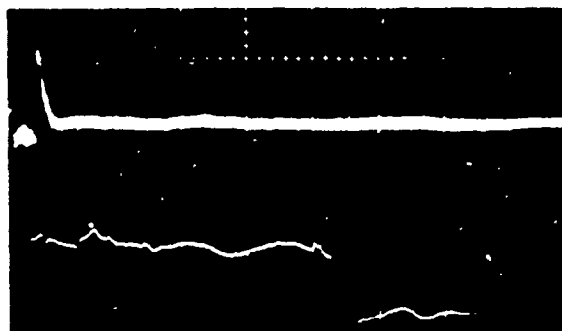
13
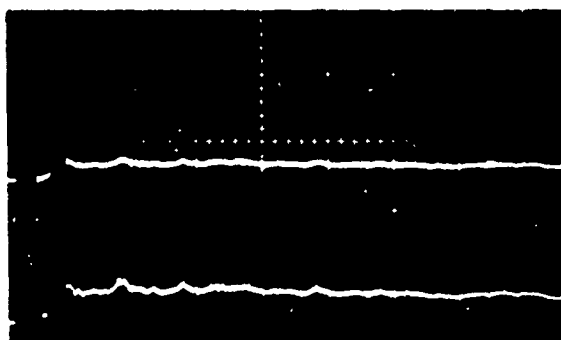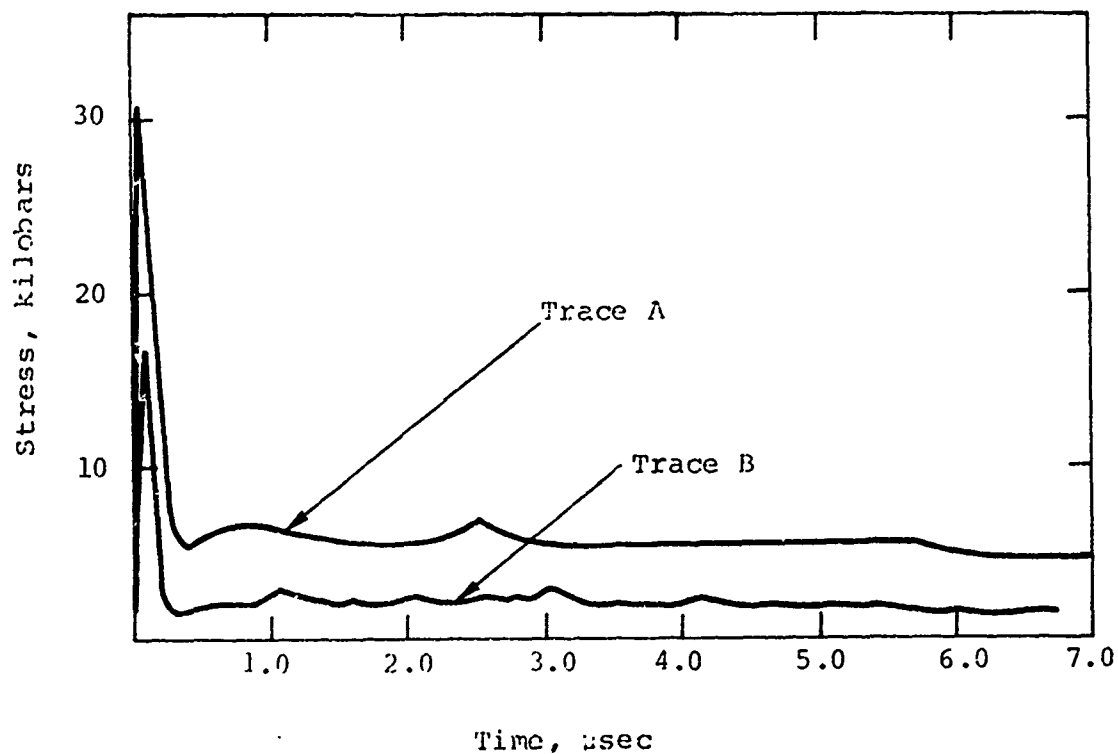
Figure 4   In-material stress histories recorded by manganin
gauges (aluminum data).

14

The millivolt level output signal of the manganin gauge required extensive shielding from the rf environment in the electron-beam drift chamber. This required a sample thickness of 0.125 inch. Since electron ranges for the irradiations performed in this program are typically 0.020 inch, the stress measurements were made well outside the deposition region and the stress pulse was attenuated.

Quantitative interpretation of manganin-gauge-measured stress histories were further complicated by a somewhat non-reproducible hysteresis (approximately 15 percent) and two-dimensional effects resulting in gauge stretching. Both flaws are in the direction of higher output from the gauge.

A comparison of measured impulse with the integral under the stress curve showed

$$\text{Measured impulse} < \int \sigma(t) \, dt.$$

The laser interferometer (see Appendix B) was used to measure rear-surface velocity histories. The rear-surface velocity histories were then converted to stress incident on the rear surface by using the Hugoniot of 6061 aluminum. The displacement mode, applicable for low-amplitude signals, was used on thick (0.5 inch) samples. The velocity mode, better suited for high amplitude pulses, was used with thin (0.32 inch) samples. In both cases, the laser beam was reflected from the polished rear surface of the samples. Before the signals from the rear surface were terminated by rear-surface spall (loss of reflecting surface), high-resolution stress histories of the thermomechanical spike were recorded with the velocity mode.

15

The laser interferometer data is shown in Figures 5 through 11.
The elastic precursor (at approximately 7 kbar) is clearly seen
in Figures 5 and 6. The long-duration, low-amplitude tails were
recorded on separate shots at the rear surface of thick samples.
The thick sample stress history in Figure 8 shows the arrival of
the thermomechanical spikes after reflection from the front
surface. The thick sample stress histories are undoubtedly no
longer one-dimensional even though their included areas (impulse)
are conserved in the two-dimensional distortion. Figure 11 shows
a composite of the thermomechanical (thin sample) stress to-
gether with the long-duration (thick sample) stress. This
composite has qualitative similarity with stress histories
obtained from manganin gauge measurements, but exhibits signifi-
cantly higher resolution.

In summary, manganin gauges have been used to measure
sample in-material stress over 10 µsec duration while simul-
taneously measuring impulse by positioning the gauge in a
pendulum bob. This stress measurement technique yielded only
qualitative information. Quantitative interpretation was
hindered by

1. Gauge hysteresis (non-reproducible)
2. Gauge stretching (two-dimensional effects)
3. Long risetime (equilibration in the gauge lamina)

The laser interferometer has proven to be a better tech-
nique for recording stress histories since it lacks the
objectionable features inherent in manganin gauge measurements.
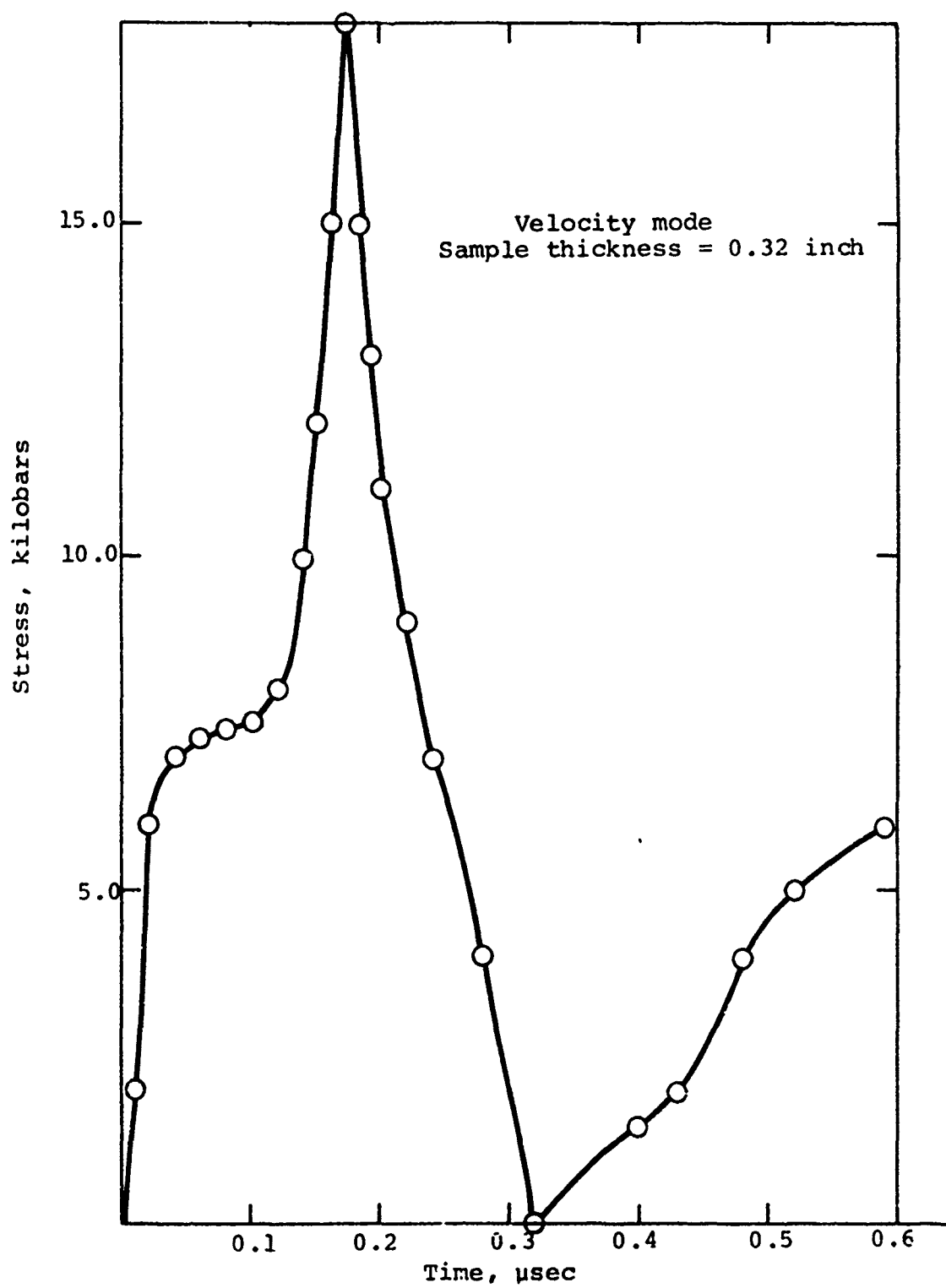
Figure 5   Stress history obtained with laser interferometer.

17

Figure 5 Stress history obtained with laser interferometer.

18
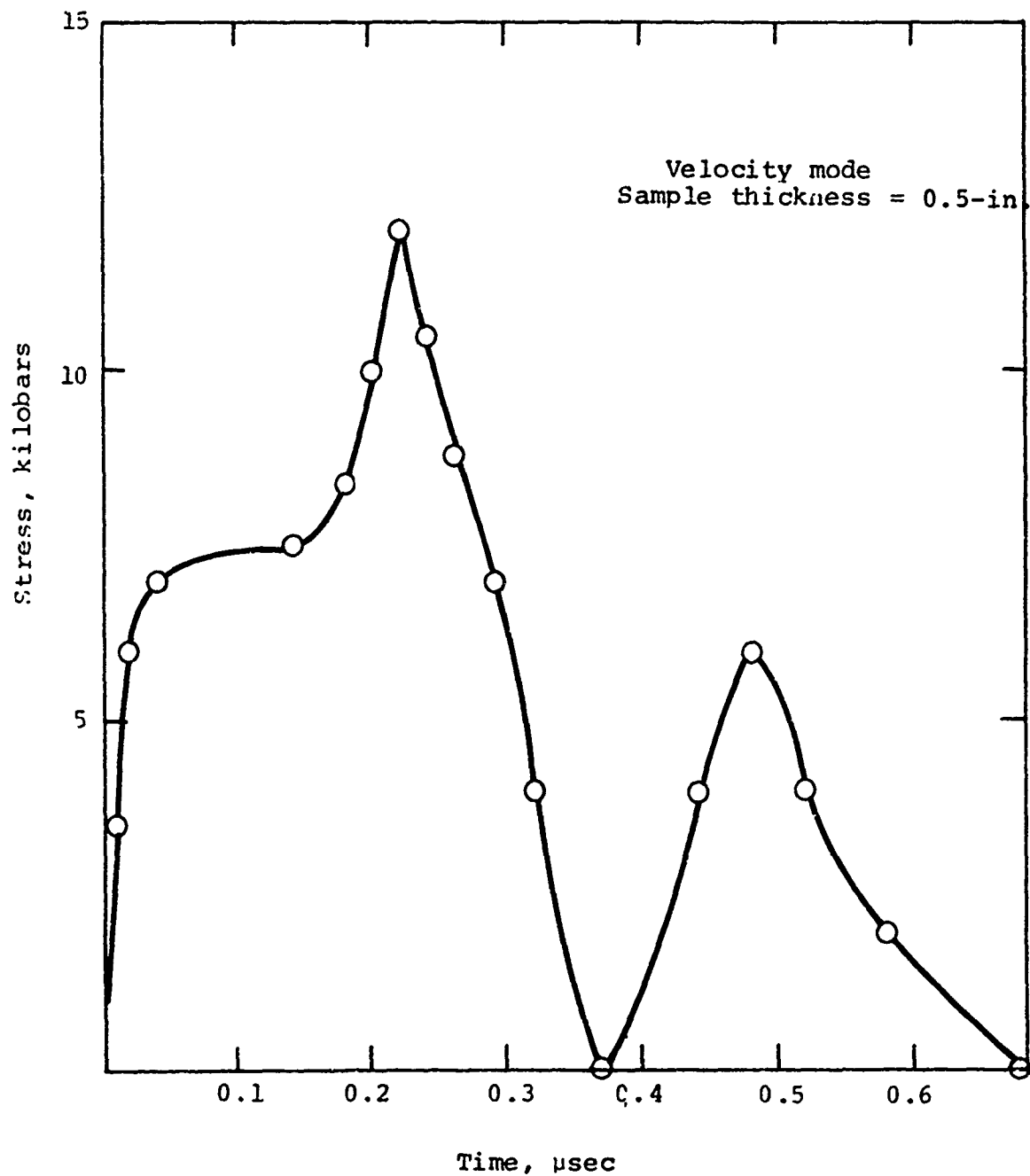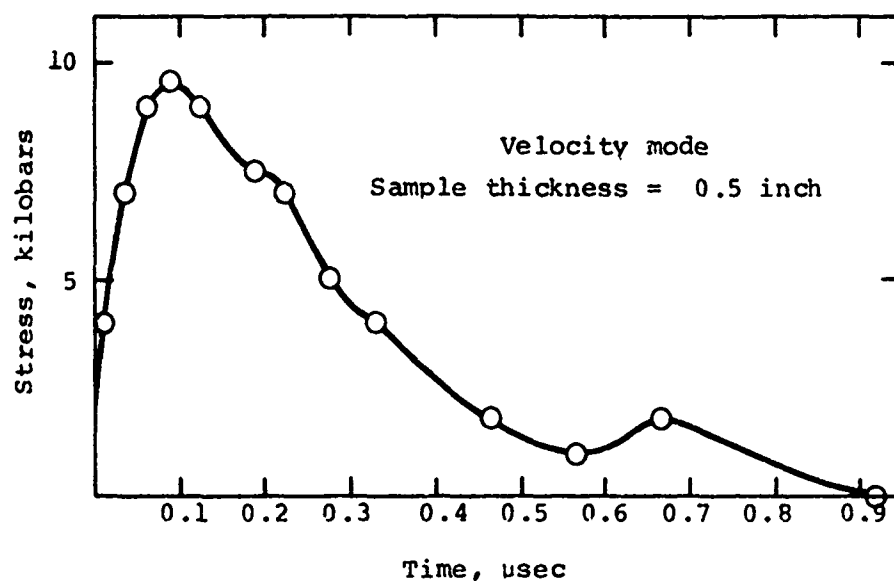
Figure 7   Stress history obtained with laser interferometer.
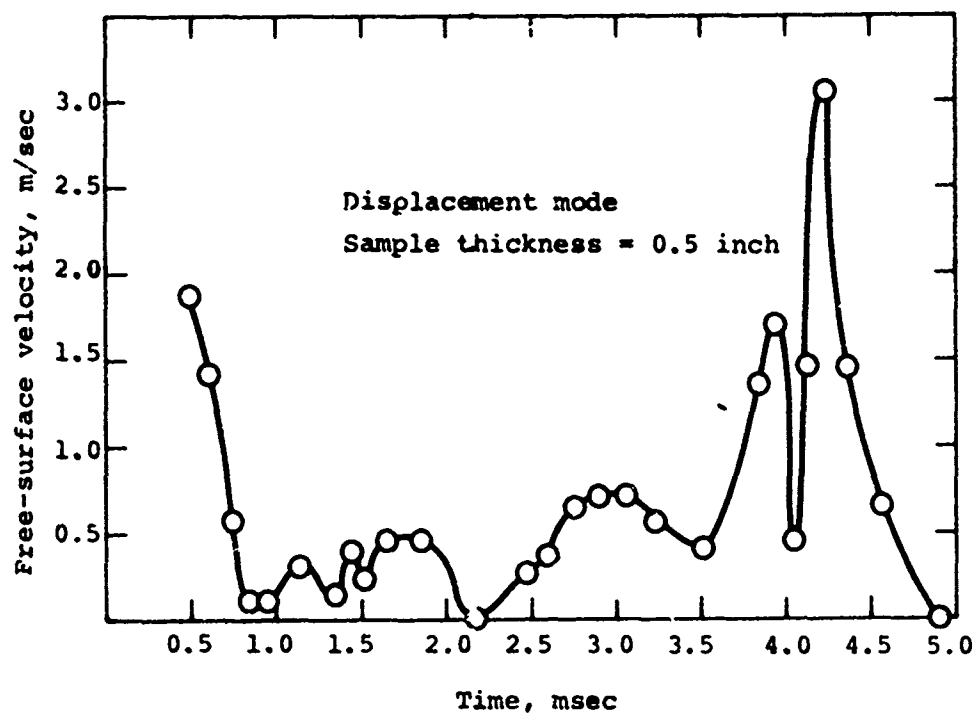
Figure 8   Stress history obtained with laser interferometer.

19
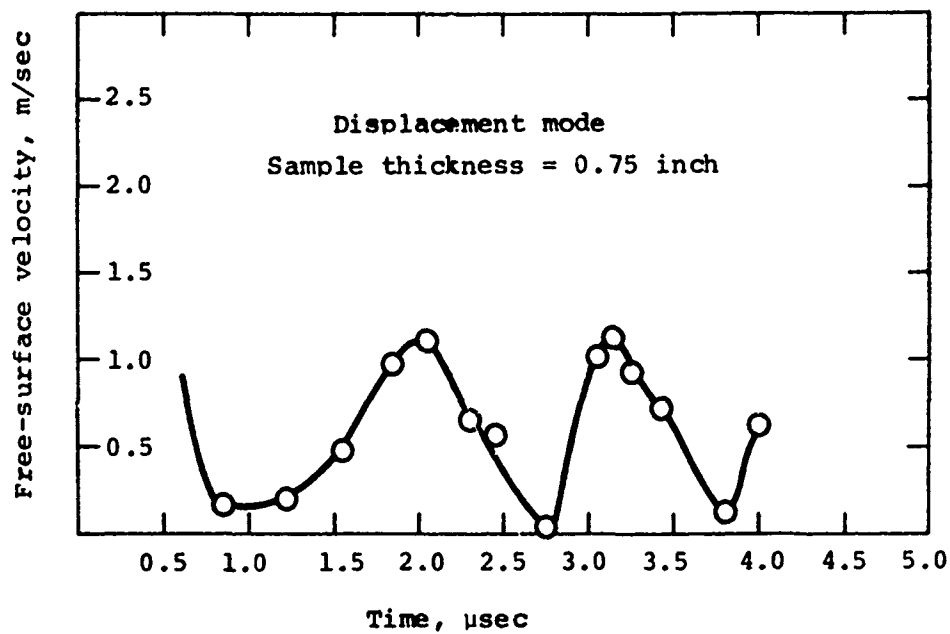
Figure 9   Stress history obtained with laser interferometer.
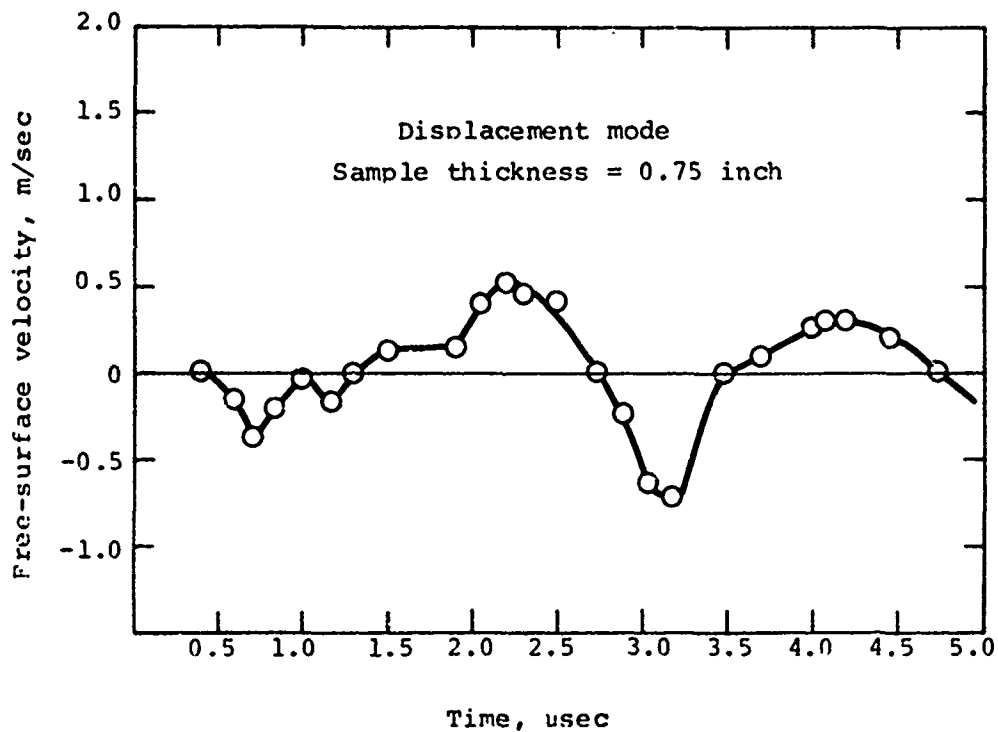
Figure 10   Stress history obtained with laser interferometer.

20

Mode		<E>	$\bar{\phi}$	Thickness
········	Velocity	(260)	(100)	0.5 in.
—·—·—	Displacement	(280)	(100)	0.75 in.
———	Displacement	(250)	(100)	0.5 in.
——————	Velocity	(370)	(100)	0.32 in.
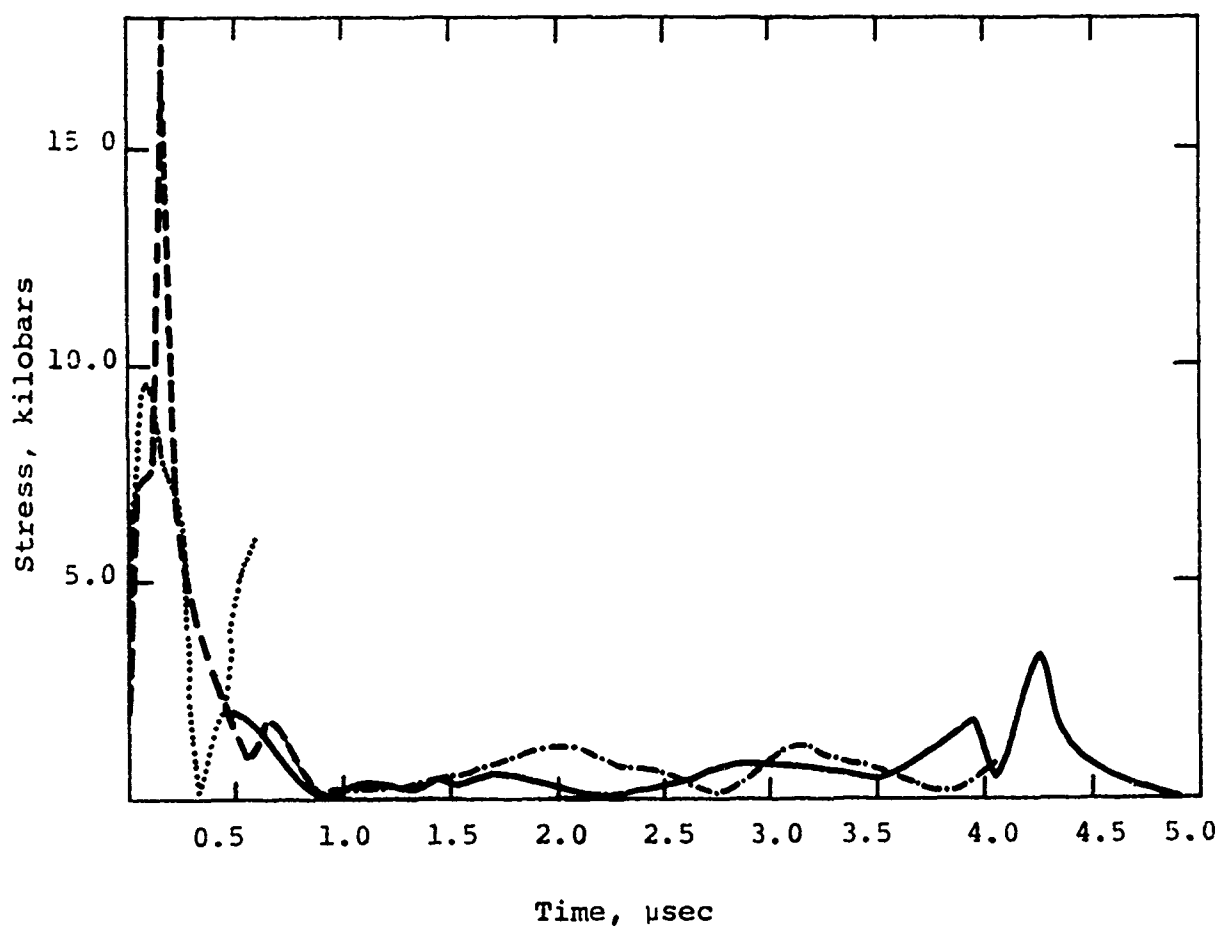
Figure 11   Laser interferometer data composite.

2.4 MASS REMOVAL DATA

The existing aluminum data point out a variety of crater appearances. A quick scan of the data indicates that craters vary in appearance with increasing fluence for a fixed mean electron energy. The observed variation is as follows:

1. Low fluence: craters are shallow with shiny, granular textured floor.

2. Medium fluence: craters are deeper with dull gray, smoother textured floor, occasionally dotted by a few small droplets.

3. High fluence: craters are obscured by some liquid "splash" (radially outward).

4. Highest fluence: craters are heavily obscured by "splash," but occasionally show deep crater floors with large droplets.

The four descriptions refer to irradiation at approximately 200 to 300 keV. High-fluence irradiations at about 600 keV result in deep, clean craters with shiny, granular textured floors. Descriptions 1, 3, and 4 are illustrated in Figure D-1.

In an effort to account for the diversity of crater appearances, the existing data which cover a wide fluence (and dose) range were analyzed according to crater appearance, depth of material removal, melt depth, electron range, and peak dose. This analysis revealed definite trends which led to a plausible explanation of crater appearances in terms of material removal mechanisms.

The above analysis required an additional category for the data. It became necessary to introduce groupings according to whether or not the propagated stress was allowed to reflect from the sample rear surface. Sample thicknesses varied over the data set from 0.08 to 0.50 inch and some of the thin samples had momentum traps attached to their rear surfaces. The category of samples with no reflected stress consisted of thin samples for which momentum traps "carried away" the propagated stress pulse.

Based on the criteria described above, all the data were sorted into two categories, each of which consisted of two subgroups according to whether or not rear surface stress reflection occurred. Category A labeled samples with clear craters--descriptions 1 and 2 above; category B consisted of samples whose craters were obscured by splash--descriptions 3 and 4 above.

Before discussing trends established by the data, it is helpful to consider some simple models of front surface mass removal--in particular, front surface spall in a semi-infinite, perfectly elastic slab of homogeneous metal. According to the derivations in Appendix D:

    1. The shortest distance from the front surface at which tension reaches its maximum value is exactly half of the electron range in the material.

    2. For finite spall strengths, spall will proceed in planes of equal thickness so that the maximum spall depth is less than or (at most) equal to half of the electron range.

Consequently, when the idealized solid is irradiated with an energy density below melt, the material removal depth due to front surface spall will be less than or equal to half the electron range, i.e.,

$$d_R \equiv \text{removal depth} \leqslant \text{half electron range} \equiv R/2$$

The exact material removal depth will depend, of course, on the fluence. The appearance of the crater will be typical of solid spall, clean and with a granular texture.

When the irradiation dose is increased above melt but below vaporization so that the solid is melted to exactly half-electron range, the same rule prevails. The exception comes in the form of thinner spall layers which allow the removal depth to approach half range more closely, i.e., $d_r \approx R/2$.

In this case, all the liquid will be removed to the melt depth. The crater should still look essentially clean but the floor should no longer resemble solid spall. Its appearance could be considerably smoother due to solidification of the remaining material at the incipient melt dose.

The intermediate case occurs when irradiation is such that the melt depth is less than half range. The liquid proceeds to spall to the melt depth. If the tension produced by reflection from the new free surface at the melt depth (see Appendix D) exceeds the solid spall strength, spall will continue into the solid material but will still not exceed half range, i.e., $d_R \leqslant R/2$. The crater will again be clean of any liquid splash and will have texture typical of solid spall.

24

The crater appearance and irradiation conditions discussed
analytically above match the data in Category A for the case of
no significant rear surface reflection of the propagated stress
(equivalent to a semi-infinite slab). Figure 12 shows a com-
parison of half range with measured removal depth for that
data. It is evident that, within experimental error,

$$\text{Removal depth} \leqslant \text{half range}$$

for all the data in this category. Figure 13 demonstrates that
for some of that data, melt depth, removal depth, and, hence,
half range were equal.

If the propagated stress is allowed to reflect in tension
from the rear (free) surface of a thin sample and if the tension
exceeds the spall strength of the material at that surface,
after rear-surface spall and propagation back to the front
surface, additional mass will be removed. The effect of such
(secondary) spall will be to increase mass loss and removal
depth but will not significantly increase momentum imparted to
the sample. The particle velocities in the secondary spall, as
well as in the remaining sample, will be in the same direction
and the effect of secondary spall will be to separate the two
masses, "trapping" lower particle velocities in the spall.

Data in Category B, because of its very nature, did not
lend itself to accurate measurements of removal depths. Liquid
splashes of various extent obscured the crater. Furthermore,
peak doses for much of the data in this category exceeded
incipient vaporization energy and the partially vaporized
material can no longer be considered to be linearly elastic. It

25
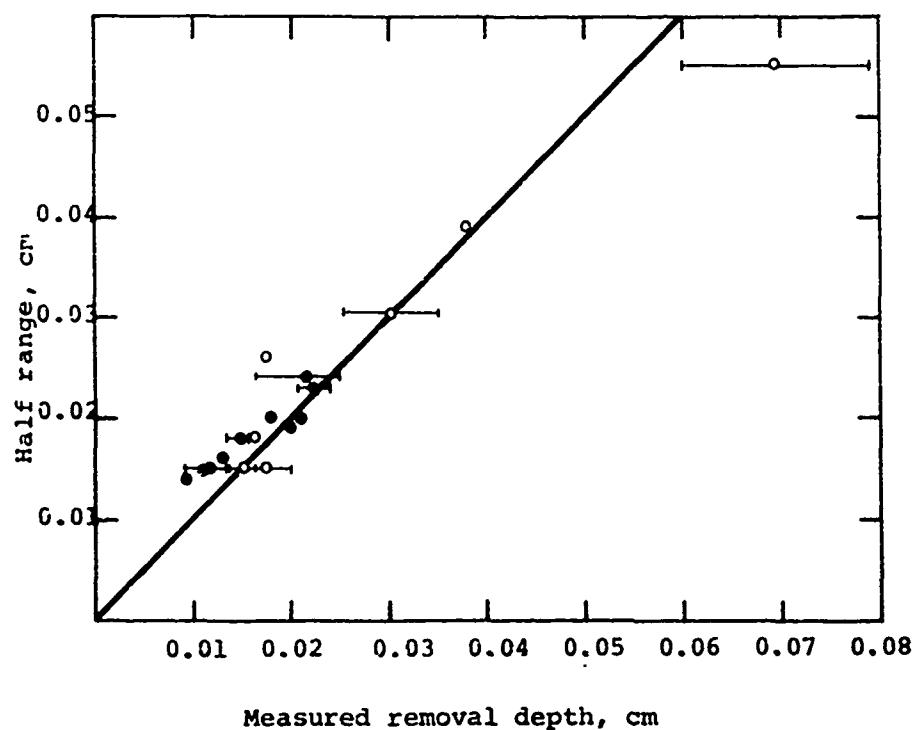
Figure 12 Half-range versus measured removal depth.
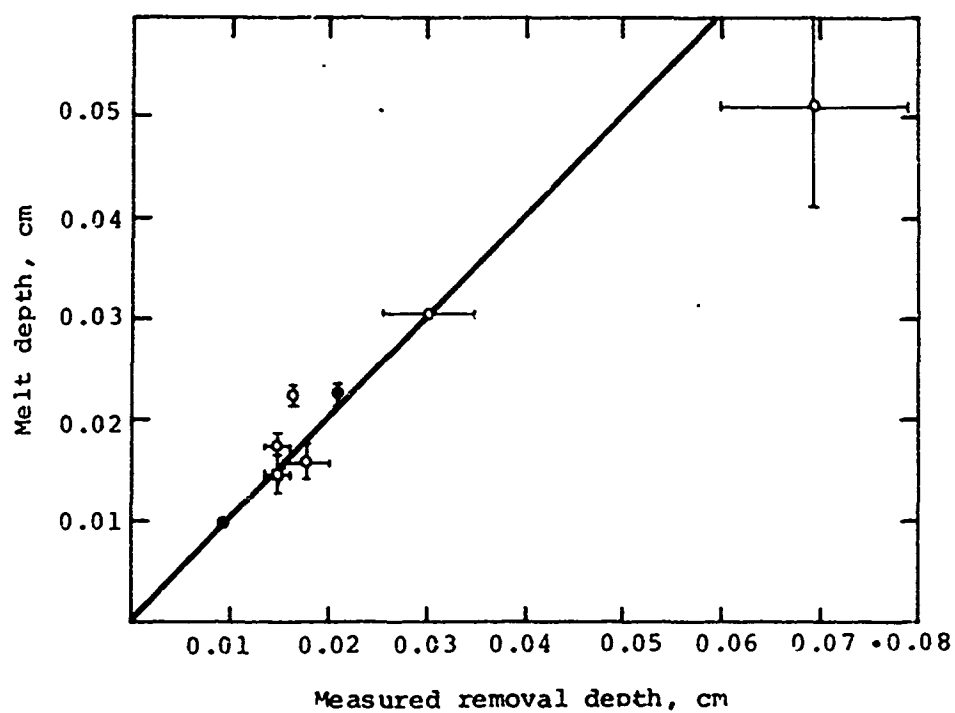
Figure 13 Melt-depth versus measured removal depth.

26

can be reasoned that the pressure resulting in vapor at the front surface can overcome the tension buildup in the remaining material, in which case the simple model used above no longer applies. However, that model can still be of use in understanding how splash occurs for irradiation below incipient vaporization doses.

If, for example, the melt depth exceeds half range, front-surface spall will remove liquid down to half range leaving a liquid layer behind. If secondary spall is excluded, that liquid layer will stay on. Two-dimensional radial relief can result in radial components of tension resulting in the migration of the remaining liquid layer away from the center of the crater. If solidification of the liquid occurs during this process, the "splash" appearance observed experimentally might result.

If secondary spall is allowed to occur while the liquid layer has begun localized solidification, the final appearance of the crater may show resolidified liquid instead of the radial splash. This condition will be accompanied by removal depths far in excess of half-range. Examples of this crater description are found among the data.

As described in the analysis section of this report, the experimental laser interferometer data and the predictions of the advanced multi-phase equation-of-state models both suggest that not all the impulse was delivered promptly ($\sim$ 100 nsec) for the high fluence and highest fluence experiments. This has been attributed to the recompression of the liquid layer by the overlying vapor and vapor-liquid layers after the initial drop to

27

zero pressure in the liquid layer. This may also account for
the final appearance of the craters which exhibit the "splash"
characteristics at the higher fluence levels.

In summary, the observed variety of crater appearance is
consistent with the front-surface spall mechanism, the solid-
to-liquid phase transitions, and the predictions of the advanced
equation-of-state models. Data which lend themselves to
quantitative analysis confirm this. When significant vapor
generation occurs at the front surface the pressure due to vapor
would tend to suppress front-surface spall of the liquid. If
radial relief or the recompression of the melted liquid layer
takes place, the final crater appearance will exhibit the
"splash" characteristic commonly observed at higher doses.

2.5 SUMMARY OF EXPERIMENTAL PROCEDURES AND RESULTS

Intense relativistic electron beams were used to achieve
rapid, in-depth heating in aluminum samples. Impulse and stress
data were collected over a peak dose range of 300 to 3800 cal/gm.

Simultaneous impulse and in-material stress measurements
were obtained using manganin piezoresistive transducers in con-
junction with a ballistic pendulum. Preliminary stress data
were obtained using a laser interferometer in the rear-surface
velocity and displacement modes. The laser technique demon-
strated high signal resolution.

28

Mass removal mechanisms have been examined and compared with crater depths and appearances. Quantitative agreement was found in the low-to-medium dose range (below vaporization energy). Qualitative interpretation of crater appearances was given for the effects observed in the higher dose range (above vaporization energy).

SECTION 3

ANALYSIS OF MIXED-PHASE IMPULSE GENERATION

3.1 INTRODUCTION

The previous sections have described the experimental
techniques and difficulties encountered in obtaining material
response data on aluminum in the mixed phase regime (liquid-
vapor). In the program that preceded this effort (Reference 2)
emphasis was placed on phenomena found in the melt-dominated
regime.

The objective of the analytical portion of this program
was to compare the experimental data with predictions using
existing multi-phase equations of state. The investigation
was to determine the importance of phase changes and the input
parameters of the models on various material response character-
istics, such as stress generated and impulse imparted to the
sample. The analytical work was also to determine whether a
complex mixed-phase equation-of-state model was needed to
predict the observed material response or whether a simpler
but more physical model, such as suggested in Reference 2,
would do equally well over a specified range.

One of the main results of the preceding investigation
(Reference 2) on melt-dominated impulse was that both the
experimental impulse and stress histories were predicted by a
simplified model which only considered the solid and liquid

phases. A simplified formula, given in Equation 1 was found
to predict the impulse for a number of metals in the melt-
dominated regime. This simplified expression was found to be
valid for energy densities well above incipient vaporization at
atmospheric pressure. A theoretical upper limit was established;
however, an experimental upper limit on the maximum energy
densities for which the simplified expression was valid was not
established. This program attempts to establish this upper limit
on energy densities for which the simplified linear fluid model
is applicable.

The experimental portion of this program has obtained peak
doses up to approximately 3800 cal/gm which is well above the
energy density (3350 cal/gm) required to fully vaporize aluminum
at atmospheric pressure. Because of the high peak dose obtained
experimentally in this program, it was deemed advisable to
compare the data with the predictions of the latest multi-phase
equation-of-state models.

This section contains a brief description of the two multi-
phase equation-of-state models, the PHILCO-FORD and GRAY
equation-of-state models. The experimental results are compared
with the predictions of the following equation-of-state models
in Section 5:

        a. PUFF

        b. LINEAR FLUID

        c. GRAY

        d. PHILCO-FORD

3.2 PHILCO-FORD EOS

The PHILCO-FORD (P-F) equation-of-state model (Reference 5) was developed by the Aeronutronic Division of Philco-Ford Corporation for the DNA-sponsored PREDIX program. This model was developed for materials, such as metals, which melt rather than sublime and whose vapor is composed of atomic species. The model includes provisions for treating the liquid-solid and liquid-vapor mixed-phase regions as well as the single-phase solid, liquid, and vapor regions.

What follows is a brief description of how the P-F equation-of-state model treats each phase region and constructs the various phase transition lines.

3.2.1 <u>Vapor-Phase</u>. In the vapor phase a generalization of the van der Waals equation is used. The formalism that is followed was first given by Hirschfelder, et al., (References 6 through 8) for describing the vapor phase of the noble gases. The expression used is given by

$$(P + A(T)/V^2 + A'(T)/V^3)(V - B+B'/V) = RT \qquad (2)$$

where $\bar{A}$ and $\bar{B}$ in van der Waals equation are now

$$\bar{A} = A(T) + A'(T)/V \qquad (3a)$$

$$\bar{B} = B - B'/V \qquad (3b)$$

with B and B' being constants.

33

The expression is then non-dimensionalized by introduction of the reduced variables, $p = P/P_c$, $v = V/V_c$, and $t = T/T_c$, where the subscript c refers to values of the thermodynamic variables at the critical point. With the introduction of the critical compressibility ratio, $Z_c = P_c V_c/R\, T_c$, (Equation 2) reduces to

$$p = \rho t/Z_c \left(1 - b\rho + b'\rho^2\right) - a(t)\rho^2 - a'(t)\rho^3 \qquad (4)$$

where $a(t) = A(T)/P_c V_c^2$, $a'(t) = A'(T)/P_c V_c$, $b = B/V_c$, $b' = B'/V_c^2$, and $\rho = 1/v$. The relationships between the various parameters are obtained by the requirement that the critical isotherm has a point of inflection at the critical point. In terms of Equation 4 this means that $(\partial p/\partial \rho)_t$ and $\partial^2 p/\partial \rho^2$ are zero at the critical point, $p = \rho = t = 1$. Applying this with the assumption that $a'(1) = 0$ gives

$$a(1) = \beta \qquad (5a)$$

$$b = \left(3\beta^2 - 6\beta - 1\right)/\beta(3\beta - 1) \qquad (5b)$$

$$b' = (\beta - 3)/(3\beta - 1) \qquad (5c)$$

where β is related to the critical compressibility ratio by

$$Z_c = \beta(3\beta - 1)/(\beta + 1)^3 \qquad (5d)$$

Thus b and b' are known once β is determined. The determination of β is described in the section that discusses the vapor-liquid mixed-phase region.

The following temperature-dependent forms for a(t) and a'(t) are suggested.

34

$$a(t) = k_o + \left(\beta - k_o\right)/t = k_o + k_1 t \qquad (6a)$$

$$a'(t) = \frac{1}{2}\left(1 - k_o + 2\beta - \alpha\right)(t-1/t) = k_2(t-1/t) \qquad (6b)$$

The parameter k_o is an input parameter and α is determined from considerations of the vapor-liquid mixed phase region by noting that $\alpha = (\partial p/\partial t)_\rho$, evaluated at the critical point.

The internal energy of the vapor phase is obtained by using the thermodynamic relationship:

$$\left(\frac{\partial E}{\partial V}\right)_T = T\left(\frac{\partial P}{\partial T}\right)_V - P \qquad (7)$$

and integrating the equation from zero density along an isotherm

$$E(v,t) - E_o(T) = -Z_c RT_c \int_0^\rho \frac{1}{\rho^2} \left| t\left(\frac{\partial p}{\partial t}\right)_\rho - p \right| d\rho$$

$$= Z_c RT_c \left| -\left(k_o + 2k_1/t\right)\rho + k_2\rho^2/t \right| \qquad (8)$$

where $E_o(T)$ is the internal energy at the temperature T and zero density. The form for $E(T)$ that is chosen is that of an ideal monatomic gas with the contribution to the internal energy from electronic excitations assumed to be zero. With these assumptions $E_o(T)$ becomes

$$E_o(T) = E_o + C_v T \qquad (9)$$

where E_o is the reference energy at 0°K.

35

The equation-of-state for the vapor phase is then given by Equations 4, 8, and 9. Given the input variables V and E, the system of equations is solved in order to obtain the pressure. The vapor portion of the P-F equation-of-state is used for densities less than the critical density when the point lies outside the liquid-vapor mixed-phase region.
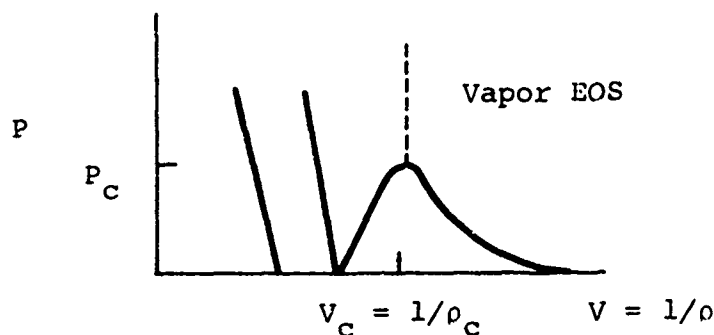
3.2.2 <u>Vapor-Liquid Mixed-Phase</u>. Pressure as a function of temperature in the mixed-phase region is obtained by using the Clapeyron-Clausius equation:

$$\frac{dP}{dT} = \frac{\Delta H}{T \left(V_v - V_\ell\right)} \qquad (10)$$

where ΔH is the heat of vaporization at temperature T. The subscripts v and ℓ refer to the vapor and liquid phases, respectively, at temperature T. The specific volume of the liquid phase is assumed to be negligible in comparison with that of the vapor phase

$$V_v \gg V_\ell \qquad V_v \approx \frac{RT}{P} \qquad (11)$$

and the heat of vaporization is approximated by

$$\Delta H \approx \Delta H_B + \Delta C \left(T - T_B \right) \tag{12}$$

where ΔC is the difference between the specific heats of the
liquid and vapor. The subscript B refers to conditions at the
normal boiling point. With these assumptions the Clapeyron-
Clausius equation is intergrated to give pressure as a function
of temperature in the liquid-vapor phase region.

$$\ell n \frac{P}{P_B} = \frac{\Delta H_B - \Delta C \ T_B}{R} \left[\frac{1}{T_B} - \frac{1}{T} \right] + \frac{\Delta C}{R} \ell n \frac{T}{T_B} \tag{13}$$

This expression is used in the liquid-vapor region for tempera-
tures less than the critical temperature.

The critical pressure is not determined from Equation 13 by
setting $T = T_c$, but is obtained by an alternate approach which
first determines the critical compressibility ratio. The critical
compressibility ratio is determined by using the form of the
reduced vapor pressure suggested by Riedel and used by Hirschfelder,
et al.

$$\ell n \ p = \alpha_R \ \ell n \ t - 0.0838 \left(\alpha_R - 3.75 \right) \left(\frac{36}{t} - 35 - t^6 + 42 \ \ell n \ t \right) \tag{14}$$

where all thermodynamic quantities are reduced variables. The
parameter α_R is specified by requiring that Equation 13 satisfy
the Clapeyron-Clausius equation at the normal boiling point

$$\frac{1}{p} \frac{dp}{dt} \bigg|_{t \ = \ t_B} = \frac{\Delta H_B}{RT_c} \frac{1}{t_B^2} \tag{15}$$

37

The critical compressibility ratio is then obtained from the relationship suggested by Riedel.

$$Z_c = \left[3.72 + 0.26 \left(\alpha_R - 7 \right) \right]^{-1} \tag{16}$$

Both Equation 14 and Equation 16 which are used to define the critical compressibility ratio are based on relationships which were based on hydrocarbon data. Their extension to metals does seem questionable; however, the results of using Equation 16 give reasonable agreement with the results of more rigorous calculational procedures.

The line that separates the mixed-phase vapor-liquid region from the vapor region is constructed by setting Equations 4 and 14 equal and solving for the reduced vapor density, ρ_v, as a function of the reduced temperature, t, for $t < 1$,

$$\rho_v t / Z_c \left(1 - b \rho_v + b' \rho_v^2 \right) - a'(t) \rho_v^2 - a(t) \rho_v^3$$

$$= \exp \left[(\alpha - \alpha_1)(1 - 1/t) + \alpha_1 \ln t \right] \tag{17}$$

where $\alpha_1 = \Delta c / R$. Since ρ_v is known as a function of t along this line and P is given by Equation 13, the line that separates the mixed-phase vapor-liquid region from the vapor region is known. The internal energy along this line is found from Equation 8.

For the line that separates the liquid from the liquid-vapor region, an expression proposed by Hirschfelder is used. The reduced liquid density is

$$\rho_\ell(t) = 1 + c(1 - t)^{1/3} + d(1 - t) \tag{18}$$

38

where c and d are constants that depend on the material. The value for the constants c and d, which are suggested in Reference 5, are c = 1.8 and d = 1.75. These values are appropriate for the alkali metals and have been extended to other metals. The internal energy on the liquid side of the vapor-lined region is determined from the value of the internal energy on the vapor side (Equation 8) and the Clapeyron-Clausius equation (Equation 10). Thus, the reduced thermodynamic quantities p, t, ρ and E, are known along the boundary of the liquid-vapor region.

The critical density, ρ_c, is determined by requiring that the vapor-liquid region join the solid mixed-phase region at zero pressure,

$$\rho_c = \frac{\rho_\ell (T_m)}{\left[1 + c \left(1 - t_m\right)^{1/3} + d \left(1 - t_m\right)\right]} \tag{19}$$

The critical pressure is then

$$P_c = Z_c \, RT_c / V_c \tag{20}$$

The critical temperature is an input parameter of the model. The vapor fraction F is introduced and the equations are solved iteratively.

3.2.3 **Solid Phase.** The equation-of-state for the solid phase in the model is the standard PUFF solid equation-of-state:

$$P(\rho, E) = C\mu + D\mu^2 + S\mu^3 + (\mu + 1)\, \Gamma E \qquad \mu = \frac{\rho}{\rho_o} - 1 \tag{21}$$

The model does, however, require that $(\partial P / \partial \rho)_E$ remain greater than zero for problem free application. This precludes using values of S which are negative. There is also a consistency condition which must be satisfied; it requires that the pressure at the normal

39

boiling point be zero. The code handles this internally by the following logic:

a. If the density at the normal melting point, ρ_{so}, is specified, the code sets the internal energy at the normal boiling point (E_{so}, so that $P(\rho_{so}, E_{so}) = 0$.

b. If E_{so} is specified, then ρ_{so} is determined such that $P(\rho_{so}, E_{so}) = 0$.

3.2.4 Solid-Liquid Mixed-Phase. For the solid-liquid mixed-phase region the Clapeyron-Clausius equation is used once again:

$$\frac{dP}{dT} = \frac{\Delta H}{T\left(V_\ell - V_s\right)} \tag{22}$$

where ΔH is the heat of fusion. The subscripts ℓ and s refer to the liquid and solid phase, respectively. The slope dP/dT along the melting line is assumed constant giving the pressure as a function of temperature:

$$P = \frac{\Delta H_m}{V_{\ell o} - V_{so}}\left[\frac{T}{T_m} - 1\right] \equiv \frac{\Delta E_o}{\Delta V_o}\left[\frac{T}{T_m} - 1\right] \tag{23}$$

where the subscript m refers to conditions at the normal melting point. The quantities $V_{\ell o}$ and V_{so} are the liquid and solid density at the zero-pressure melting temperature. As a consequence of assuming that dP/dT is a constant along the melting line, the ratio of the energy difference to the volume change between the solid and liquid is constant,

$$\frac{\Delta E}{\Delta V} \equiv \frac{E_\ell(T) - E_s(T)}{V_\ell(T) - V_s(T)} = \frac{\Delta E_o}{\Delta V_o} \tag{24}$$

40

The initial slope of the internal energy as a function of temperature is known for both the liquid and vapor phases since the respective specific heats are known. The average internal energy of the liquid and solid is assumed linear with temperature with the proportionality constant being the average specific heat of liquid and solid at normal pressure conditions. This relation is given by

$$\bar{E}(t) \approx \frac{E_\ell(T) + E_s(T)}{2} = \frac{E_\ell(T_m) + E_s(T_m)}{2} + \bar{C}\left(T - T_m\right) \quad (25a)$$

where

$$\bar{C} = \frac{C_s(T_m) + C_\ell(T_m)}{2} \quad (25b)$$

The form of the expression for the internal energy of the liquid and solid phase is constructed so that $dE_\ell/dT = C_\ell$ and $dE_s/dT = C_s$ at temperatures close to T_m. At large temperatures $dE_\ell/dT \approx \bar{C}$ and $dE_s/dT \approx \bar{C}$. The suggested forms that satisfy these conditions are

$$E_\ell(T) = E_{\ell o} + \bar{C}\left(T - T_m\right) + \frac{\Delta C}{2} T_m \left[\frac{T_m}{T} - 1\right] \quad (26a)$$

$$E_s(T) = E_{so} + \bar{C}\left(T - T_m\right) - \frac{\Delta C}{2} T_m \left[\frac{T_m}{T} - 1\right] \quad (26b)$$

where

$$\Delta C = \frac{C_s - C_\ell}{2} \quad (26c)$$

41

The melting entropy is given by

$$\frac{\Delta H}{T} = \frac{E_{\ell}(T) - E_s(T) + P\left[V_{\ell}(T) - V_s(T)\right]}{T} \qquad (27)$$

Substituting Equation 24 into Equation 23 provides an expression for the melting entropy

$$\frac{\Delta H}{T} = \frac{E_{\ell} - E_s + \left(E_{\ell} - E_s\right)\left[\frac{T}{T_m} - 1\right]}{T} \qquad (28)$$

which reduces to

$$\frac{\Delta H}{T} = \frac{E_{\ell} - E_s}{T_m} \qquad (29)$$

Since ΔC is generally a small quantity, the difference in internal energy is nearly constant. Therefore, the melting entropy is also nearly constant and approximately equal to

$$\frac{\Delta H}{T} = \frac{E_{\ell} - E_s}{T_m} \approx \frac{E_{\ell o} - E_{so}}{T_m} \qquad (30)$$

The density on the solid melting curve is obtained by requiring that the pressure be continuous across the solid melting curve. This means that Equations 21, and 23 must be solved simultaneously. The density on the liquid melting curve may then be obtained by using the Claperyon-Clausius equation.

In the solid-liquid phase the volume V and internal energy E are related through the liquid fraction F:

$$V = F V_{\ell} + (1 - F) V_s \qquad (31a)$$

$$E = F E_{\ell} + (1 - F) E_s \qquad (31b)$$

42

The equations are solved iteratively to define $P(V,E)$ in the solid-liquid region.

3.2.5 **Liquid Phase.** The equation-of-state formalism up to this point has determined all the thermodynamic variables on the boundary of the liquid region. The equation of state in the liquid region is then developed by using empirical curves along which the internal energy is constant.

Two empirical expressions are suggested. The first assumes that the pressure is a linear function of density for a given energy

$$P_1(\rho, E) = \frac{P_{\ell m} - P_{\ell B}}{\rho_{\ell m} - \rho_{\ell B}} \rho - \frac{\rho_{\ell B} P_{\ell m} - \rho_{\ell m} P_{\ell B}}{\rho_{\ell m} - \rho_{\ell B}} \tag{32}$$

where the subscripts m and B refer to the melting and boiling sides of the liquid region. For $E > E_c$ the density $\rho_{\ell B}$ becomes ρ_c and $P_{\ell B}$ becomes $P_V(E, \rho_c)$ where the V refers to the vapor region. The second expression assumes that the logarithm of the pressure is a linear function of the logarithm of the density,

$$\ell n\, P_2(\rho, E) = \frac{\ell n\left(P_{\ell m}/P_{\ell B}\right)}{\ell n\left(\rho_{\ell m}/\rho_{\ell B}\right)} \ell n\, \rho \tag{33}$$

$$- \frac{\ell n\, \rho_{\ell B}\, \ell n\, P_{\ell m} - \ell n\, \rho_{\ell m}\, \ell n\, P_{\ell B}}{\ell n\left(\rho_{\ell m}/\rho_{\ell B}\right)}$$

The actual relation used for the equation of state in the liquid region is obtained by using a linear combination of the logarithms of the two pressures, P_1 and P_2,

43

$$\ln P (\rho, E) = F(E) \ln P_1 (\rho, E) + (1 - F(E)) \ln P_2 (\rho, E) \quad (34)$$

where $0 \leqslant F(E) \leqslant 1$ and is determined by the condition

$$\left. \frac{\partial P(\rho, E)}{\partial \rho} \right|_{\rho_{\ell m}} = \frac{P_{\ell m}(E)}{\rho_{\ell m}(E) - \rho_{\ell o}} \quad (35)$$

By choosing $F(E)$ in this manner P_1 is predominant at low energies, while P_2 is predominant at high energies.

3.2.6 <u>Discussion of the Model</u>. The PHILCO-FORD equation of state model was developed for materials, such as metals, which melt rather than sublime and whose vapor phase is composed of atomic species. Since the pressure of the triple point for metals is quite low, orders of magnitude below one atmosphere, the model has neglected the sublimation region of the phase diagram. The thermodynamic quantities which are measured at one atmosphere are assumed to occur at zero pressure.

The vapor equation-of-state is based on a modified van der Waals equation. This model in the vapor region should be adequate since both the experimental data and advanced theoretical calculations have demonstrated that it is applicable in this region. Electronic contributions to the specific heat have been neglected, but at the dose levels of interest for this report this contribution is negligible. Also, the formalism does exist for including these considerations within the model.

The envelope of the vapor-liquid region is determined by
using relations based on hydrocarbon data and an integration of
the Clapeyron-Clausius equation with assumptions which are not
justified over the total region of integration. Both of these
objections make the determination of the envelope questionable.
However, the results of the model give values for the critical
parameters, which are in reasonable agreement with values
determined from experiments and from advanced theoretical
considerations. This tends to support the validity of the
assumptions used to construct the envelope of the liquid-vapor
region and the equation-of-state model in the liquid-vapor region.

The equation-of-state in the solid region is equivalent
to the PUFF treatment for a solid, which has withstood the test
of time quite well.

In the mixed-phase liquid-solid region the melting entropy
is nearly constant. This assumption has been shown to be valid
for most metals both by experiment and theoretical considerations
(Reference 9). Unfortunately aluminum, the metal of interest
in this program, does not fall into this class of metals
(Reference 9). The specific heat of the liquid along the melt
line is assumed to be approximately a constant.

The liquid equation-of-state is the most questionable. The
relationships are entirely empirical and lack either experimental
or theoretical data for their justification. A much better
method of treating both the liquid phase and liquid-solid phase
would be to incorporate the liquid-metal equation-of-state based
on scaling proposed in Reference 9 and used by Royce in the GRAY
model, which is discussed later.

In summary, the PHILCO-FORD equation-of-state model has
provisions for treating the liquid-solid and liquid-vapor mixed-
phase regions as well as the standard solid, liquid, and vapor
phases. Its most questionable treatment is in the liquid-solid
and liquid regions. The framework does exist for modifying
these two regions with an updated treatment such as suggested
by Grover in Reference 9.

3.3 GRAY EOS

The GRAY equation-of-state model was developed at the
Lawrence Livermore Laboratory, Livermore, California by Royce,
Grover, Young, and Alder (References 10 through 12). The final
documentation is given in Reference 11.

In the solid, liquid-solid and liquid regimes the GRAY
equation-of-state model is based on the liquid-metal equation
of state developed by Grover (Reference 9). The vapor equation
of state has been obtained by analytically joining Grover's
model to the modified van der Waals equation-of-state developed
by Young and Alder (Reference 12). What follows is a brief
summary of the GRAY model.

3.3.1 <u>Solid, Solid-Liquid, and Liquid Region</u>. The funda-
mental assumptions used by Grover in obtaining the equation-of-
state in these regions are:

    a. The entropy of melting at constant pressure is a
constant independent temperature and pressure.

    b. The specific heat in the liquid has the functional
form $C_v = 3R - \alpha \, T/T_m$, $\alpha \simeq 0.15R$, $T > T_m$.

c. The melting temperature as a function of specific
volume can be obtained by integrating Lindemann's relation:

$$\frac{d \ln T_m}{d \ln v} = 2 \, \Gamma_s(v) - \frac{2}{3}$$

were $\Gamma_s(v)$ is the volume-dependent Gruneisen coefficient
for the solid phase.

In Reference 9 Grover carefully considers each assumption and
justifies each on the basis of experimental data, theoretical
considerations, and the results of numerical statistical
mechanics calculations.

The equation of state is constructed by using assumptions
(a) and (b) to obtain the Helmholz free energy A. The pressure
and energy relations then follow from the relations $P \equiv -(\partial A/\partial V)_T$
and $E = A + TS$. The equation-of-state is

$$A(T, V) = A_s(T, V) - v^2 \frac{\Delta T}{2} (\Delta S - \alpha) \left.\vphantom{\begin{array}{c}1\\1\\1\end{array}}\right\}$$

$$E(T, V) = E_s(T, V) + v \left(T - v \frac{\Delta T}{2} \right)(\Delta S - \alpha) \left.\vphantom{\begin{array}{c}1\\1\\1\end{array}}\right\} \quad T_m - \frac{\Delta T}{2} < T < T_m + \frac{\Delta T}{2}$$

$$V\,P(T, V) = V\,P_s(T, V) + \mu \, v \, T_m (\Delta S - \alpha)$$

$$A(T, V) = A_s(T, V) + T_m\left(\Delta S - \frac{\alpha}{2} \right) - T\Delta S + \frac{\alpha T^2}{2T_m} \left.\vphantom{\begin{array}{c}1\\1\\1\end{array}}\right\}$$

$$E(T, V) = E_s(T, V) + T_m\left(\Delta S - \frac{\alpha}{2} - \frac{\alpha T^2}{2T_m^2} \right) \left.\vphantom{\begin{array}{c}1\\1\\1\end{array}}\right\} \quad T > T_m + \frac{\Delta T}{2}$$

$$V\,P(T, V) = V P_s(T, V) + \mu T_m\left(\Delta S \cdot \frac{\alpha}{2} - \frac{\alpha T^2}{2T_m^2} \right)$$

where ΔT is the temperature difference between the solidus temperature $T_s(V)$ and liquidus temperature $T_\ell(T)$, $T_m = (T_s + T_\ell)/2$, $\nu = (T - T_s(V))/\Delta T(V)$, $\Delta S =$ entropy of melting, $\mu = -\, d\,\ell n\, T_m/d\,\ell n\, V$, and $\alpha =$ temperature coefficient of specific heat. The Mie-Gruneisen EOS for the solid extrapolated to temperatures above melting gives A_s, E_s, and P_s. The expression for ΔT is obtained by using the Clapeyron-Clausius equation. The integration of Lindemann's relation gives T_m, the melt temperature.

The specific heat decreases with increasing temperature until it reaches the ideal gas value of $3R/2$ at a temperature of T_G where it remains constant for increasing temperature. For temperatures above T_G the EOS takes on the simplified form

$$
\left.
\begin{aligned}
E(T,\,V) &= E_G(V) + \frac{3}{2}\,RT \\[2em]
V\,P(T,\,V) &= V\,P_G(V) + RT
\end{aligned}
\right\} \quad T > T_G(V) \equiv \frac{3R}{2\alpha}\,T_m(V)
$$

where

$$
E_G(V) = E_0(V) + T_m(V)\left[\Delta S + \frac{\alpha}{2}\left(\left(\frac{3R}{2\alpha}\right)^2 - 1\right)\right]
$$

$$
V\,P_G(V) = V\,P_0(V) + \mu(V)\,T_m(V)\left[\Delta S + \frac{\alpha}{2}\left(\left(\frac{3R}{2\alpha}\right)^2 - 1\right)\right]
$$

and $E_0(V)$ is the energy along the cold compression curve.

The GRAY equation of state has a volume- and energy-dependent Gruneisen coefficient $\gamma \equiv V(\partial P/\partial E)_V$. The solid-phase Gruneisen coefficient γ_S is a function of volume only. Upon melting γ exceeds γ_S; then, as the temperature is increased, γ slowly decreases until it reaches the ideal monatomic gas value of 2/3 at $T = T_G$ where T is approximately 10 T_m.

In summary, the GRAY equation-of-state model in the solid, liquid-solid, and solid region is based on Grover's liquid-metal EOS which is derived from scaling laws. The foundation of the model in these regions are the scaling laws (assumptions a through c) which are based on both experimental data and theoretical considerations.

3.3.2 Liquid-Vapor Region (Expanded Region). The liquid-vapor region uses a modified van der Waals equation-of-state developed by Young and Alder (Reference 12). The Helmholz free energy is expanded about the hard-sphere free energy as a perturbation series. The cohesive energy is approximated by the mean-field approximation used in the classical van der Waals model. What is obtained is a modified van der Waals model.

The model has been used to predict critical parameters of the metallic elements and compared with estimates from experimental data (Reference 12). The comparison with the experimental data is generally good in light of the errors which are present in the estimates from the experimental data.

3.3.3 The Complete EOS. The complete EOS is obtained by analytically joining the Grover scaling law model to the modified van der Waals model of Young and Alder at a specific volume of 1.3 to 1.5 times the normal volume. The joining is done in a thermodynamically consistent manner. The details and rationale for the joining are given in Reference 11.

3.3.4 <u>Discussion of the Model</u>. The GRAY EOS model treats the solid, liquid-solid, liquid, and vapor regions of the phase plane. The model is based on the results of two models which are formulated from theoretical considerations and which agree reasonably well with existing experimental data. The model does ignore the liquid-vapor region.

3.4 COMPARISON OF THE PHILCO-FORD AND GRAY EOS

Both the PHILCO-FORD and GRAY EOS models treat the solid, solid-liquid, liquid, and vapor phases. The P-F model also allows the existence of the liquid-vapor portion of the phase plane. This section describes some of the similarities and differences of the two models.

3.4.1 <u>Solid Region</u>. The models contain similar treatments of the solid phase. Both models follow closely the Mie-Gruneisen equation-of-state in the solid phase. The P-F model assumes that the Gruneisen coefficient γ is constant while the GRAY model has a linear dependence of γ on the specific volume.

3.4.2 <u>Liquid-Solid Region</u>. The models differ in the manner in which the melt line is established. The P-F model assumes that dP/dT along the melt line is constant and equal to the value obtained from the Clapeyron-Clausius equation evaluated at one atmosphere. The GRAY model first defines a parameter called the melting temperature

$$T_m(V) = \frac{T_s(V) + T_\ell(V)}{2}$$

where the subscripts s and ℓ refer to the solidus and liquidus respectively. The value of $T_m(V)$ is obtained by using Lindemann's law. An estimate of $\Delta T = T_\ell(V) - T_s(V)$ is obtained from the Clapeyron-Clausius equation.

50

The GRAY EOS assumes that the entropy change on melting is a constant. The entropy of melting in the P-F model is nearly constant because of the assumptions made in deriving the model in the melt region. Both models show an increase in the Gruneisen coefficient during melt for aluminum.

3.4.3 Liquid Region. The GRAY EOS is divided into two subregions. The first is referred to as the liquid region and it is for temperatures $T < T_G$ ($\sim 10\ T_m$). In this region the specific heat and Gruneisen coefficient are decreasing as the temperature increases. For temperatures above T_G the material is called a hot liquid with $C_v = 3R/2$ and $\gamma = 2/3$, the monatomic perfect gas value.

The P-F model uses empirical curves to span this region. These curves have no theoretical justification. The Gruneisen coefficient at normal value remains above two even for doses of as much as 20,000 cal/gm. The Gruneisen does, however, become smaller for an expanded volume.

3.4.4 Liquid-Vapor Region. The GRAY model does not consider the liquid-vapor region of the phase plane as a separate state. The GRAY model uses an EOS developed by Young and Alder which predicts values of the critical constants close to the experimentally observed values. This would seem to indicate that GRAY provides an adequate representation of the EOS in the critical region. However, the results of the comparison of GRAY, PUFF-V and P-F for aluminum described in the next section do not support this conclusion.

The construction of the envelope of the liquid-vapor region in the P-F model is not exact. However, the model predicts values of the critical constants which are close to the experimentally observed values. The model does provide reasonable definition of the liquid-vapor region.

3.4.5 Vapor Region. Both models use a modified van der Waal equation-of-state in the vapor region. The coefficient of attractive potential, a, in the van der Waal EOS, which was used in the numerical example for aluminum given in the next section, are comparable for each model.

$$a_{GRAY} = a_y = 0.06457 \quad \frac{mbar \ cm^6}{gm^2}$$

$$a_{P-F} = 0.07548 \quad \frac{mbar \ cm^6}{gm^2}$$

However, the pressure, sound speed, and Gruneisen parameters do not agree in the expanded region, Figures 21 through 23 .

3.4.6 High-Temperature Behavior. At high temperatures (on the order of 2 ev or above) the electronic contributions to the EOS become important. Neither the GRAY nor the P-F model takes into account the electronic contributions to the EOS. Thus application of both models to extremely high-temperature experimental data is questionable.

SECTION 4

COMPARISON OF THE GRAY, PHILCO-FORD, AND PUFF-V EQUATION-OF-STATE MODELS FOR ALUMINUM

4.1 INTRODUCTION

A comparison of the GRAY, PHILCO-FORD, and PUFF-V EOS models was carried out for aluminum. The input parameters used for each of the EOS models are given in Tables 2 through 4.

4.2 REFERENCE DENSITY

The pressure predicted by each EOS model as a function of internal energy density for aluminum at reference density is shown in Figure 14. The pressures predicted by the P-F model for aluminum at reference density are higher than those predicted by either the GRAY or PUFF-V EOS for internal energy densities above 400 cal/gm. For internal energy densities above 3500 cal/gm, the P-F pressures are at least a factor of two above those of GRAY. The PUFF-V and P-F models are in reasonable agreement for energy densities less than 3000 cal/gm.

In the PUFF-V EOS model, aluminum at reference density remains as solid as the internal energy density is increased. The pressure as predicted by PUFF-V is proportional to the internal energy density with the product of the Gruneisen coefficient times the density being the proportionality constant $(P = \rho \, \Gamma \, E)$.

TABLE 2

PHILCO-FORD EOS INPUT PARAMETERS FOR ALUMINUM

Description	Units	Value
Atomic weight	gm/mole	26.98
Normal density	gm/cm^3	2.71
Critical temperature	K^O	8000.00
c coefficient in liquid density equation	None	1.8
d coefficient in liquid density equation	None	1.75
k_o parameter in vapor EOS	None	0.0
Melting temperature T_M	K^O	932.00
Solid enthalpy at T_M	kcal/mole	4.291
Liquid enthalpy at T_M	kcal/mole	6.838
Vapor enthalpy at T_M	kcal/mole	81.177
Solid density at T_M	gm/cm^3	2.537
Liquid density at T_M	gm/cm^3	2.380
Boiling temperature T_B	K^O	2736.00
Liquid enthalpy at T_B	kcal/mole	19.466
Vapor enthalpy at T_B	kcal/mole	90.149
C coefficient in solid EOS	kbar	720.00
D coefficient in solid EOS	kbar	1313.00
S coefficient in solid EOS	kbar	2008.00
Gruneisen coefficient in solid EOS	None	2.18

TABLE 3

GRAY EOS INPUT PARAMETERS FOR ALUMINUM

Description	Units	Value
Normal volume of solid	cm^3/gm	1/2.71
Hugoniot parameter C	$cm/\mu sec$	0.524
Hugoniot parameter S	None	1.40
Lattice gamma parameter γ_o	None	2.18
Lattice gamma parameter a	None	1.70
Electronic energy coefficient	mbar $cm^3/mole$ deg^2	8.7×10^{-9}
Melting temperature parameter	deg.	1220
Atomic weight	gm/mole	26.98
Volume where equations of state are joined	cm^3/gm	0.4871
Excluded volume for vapor phase	cm^3/gm	0.1956
Coefficient of attractive potential for vapor a_y	$(cm^3/mole)^2$	47.

Note: For γ_{om}, a_m, γ_e, ΔS, E_{OH}, and θ, the normal relations were used.

55

TABLE 4

PUFF-V EOS INPUT PARAMETERS FOR ALUMINUM

Description	Units	Value
Density	gm/cm^3	2.71
C coefficient in solid EOS	mbar	0.720
D coefficient in solid EOS	mbar	1.313
S coefficient in solid EOS	mbar	2.008
Gruneisen coefficient	None	2.13
H parameter in vapor EOS	None	0.1
Sublimation energy	mbar	0.3232
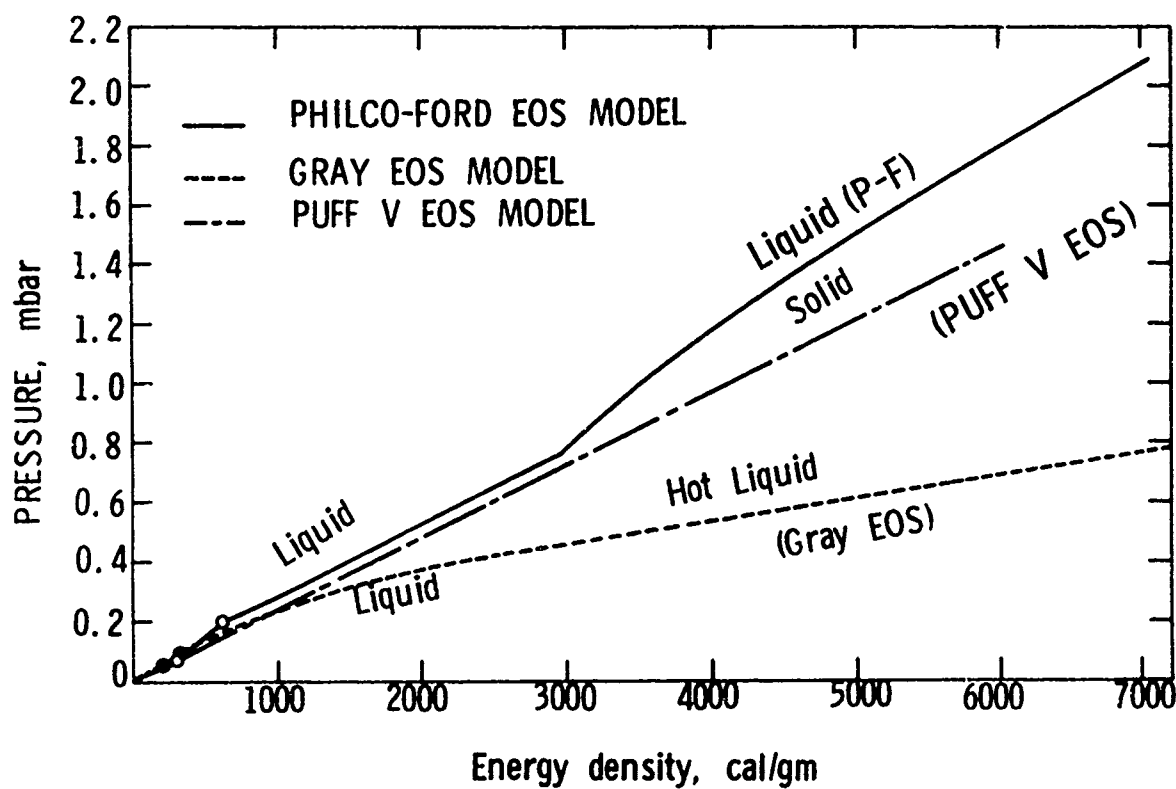
Figure 14 Comparison of predicted pressure as a function of
energy density for aluminum at reference density.

Both the GRAY and P-F EOS models allow aluminum to undergo
a melting phase transition at reference density for sufficiently
high internal energy densities. GRAY predicts the onset of
melting at 200 cal/gm with full melt occurring at approximately
300 cal/gm, while the corresponding values obtained from P-F are
300 cal/gm for start melt and 600 cal/gm for end melt.

The Gruneisen coefficient $\Gamma = V(\partial P/\partial E)_V$ as a function of
internal energy density for aluminum at reference density is
shown in Figure 15. As pointed out previously, the Gruneisen
coefficient in PUFF-V is independent of internal energy and
equal to a constant.

Both the P-F and GRAY EOS models show an increase in the
Gruneisen coefficient during the melting phase transformation
at constant volume. The Gruneisen coefficient during the melt
phase transformation at constant volume is larger than either the
solid or the liquid Gruneisen coefficient at energies adjacent
to the liquid-solid region.

For energies above 2500 cal/gm the Gruneisen coefficient in
the GRAY model is equal to the ideal monatomic gas value of 2/3.
The rationale for the decrease in Γ to this limiting value is
given in Reference 9.

The sharp increase in the P-F Gruneisen coefficient, which
occurs at 3000 cal/gm, is due to the manner in which the model
is constructed in the liquid phase region. For the liquid region
the pressure is determined by the thermodynamic conditions on
the boundaries of the liquid phase region (see Figure 16). For
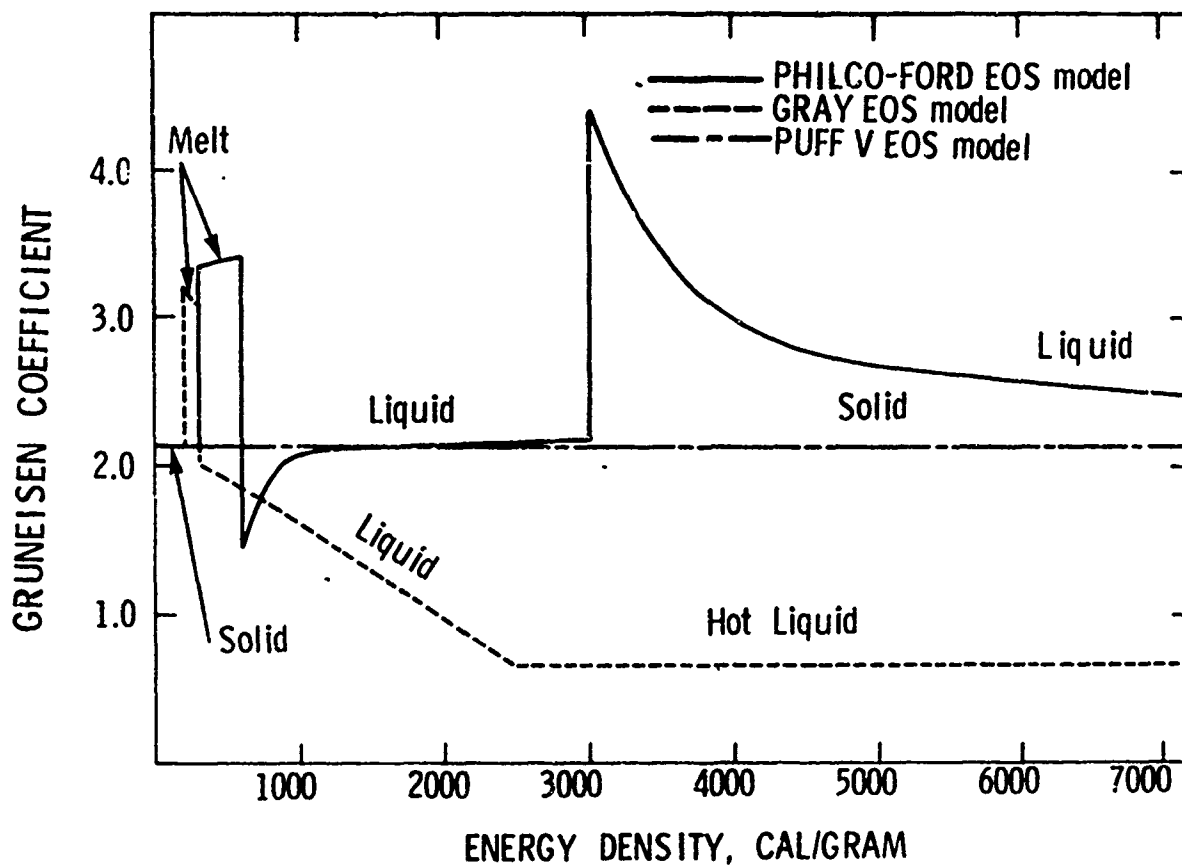
Figure 15   Comparison of the Gruneisen coefficient as a function of energy density for aluminum at reference density.
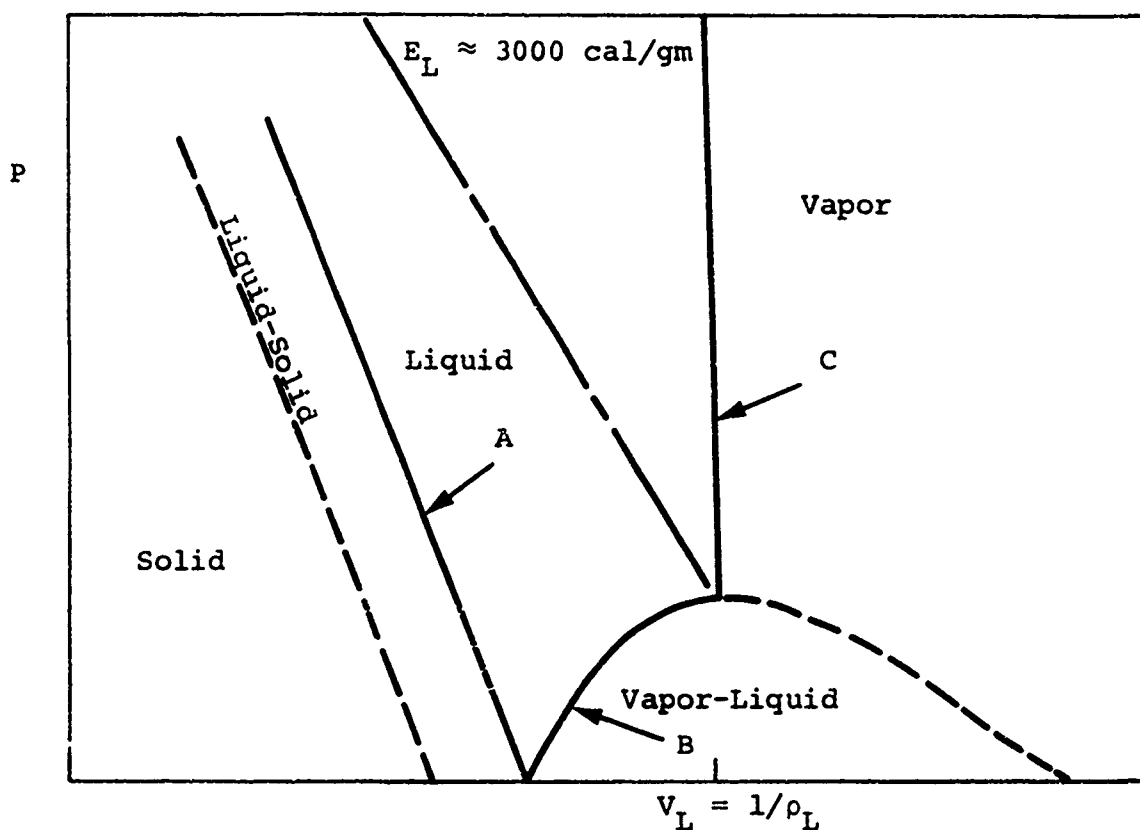
59

Figure 16   P-V phase diagram with liquid region boundaries
defined by a solid line.

internal energy densities below 3000 cal/gm, pressures in the
liquid phase region are determined from thermodynamic conditions
on the liquid side of the liquid-solid region (line A, Figure
16) and conditions on the envelope of the vapor-liquid region
(line B, Figure 16). When the internal energy densities are
above 3000 cal/gm, the liquid phase pressures are determined
from thermodynamic conditions in the vapor phase when $\rho = \rho_{critical}$

(line C, Figure 16) and conditions on the boundary of the liquid-solid region (line A, Figure 16). The construction of the EOS surface in the liquid region is one of the drawbacks of the P-F model. There is no sound physical reason to expect a discontinuous change in the pressure-energy coupling coefficient for reference density aluminum at an internal energy density of 3000 cal/gm.

Another thermodynamic quantity which influences the material response is the sound speed $\sqrt{(\partial P/\partial \rho)}_s$. The sound speed predicted by each model as a function of energy density for aluminum at reference density is shown in Figure 17. The comparison of sound speeds is similar to the Gruneisen coefficient comparison. For a given value of energy density the model that predicts the highest sound speed also predicts the highest Gruneisen co-efficient, while the model that predicts the lowest sound speed also predicts the lowest coefficient.

The P-F model predicts a decrease in sound speed as aluminum melts at reference density. The sound speed then increases as aluminum is heated through the melt region. At the end of the melting phase transformation at reference density, the sound speed in the liquid phase is higher than in the melt phase. Physically this means that the slope of the release adiabat $\frac{\partial P}{\partial v}\Big|_{adiab.} = -(\rho c)^2$ is discontinuous at both the begin melt and end melt.

In the GRAY EOS model the sound speed is continuous across the melting phase transformation and thus the slope of the release adiabat $\frac{\partial P}{\partial v}\Big|_{adiab.} = -(\rho c)^2$ is continuous at both begin melt and end melt.
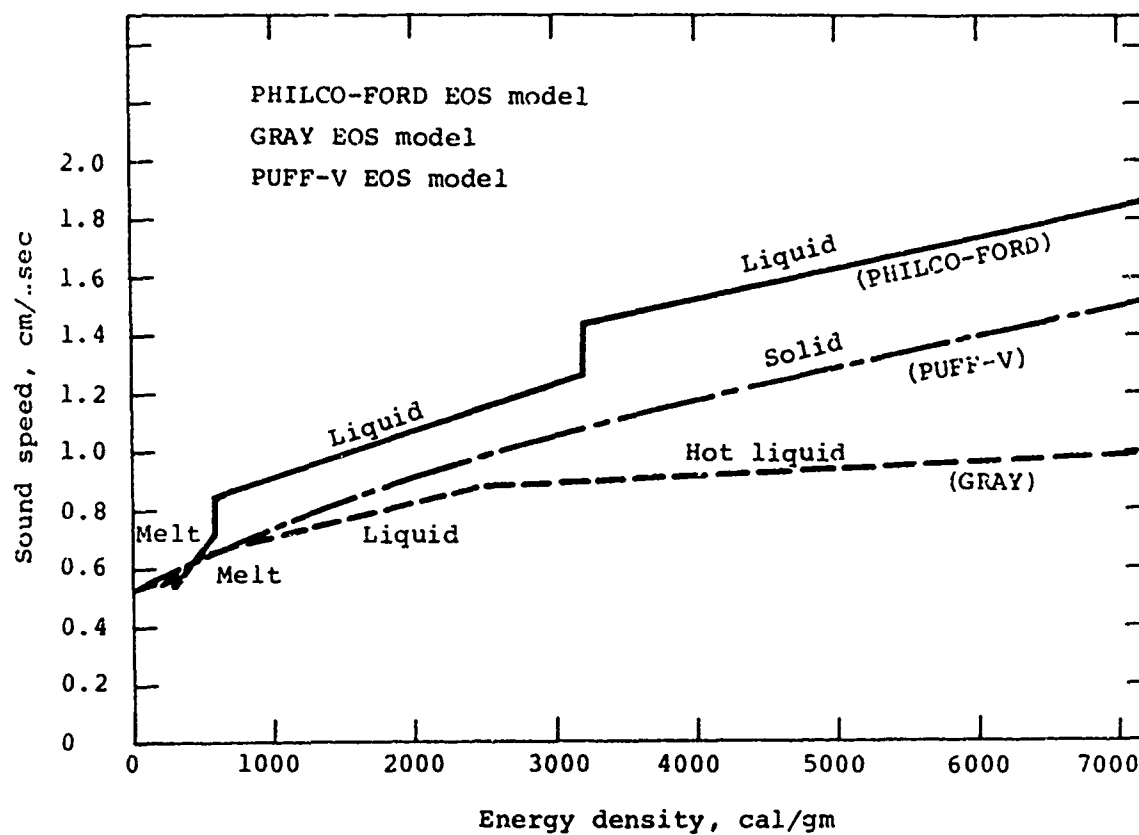
Figure 17 Comparison of predicted sound speed as a function of
energy-density for aluminum at reference density.

It is apparent from Figures 14 through 17 that the GRAY, PHILCO-FORD, and PUFF-V EOS models are in significant disagreement in the predicted values of pressure, Gruneisen coefficient, and sound speed as a function of energy density for reference density aluminum. The question which arises is the following: can the data (total impulse and propagated stress pulse measurements) be used to resolve the differences and choose which EOS model is more appropriate, or determine a new set of more appropriate input parameters?

In order to answer the above question, consider the case of melt-dominated material response. Assume an EOS of the form

$$P = f \left(\frac{\rho}{\rho_o} \right) + \rho \, \Gamma \, E$$

where P is the pressure, ρ is the density, ρ_o the reference density, Γ is the Gruneisen-energy coefficient, and E is the internal energy density. For the linearized problem

$$\rho = \rho_o \, (1 + \epsilon) \qquad \epsilon \ll 1$$

the peak propagating stress is given by Reference 13

$$\sigma_p = \frac{\rho_o \, \Gamma \, \phi}{2c \, \tau} \int_o^{c\tau} \widetilde{E}(s) \, ds \tag{35}$$

where ϕ is the fluence, τ the deposition time, c the sound speed, and $\widetilde{E}(s)$ is the normalized energy deposition profile. When Equation 35 is specialized to a linear deposition profile with range r

$$\tilde{E}(s) = \tilde{E}_O \left(1 - \frac{s}{r}\right), \quad r = \text{range}$$

the peak propagating stress is given by

$$\sigma_p = \frac{\rho_O \Gamma E_O}{2} \left[1 - \frac{c\tau}{2r}\right] \qquad c\tau \leqslant r \qquad (36a)$$

$$\sigma_p = \frac{\Gamma \phi}{2c\tau} \qquad\qquad c\tau \geqslant r \qquad (36b)$$

where $E_O = \phi \tilde{E}_O$ is the maximum deposited energy. If we make the additional assumption that the material is removed to half range, then the impulse has been shown (Reference 2) to be given by

$$I = \frac{\Gamma}{2C} \phi \, e^{-\frac{c\tau}{2r}} \qquad (37)$$

In obtaining both Equation 35 and 37 the sound speed c and Gruneisen coefficient Γ were assumed to be a constant. In applying these relations to a case where both Γ and c are not constant, a more appropriate parameter to use is the effective or average value of sound speed and Gruneisen coefficient. These relations (Equation 36 and Equation 37) do provide a useful qualitative way of interpreting the effect of the sound speed and Gruneisen coefficient on the peak propagated stress and impulse for melt-dominated material response.

For the data on aluminum taken as part of this program, the deposition time (τ), range (r), and fluence (ϕ) are known to within the experimental error. The thermodynamic parameters

which to first order effect the material response are the Gruneise⁻ coefficient Γ and sound speed c.   From Equation 36 and Equation 37 it is seen that for a given deposition time an EOS model that predicts a higher value of both Γ and c may give approximately the same value for peak propagated pressure and impulse as a model that predicts a lower value of both Γ and c.

For aluminum the PHILCO-FORD EOS generally predicts the highest value of Gruneisen coefficient (Figure 15) and sound speed (Figure 17), while the GRAY EOS model generally predicts the lowest value of both Γ and c. In general the PUFF-V EOS model gives intermediate values of Γ and c. A larger value of Γ alone tends to give a larger predicted value of peak propagating stress (Equation 36) and impulse (Equation 37). However, a larger value of c tends to give a lower predicted value of peak propagating stress and impulse. The two effects tend to compensate since a higher Gruneisen coefficient combined with a higher sound speed (Equation 36 and Equation 37) may give approximately the same value of peak propagating stress and total impulse as a lower value of both Γ and c.

Thus we see that from measurements of peak propagated stress and total impulse alone it is difficult to resolve the differences between the EOS models and choose which EOS model is more appropriate. It may be pointed out that Equation 36 and Equation 37 are most applicable to melt-dominated material response. The differences in the predictions of each model for the high fluence data are discussed in the next section. As the peak stress propagates it will be attenuated, due to hydrodynamic attenuation. This attenuation tends to bring the predictions of the EOS models closer together. In other words, the model that predicts the higher peak propagating stress generally predicts a larger hydrodynamic attenuation near the front surface.

65

4.3   CRITICAL DENSITY

A comparison of the GRAY, PHILCO-FORD, and PUFF-V EOS models was also carried out for aluminum at a density of 0.6 gm/cm^3 which is near the critical density. The results of the comparison are shown in Figures 18 through 20.

Both the GRAY and PUFF-V EOS models only allow for the vapor phase to exist at this density. The PHILCO-FORD EOS model does include the vapor-liquid mixed phase region of the phase plane and allows the material to be a liquid or a mixed phase (vapor-liquid) at this density (0.6 gm/cm^3). In the PHILCO-FORD model the dividing line between a liquid and vapor is $\rho = \rho_{critical}$ (see Figure 16). The critical density for aluminum has not been experimentally determined but is on the order of 0.5 to 0.7 gm/cm^3. The PHILCO-FORD EOS model predicts a critical density of 0.56 gm/cm^3.

For a given energy density the PHILCO-FORD EOS model predicts a larger value of pressure (Figure 18), Gruneisen coefficient (Figure 19), and sound speed (Figure 20) than either the GRAY or PUFF-V EOS models. Of the three models the GRAY EOS model always predicts the smallest value for the three quantities compared. The PUFF-V EOS model predicts values that are intermediate to the other two models.

For energy densities above 3000 cal/gm the PUFF-V and PHILCO-FORD EOS models are almost equivalent. Not only do the models predict approximately the same value of pressure and pressure-energy coupling coefficient for the same internal energy density, but the slopes of the release adiabats $\left(\left.\dfrac{\partial P}{\partial v}\right|_{adiab.} = -(\rho c)^2\right)$ are also approximately the same.
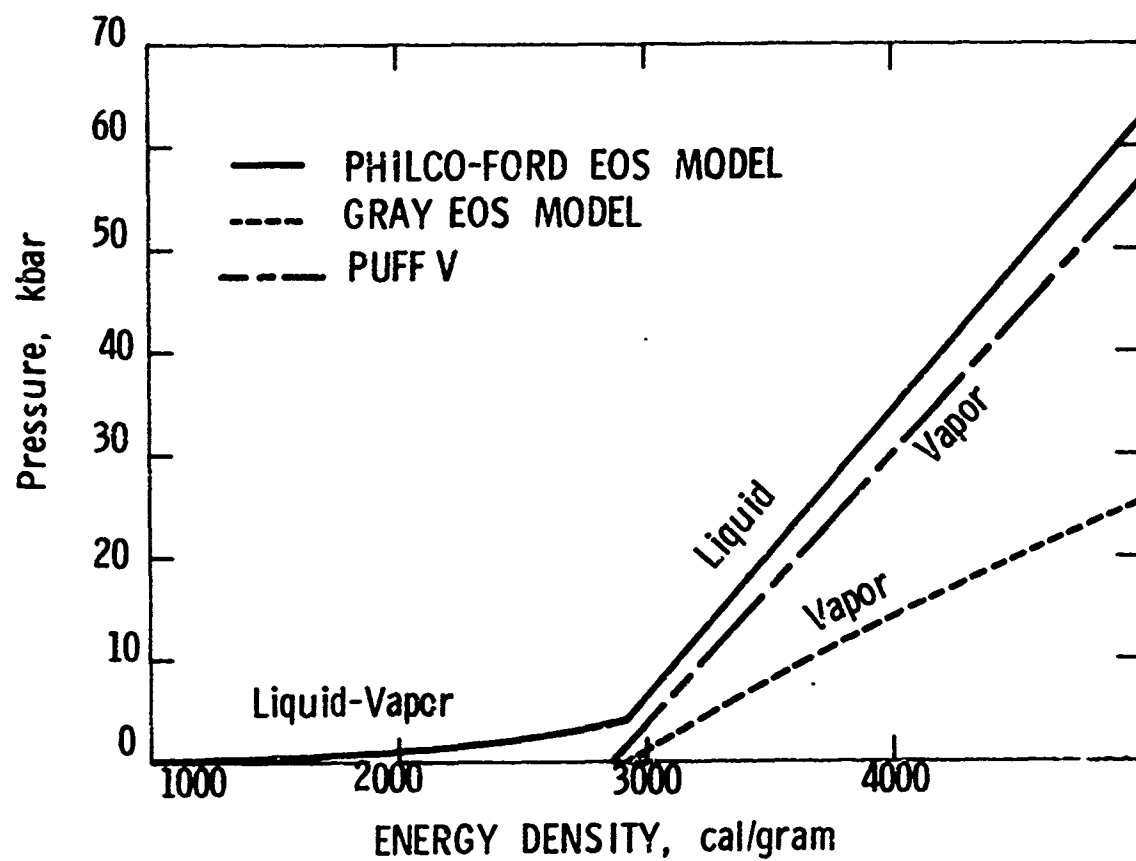
Figure 18 Comparison of predicted pressure as a function of
energy density for aluminum at a density of
$\rho = 0.6$ gram/cm³.
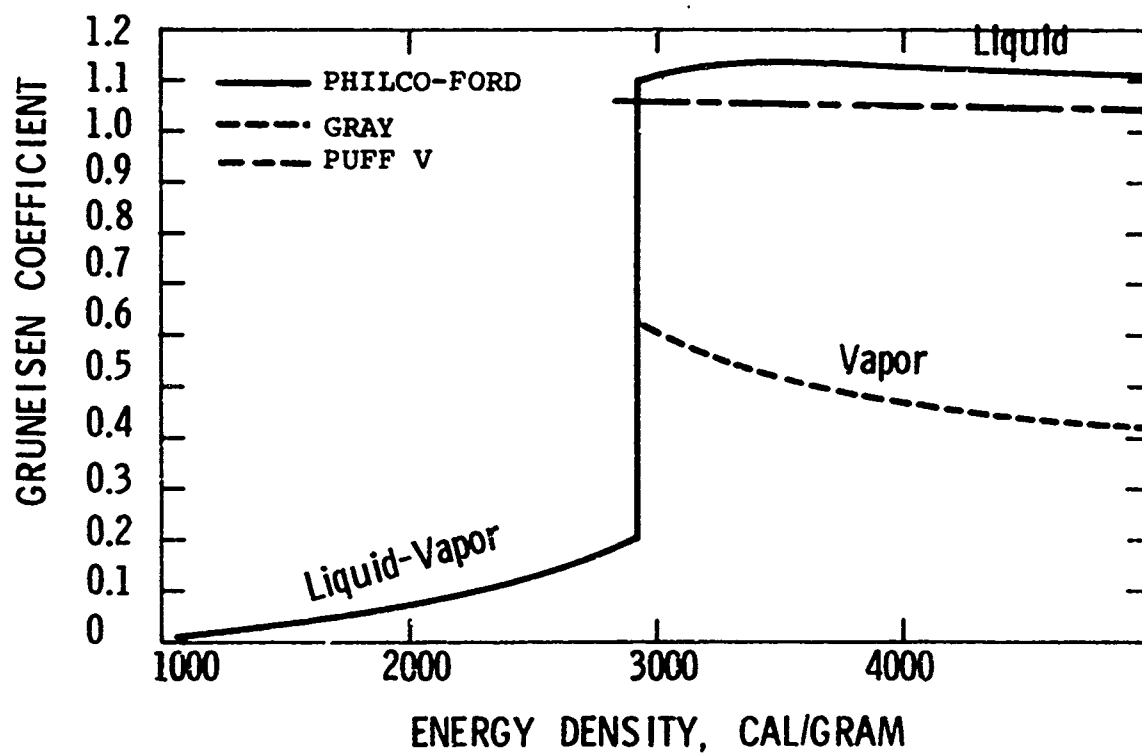
Figure 19   Comparison of Gruneisen coefficient as a function
             of energy density for aluminum at a density of
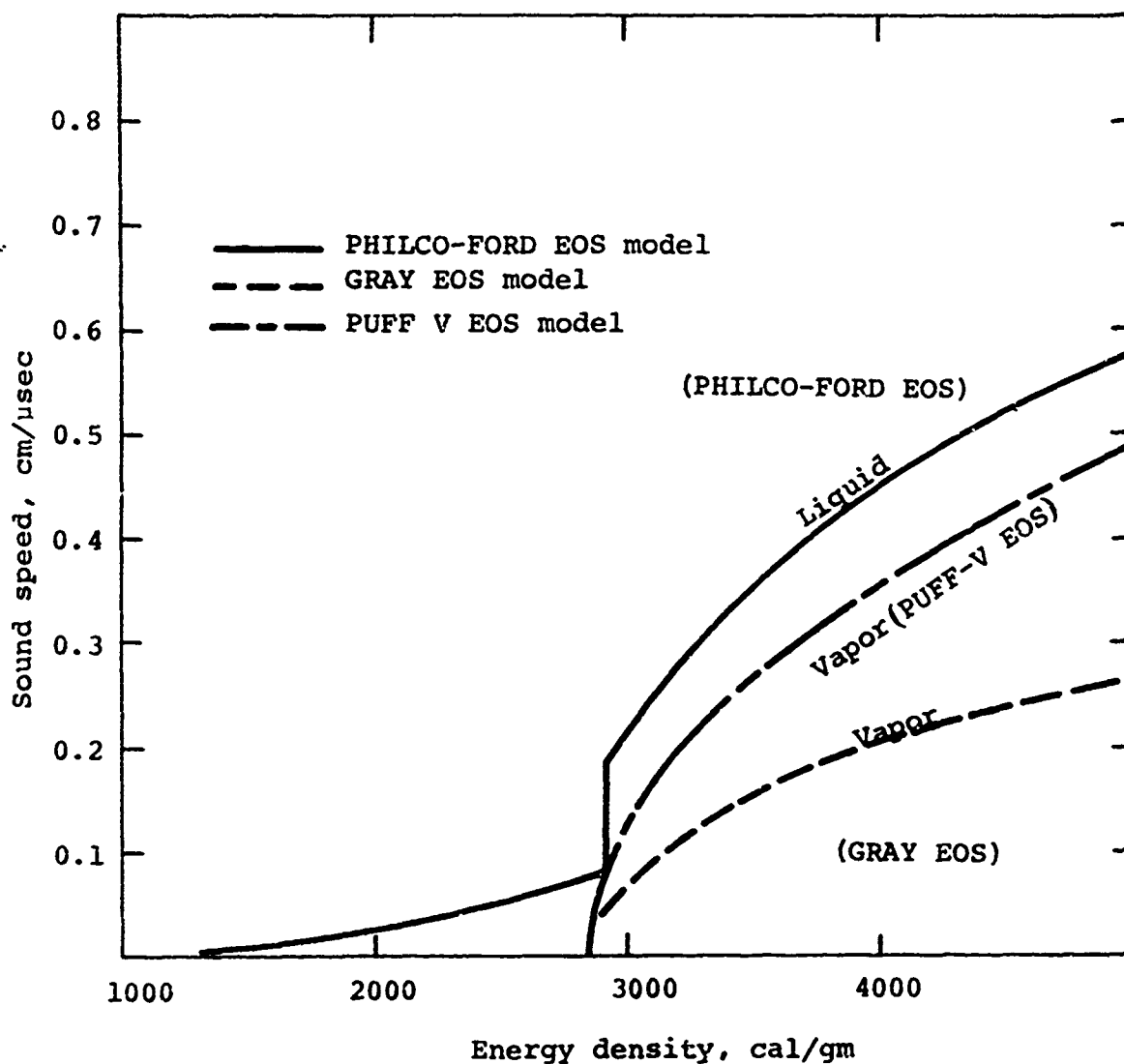 $\rho = 0.6$ cal/cm^3.

Figure 20 Comparison of predicted sound speed as a function of
energy density for aluminum at a density of
$\rho = 0.6$ gm/cm^3.

The GRAY EOS model predicts significantly lower pressures than either the PUFF-V or PHILCO-FORD EOS models.

4.4 EXPANDED DENSITY

A comparison of the three EOS models was carried out for aluminum with a density of 0.3 gm/cm^3. This density represents approximately a 9 to 1 expansion of aluminum from its reference density condition. The results of the comparison are summarized in Figures 21 through 23. The comparison follows the general trend of the two previous comparisons at a density of 0.6 gm/cm^3 and 2.71 gm/cm^3. For a given energy density the PHILCO-FORD EOS model predicts the largest value of pressure, Gruneisen coefficient, and sound speed while, of the three models, GRAY once again predicts the lowest value for the three quantities investigated.

For energy densities above 3200 cal/gm the predictions of the PUFF-V and PHILCO-FORD models are almost identical. For a given energy density greater than 3200 cal/gm, the pressure and pressure-energy coupling coefficient predicted by each model are approximately the same. Since the models also predict identical sound speeds, the slopes of the release adiabats $\left(\frac{\partial P}{\partial V} \Big|_{adiab.} = -(\rho c)^2 \right)$ are also the same for both of the models. The only difference between the two models is in the mixed phase liquid-vapor region of the phase plane.

4.5 SUMMARY

In general, for a given density and internal energy density, the PHILCO-FORD EOS model predicted higher values of pressure, Gruneisen coefficient, and sound speed than either the PUFF-V or GRAY EOS models. The GRAY EOS predicts lower values of these quantities for almost all of the range of densities and internal energy densities investigated.
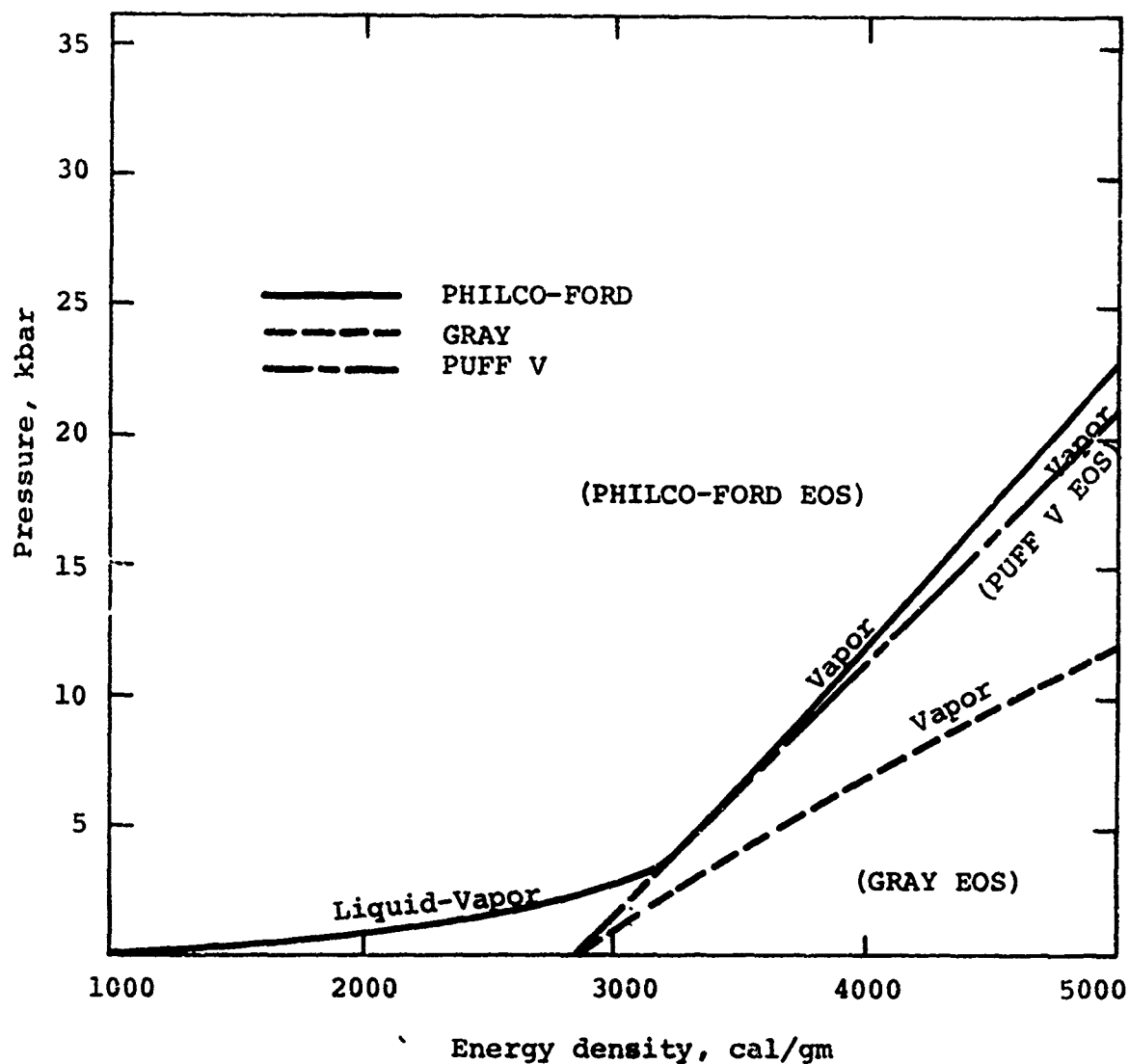
70

Figure 21 Comparison of predicted pressure as a function of
energy density for aluminum at a density of
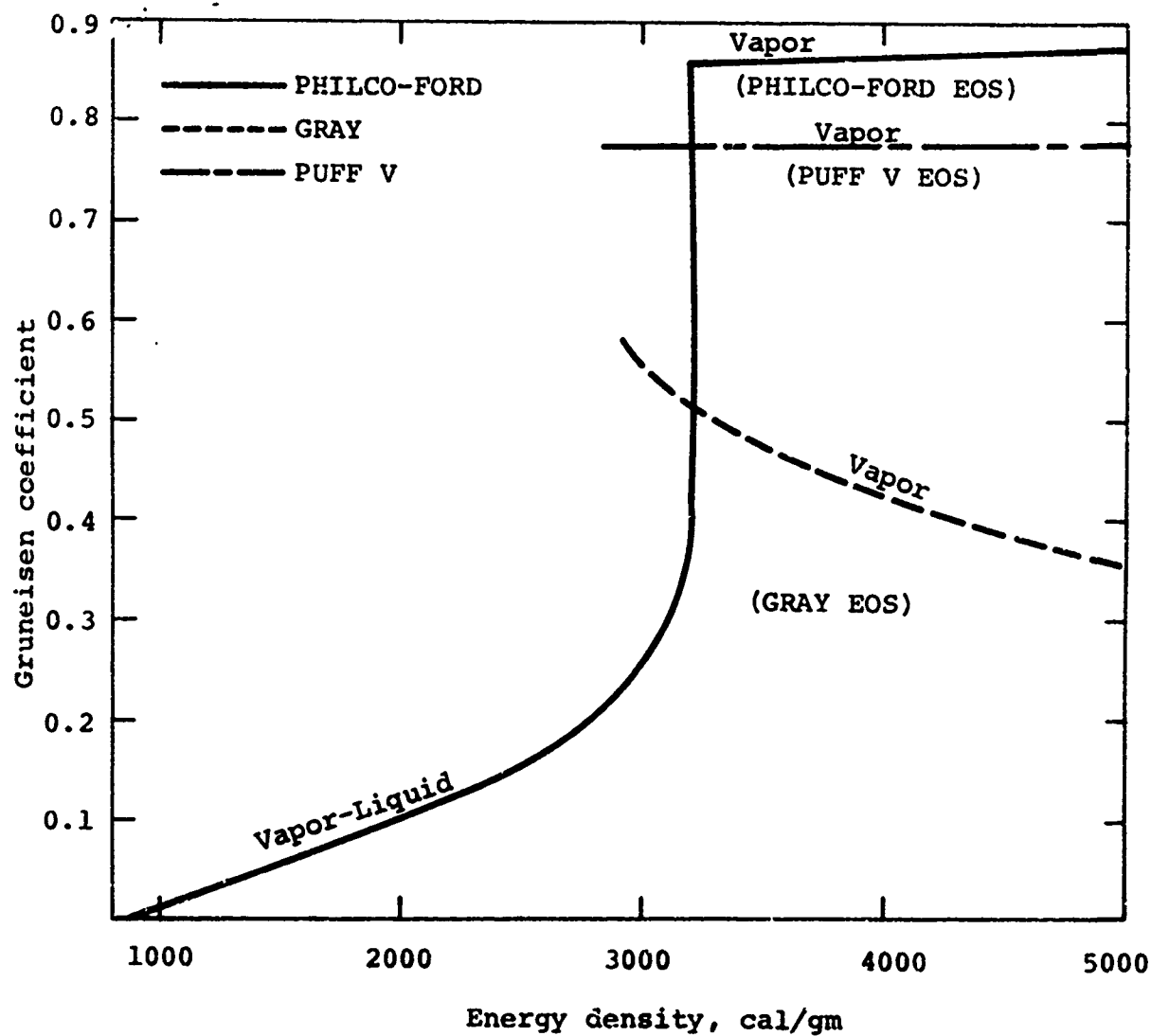$\rho = 0.3$ gm/cm^3.

71

Figure 22 Comparison of predicted Gruneisen coefficient as a
function of energy density for aluminum at a density
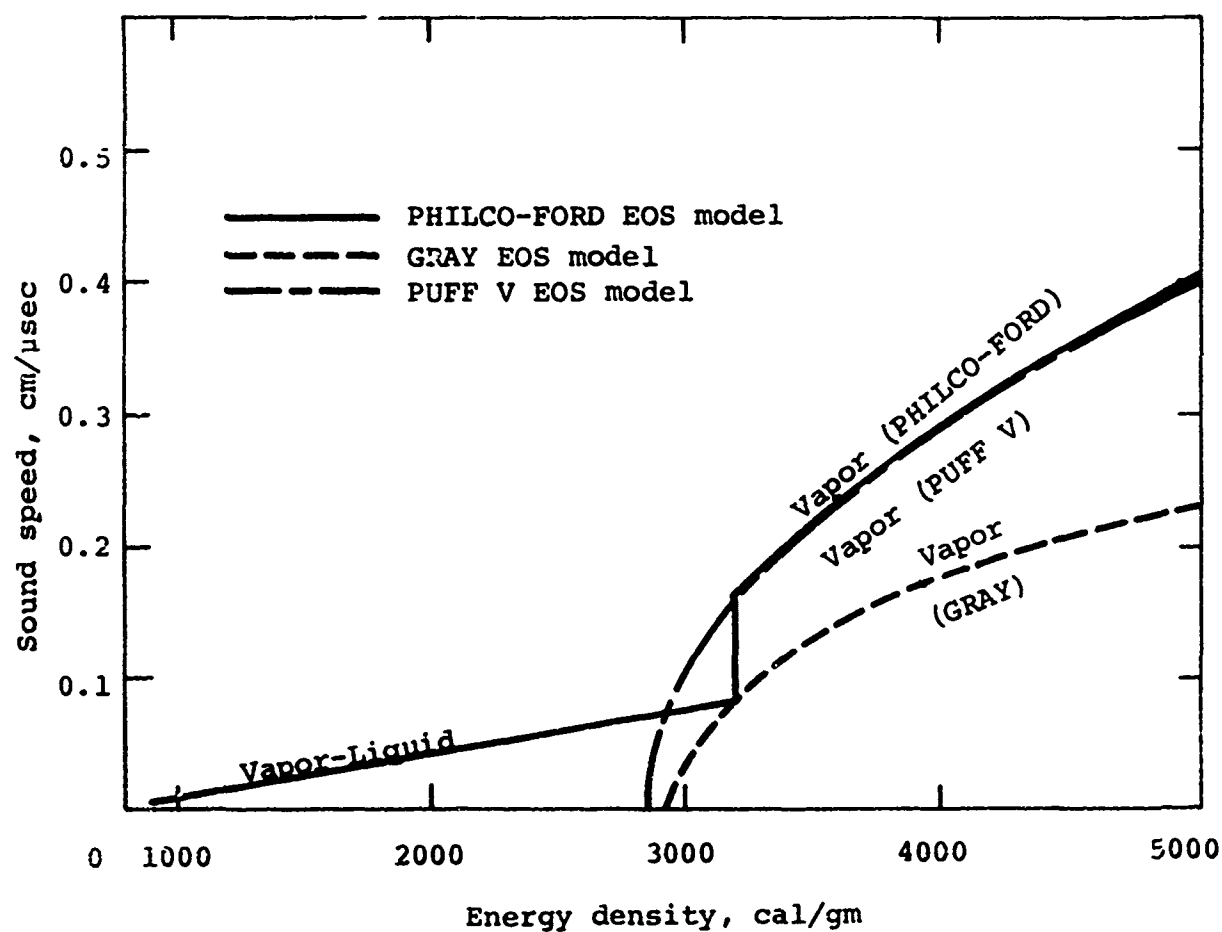of $\rho = 0.3$ cal/gm.

Figure 23   Comparison of predicted sound speed as a function of
energy density for aluminum at a density of
$\rho = 0.3$ gm/cm^3.

By examining Figures 18 through 20 and Figures 21
through 23, it can be concluded that in the case of aluminum
for densities less than 0.6 gm/cm^3 and energies greater than
3200 cal/gm the PUFF-V EOS model and the PHILCO-FORD EOS model
are approximately equivalent.

The comparison of the three EOS models did point out some
significant disagreement in the predicted values of pressure,
Gruneisen coefficient, and sound speed, especially for reference
density conditions. It was concluded that it is difficult to
resolve the differences between the EOS models and choose which
EOS model is more appropriate from measurements of peak pro-
pagated stress and total impulse alone. The differences in the
models tend to be self-compensating (see Section 4.2). It is
now possible to design special experiments to resolve some of
the differences.

SECTION 5

COMPARISON OF THE EXPERIMENTAL
DATA WITH EXISTING EQUATION-OF-STATE MODELS

The objective of this program was to investigate the
radiation-induced response of aluminum for cases where a signi-
ficant portion of the blowoff material was in the mixed
liquid-vapor phase. Figure 24 gives the deposited energy as a
function of depth in aluminum for the highest fluence condition
obtained as part of this program. Overlayed on this deposition
profile are the depths of the various phase regions as
determined from the atmospheric values of enthalpy for begin
melt, complete melt, begin vaporization, and complete
vaporization. As can be seen from Figure 24, the amount of
material that passes through the mixed liquid-vapor phase is a
large fraction of the material that is removed; (removal depth
is approximately equal to the melt depth). It must be noted
that Figure 24 uses the atmospheric values of the enthalpy for
the phase transformation, and instantaneous deposition. The
actual experimental results are for a finite deposition time
and the pressures in the heated region are greater than one
atmosphere when impulse is being generated. However, if the
results of the numerical calculations using the PHILCO-FORD EOS
model (the only model studied that contained the liquid-vapor
region) are examined, we find that Figure 24 provides a conser-
vative estimate of the amount of material which passes through
the mixed liquid-vapor phase region.

75
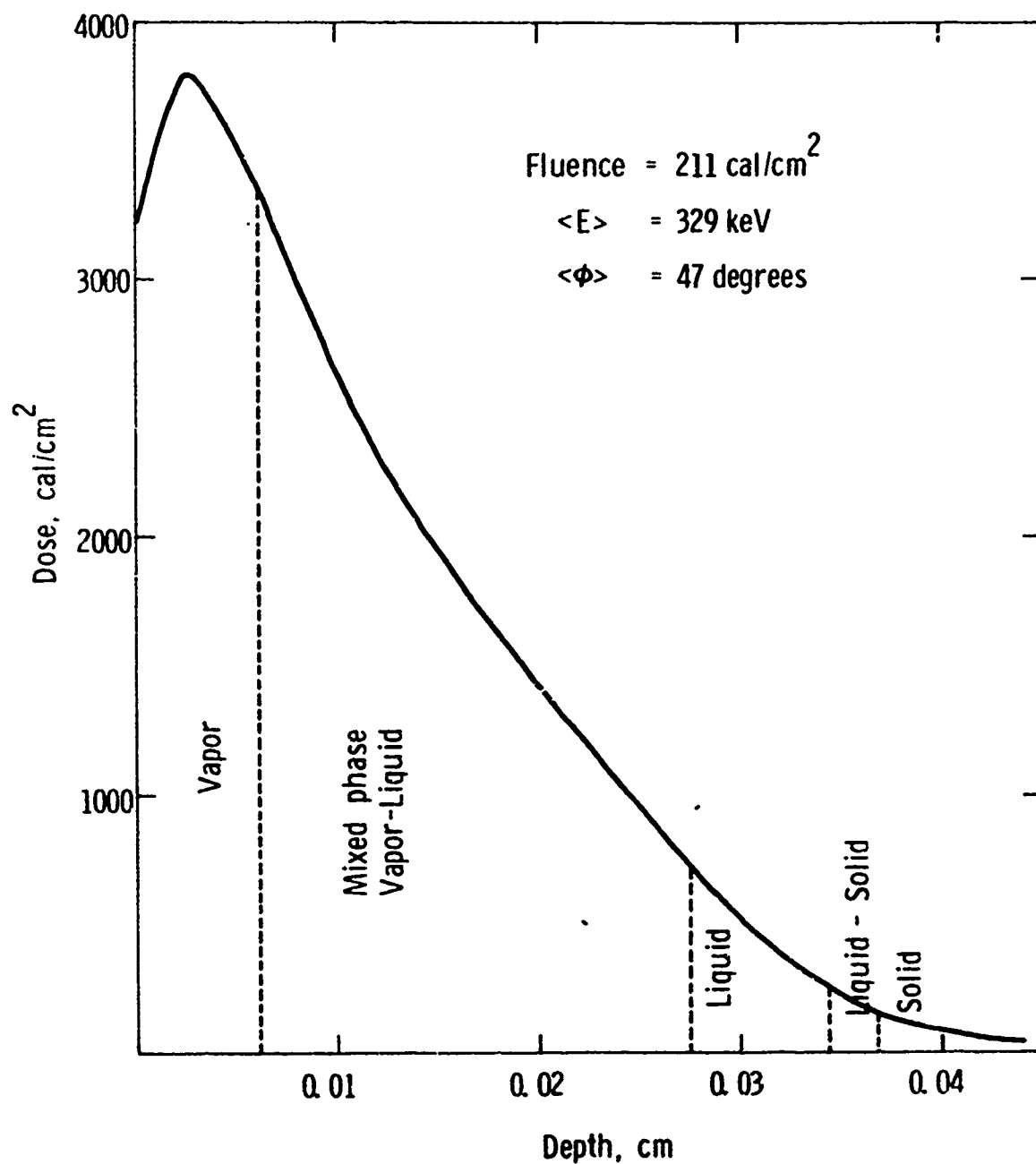
Figure 24   Depths of various phase regions in aluminum for
highest fluence condition.

For the conditions given in Figure 24 approximately 60 percent of the blowoff material is in the liquid-vapor state. If the fluence is dropped to 100 cal/cm^2 and the mean electron energy and average angle remains the same as Figure 24; approximately 60 percent of the blowoff material is still in the liquid-vapor state. This percentage drops until for a fluence of 42 cal/cm^2 only a small fraction of the blowoff material is in the liquid-vapor state.

Thus for the experimental data taken at fluences above 100 cal/cm^2, significant amounts of the blowoff material are in the liquid-vapor phase region. For the condition given in Figure 24 the peak pressure in the heated region is on the order of 260 kbar and this pressure occurs at a depth of approximately 0.017 cm. The maximum pressure of aluminum in the liquid-vapor state is on the order of 4 kbar. Thus w see that the material which had the peak pressure of 260 kbar must expand until its pressure has dropped to at least 4 kbar before it enters the liquid-vapor state. Since 4 kbar is only 1.5 percent of 260 kbar there is some question of the importance of the mixed liquid-vapor phase in determining the material response. For the experimental data taken at fluence on the order of 50 cal/cm^2 the peak pressure in the heated region is approximately 80 kbar. Even at this lower fluence the maximum pressure of the liquid-vapor state is only 5 percent of the pressure due to direct energy deposition. Thus we see that the material response of aluminum for energy loading conditions for which a significant portion of the blowoff is in the liquid-vapor state at relatively low pressures may not be dominated by mixed phase (liquid-vapor) effects, since the maximum pressure of the liquid-vapor state is only a few percent of the maximum pressure due to direct energy deposition.

The impulse data are presented in Figure 25 as a function of fluence. Also included in Figure 25 is the linear fluid model expression for impulse. The expression is included in Figure 25 to remind the reader that each impulse measurement has its individual set of loading conditions (e.g., mean electron energy, average angle of incidence, fluence, and deposition time) on which impulse generation may depend. Therefore, a plot of impulse versus fluence for the electron beam data does not give a valid representation of the scatter in the data, and such graphs can only be used to present general trends.

The mean electron energy of the flagged data point in Figure 25 was 620 keV and thus should not be considered with the other data points.

A comparison of model predictions with impulse data, generated in electron beams, must be done on a point-by-point basis since each impulse measurement has, as mentioned before, its individual set of loading conditions. From the impulse data shown in Figure 25 several representative data points were selected for a shot-by-shot comparison with the theoretical predictions using the PUFF-V, LINEAR-FLUID, GRAY, and PHILCO-FORD EOS models. The data points selected are the filled-in points in Figure 25 . The selection of a particular data point was based on the confidence of the experimentalist in the data point and in obtaining data points that spanned the range of peak doses for which data existed.

The machine diagnostics were used, as described in Reference 2, to obtain the energy spectrum, mean angle of incidence of the electrons, fluence, and effective deposition time. A Monte Carlo electron transport code was then used to calculate the deposition profile which was used in the hydrodynamic code calculations with various EOS models.

FOR MELT-DOMINATED IMPULSE, $I \sim \dfrac{\varphi \Gamma}{c} e^{-\frac{c\tau}{2r}}$
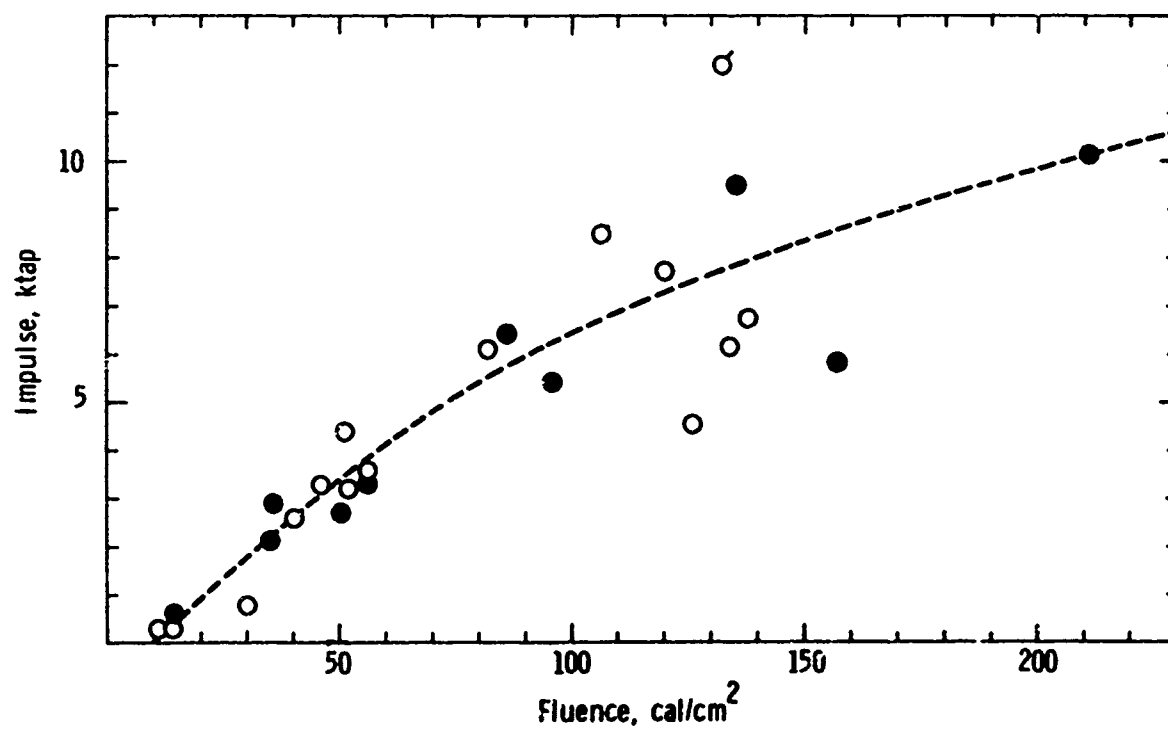
Figure 25   Impulse fluence for aluminum--mean electron energy: 200 to 402 keV.

The experimental data were compared with the prediction which used the PUFF-V, LINEAR-FLUID, GRAY, and PHILCO-FORD EOS models. For the theoretical predictions each of the EOS models was combined with a one-dimensional Lagrangian finite-difference code (PISCES 1DL).

The LINEAR-FLUID model is given in Reference 2 and summarized in Table 5.

TABLE 5

LINEAR-FLUID CONSTITUTIVE RELATIONS FOR ALUMINUM

$$P = 0.75\mu + 0.405\mu^2 + (2 + 2\mu)E, \quad \mu > 0$$

$$P = 0.75\mu \qquad\qquad + (2 + 2\mu)E, \quad \mu < 0$$

where

$$\mu = \frac{\rho}{\rho_o} - 1$$

The input parameters for the PUFF-V, GRAY, and PHILCO-FORD EOS model are given in Tables 2, 3, and 4 respectively. A von Mises yield model was used with Y_o = 2.78 kbar. The shear modulus was 277 kbar and the spall strength was -13 kbar. Both the shear modulus and spall strength decreased linearly with internal energy density and approached zero as the internal energy reached the enthalpy required to reach the melting point at one atmosphere.

The phase regions described by each EOS model are given in Table 6. It is noted that only the PHILCO-FORD EOS model attempts to describe all five phase regions (solid, solid-liquid, liquid, liquid-vapor, and vapor). The results of the comparison of the impulse data with the predictions of the four EOS models are summarized in Table 7 and Figure 26.

In Figure 26 the error bars for each data point have been retained. As the fluence increases the uncertainty in the data also increases. The main source of uncertainty in the high-fluence data is the uncertainty in the irradiated area. For the electron beam tests impulse and fluence are not measured directly. What is measured is the total energy in the beam (H) and the total momentum imparted to the sample (ΔMV) by the material that is removed. The fluence and impulse are then determined by dividing by the irradiated area A (i.e., $\phi = H/A$ and $I = \Delta MV/A$). For a given mean electron energy the total electron-beam-machine output in calories (H) remains relatively fixed. The fluence is adjusted by using the area which gives the desired fluence, ϕ ($A = H/\phi$). The data, which were taken at higher and higher fluences, are obtained by continuously reducing the area. At the high-fluence levels a relatively small uncertainty in the absolute value of the irradiated area can give an extremely large percentage uncertainty in impulse and fluence. The dependence of impulse and fluence uncertainty on the uncertainty in area of irradiation (uncertainty in crater radius) is shown in Figure 27. The area of irradiation for the high-fluence data was < 1 cm^2. From Figure 27 we see that an error of only 1 mm in determining the crater radius leads to an uncertainty of approximately 35 percent in the fluence and impulse. The obvious solution to the problem is to use larger areas of irradiation while maintaining the same fluence. With the installation of

TABLE 6

PHASE REGIONS DESCRIBED BY EOS RESPONSE MODELS

	Solid	Solid-Liquid	Liquid	Liquid-Vapor	Vapor
PUFF	X				X
PHILCO-FORD	X	X	X	X	X
GRAY	X	X	X		X
LINEAR FLUID	X		X		

TABLE 7

SUMMARY OF COMPARISON OF IMPULSE DATA WITH PREDICTIONS USING FOUR EOS MODELS

Shot	$\langle E \rangle$	$\langle \theta \rangle$ $(^\circ)$	τ (nsec)	ϕ (cal/cm^2)	Data I (ktap)	GRAY EOS Model I (ktap)	PHILCO-FORD EOS Model I (ktap)	PUFF-V EOS Model I (ktap)	Linear-Fluid EOS Model I (ktap)	Approx. Peak Dose (cal/gm)
15165	220	37	56	14±3	0.6±0.1	0.69	0.68	0.53	0.53	300
15510	301	30	38	36±5	2.9±0.4	2.43	2.57	1.97	1.98	600
12214	219	49	55	35±6	2.1±0.2	3.45	1.48	1.10	1.11	1100
12218	266	44	55	50±5	2.7±0.3	2.49	2.46	1.97	1.99	1100
15343	275	58	51	56±4	3.3±0.3	2.34	2.34	1.88	1.90	1400
15511	317	33	51	96±20	5.4±1.0	5.13	5.11	4.40	4.46	1400
14016	290	39	35	86±30	6.4±2.0	4.85	4.83	4.22	4.27	1600
14011	296	40	35	136±40	9.5±3.0	6.32	6.94	6.16	6.23	2500
15494	284	42	45	156±30	5.8±0.7	6.64	7.51	6.64	6.72	3500
15497	329	47	43	211±40	10.1±2.0	7.59	9.29	8.29	8.34	3800

83
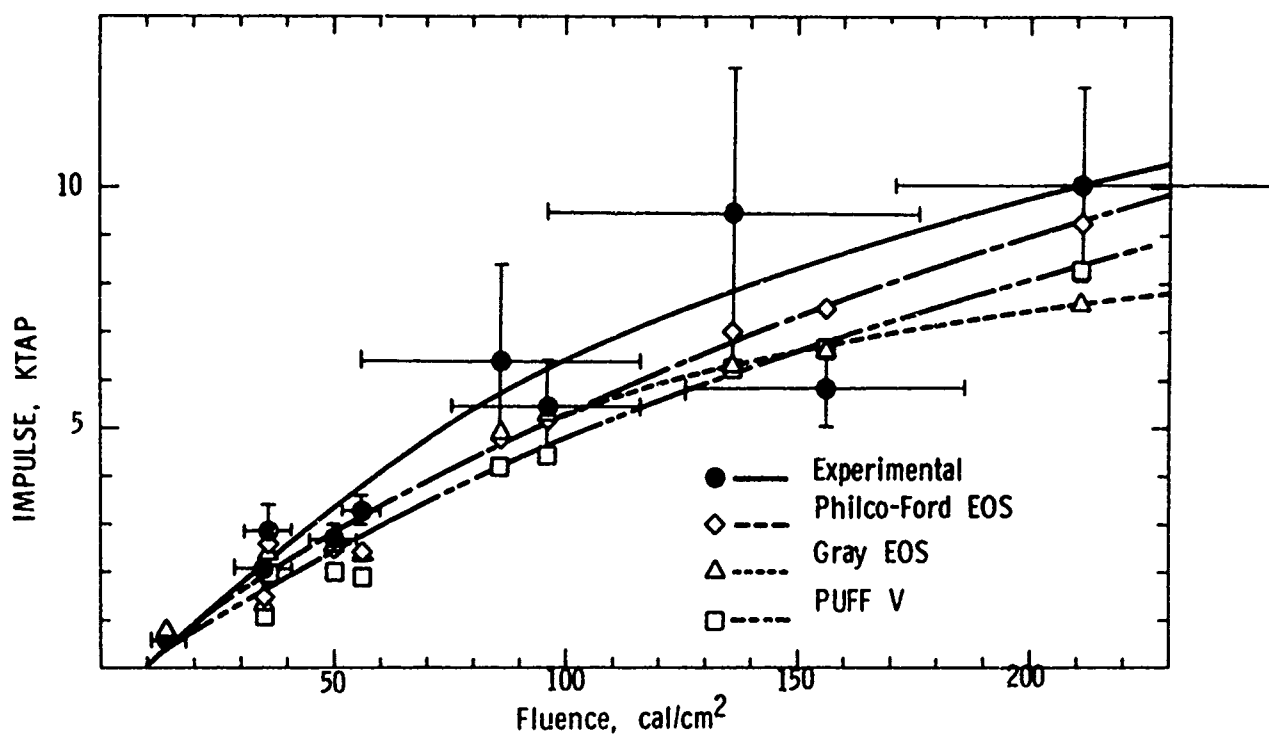
Figure 26   Comparison of predictions of various EOS models with
experimentally observed impulse in aluminum for peak
doses from 300 cal/gram to 3800 cal/gram.
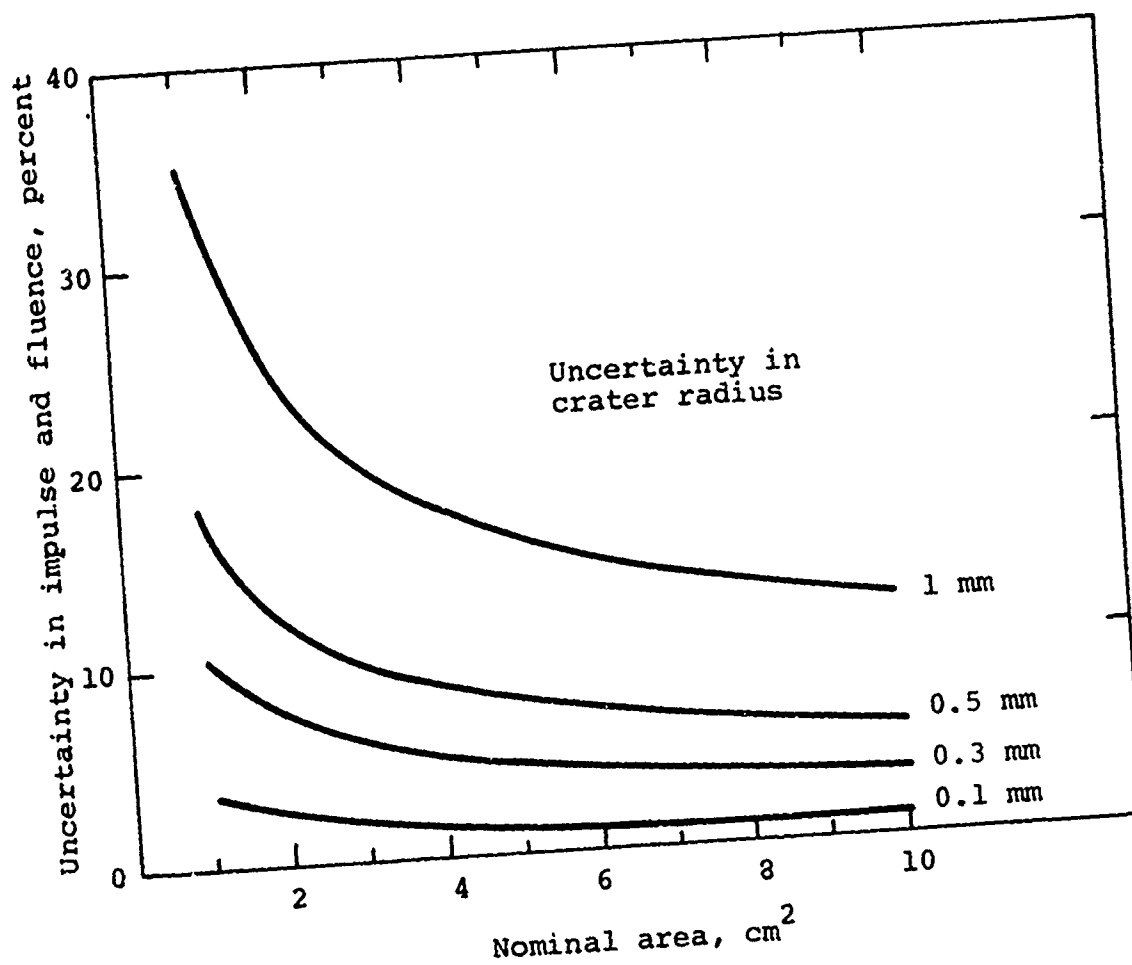
Figure 27   Effect of uncertainty in crater radius upon impulse and fluence determination.

an external-magnetic field beam-control technique on the Pulserad Model 738 (the electron beam machine on which the data for this report were taken), the desired larger areas have become available. The lines in Figure 26 are only meant to point out general trends in the comparison. As can be seen from Figure 26 the PHILCO-FORD equation-of-state model gives the best representation of the data.

In Figure 26 the predictions of the PUFF-V and LINEAR-FLUID EOS have been combined, since the impulse predictions of the two models for each data point examined are almost identical (Table 7). As shown in Table 6 the LINEAR-FLUID model does not contain provisions for treating the vapor expansion as does the PUFF-V model. The equivalence of the predictions of the two models for peak doses less than 2600 cal/gm is not surprising since it was shown in Reference 2 that the impulse is expected to be melt-dominated for peak dose up to 2600 cal/gm. However, the PUFF-V EOS model, which includes a vapor state, and the LINEAR-FLUID EOS model, which does not, predict approximately the same impulse for peak dose up to at least 3800 cal/gm. Thus we see the first evidence that even for a peak deposited energy of 3800 cal/gm, which is above the enthalpy needed to completely vaporize aluminum (3341 cal/gm) at one atmosphere, the impulse is not dominated by liquid-vapor effects. Instead, the impulse production seems to be dominated by the behavior of the EOS of aluminum in the liquid region of the phase plane (Figure 16).

For a mean electron energy on the order of 300 keV and fluences of less than 100 cal/cm^2 the GRAY and PHILCO-FORD EOS models predict approximately the same value of impulse for the same energy loading conditions. Above a fluence of 100 cal/cm^2 the predictions of the GRAY model are below those of the PHILCO-FORD model. The difference in the predictions of the two models

86

becomes larger as the fluence increases. For the highest fluence condition considered (211 cal/cm^2) the prediction of GRAY was 19 percent below that of PHILCO-FORD. The difference in the impulse predictions of the two models for fluences above 100 cal/cm^2 is probably due to the large differences between these two EOS models in the liquid region.

To investigate the reasons for the differences in predicted impulse between the two models, release adiabats from reference density were obtained for aluminum. The release adiabats from reference density with initial energy densities of 300 cal/gm, 1000 cal/gm, and 2000 cal/gm are shown in Figures 28, 29, and 30. The jump-off velocity shown in each figure is indicative of the impulse produced by each model as the material expands. The jump-off velocity is given by

$$u_{JO} = \int_0^P \left(\frac{1}{\rho c}\right) dP \bigg|_{adiab.}$$

From Figures 28, 29, and 30 it is apparent why the two models disagree in the value of predicted impulse for peak deposited energies greater than 1600 cal/gm. The jump-off velocity and the area under the p-v curve (energy converted to kinetic energy of motion) are approximately equal for the 300 cal/gm and 1000 cal/gm release adiabat. However, for the 2000 cal/gm release adiabat, the jump-off velocity and the area under the p-v curve for the PHILCO-FORD model are significantly larger than the jump-off velocity and the area under the p-v curve for the GRAY model. Thus, at an energy density somewhere between 1000 cal/gm and 2000 cal/gm the predictions of the two models should start disagreeing. The numerical comparison of the models places the onset of this disagreement to between a peak deposited energy of 1600 cal/gm and 2500 cal/gm for a mean electron energy on the order of 300 keV.

87
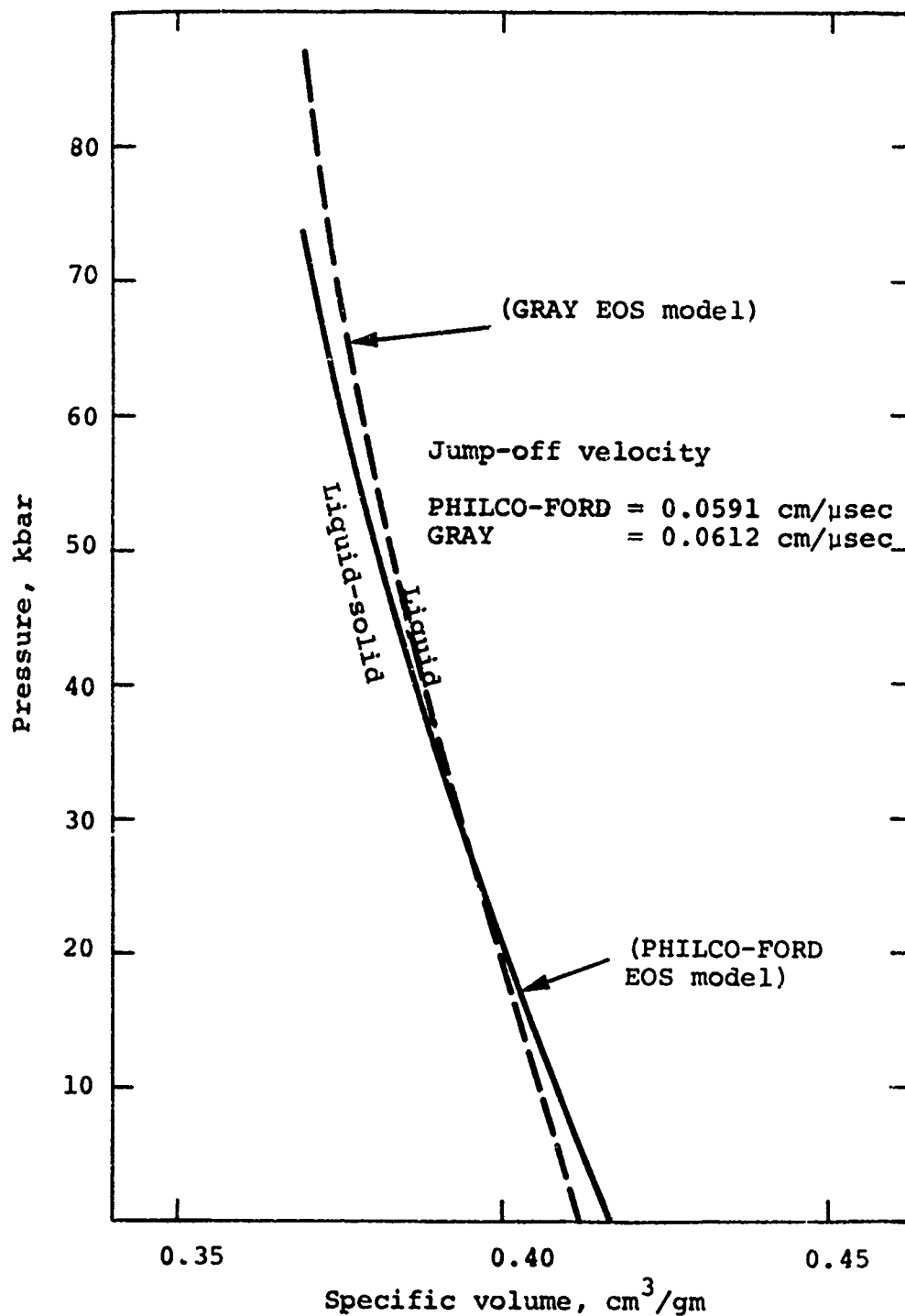
Figure 28 Comparison of release adiabat of aluminum from
reference density and an initial energy density of
300 cal/gm.
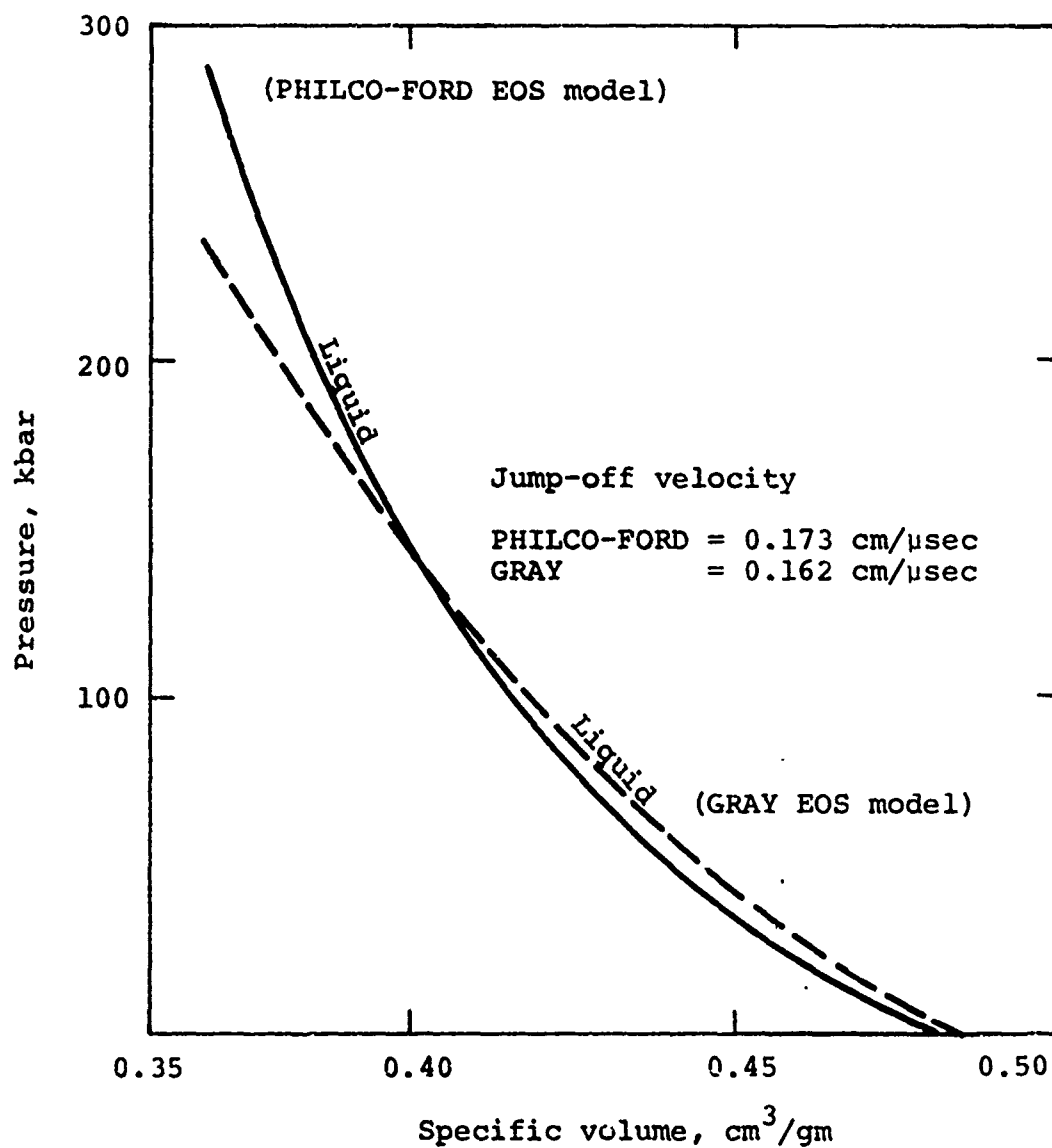
Figure 29 Comparison of release adiabat of aluminum from
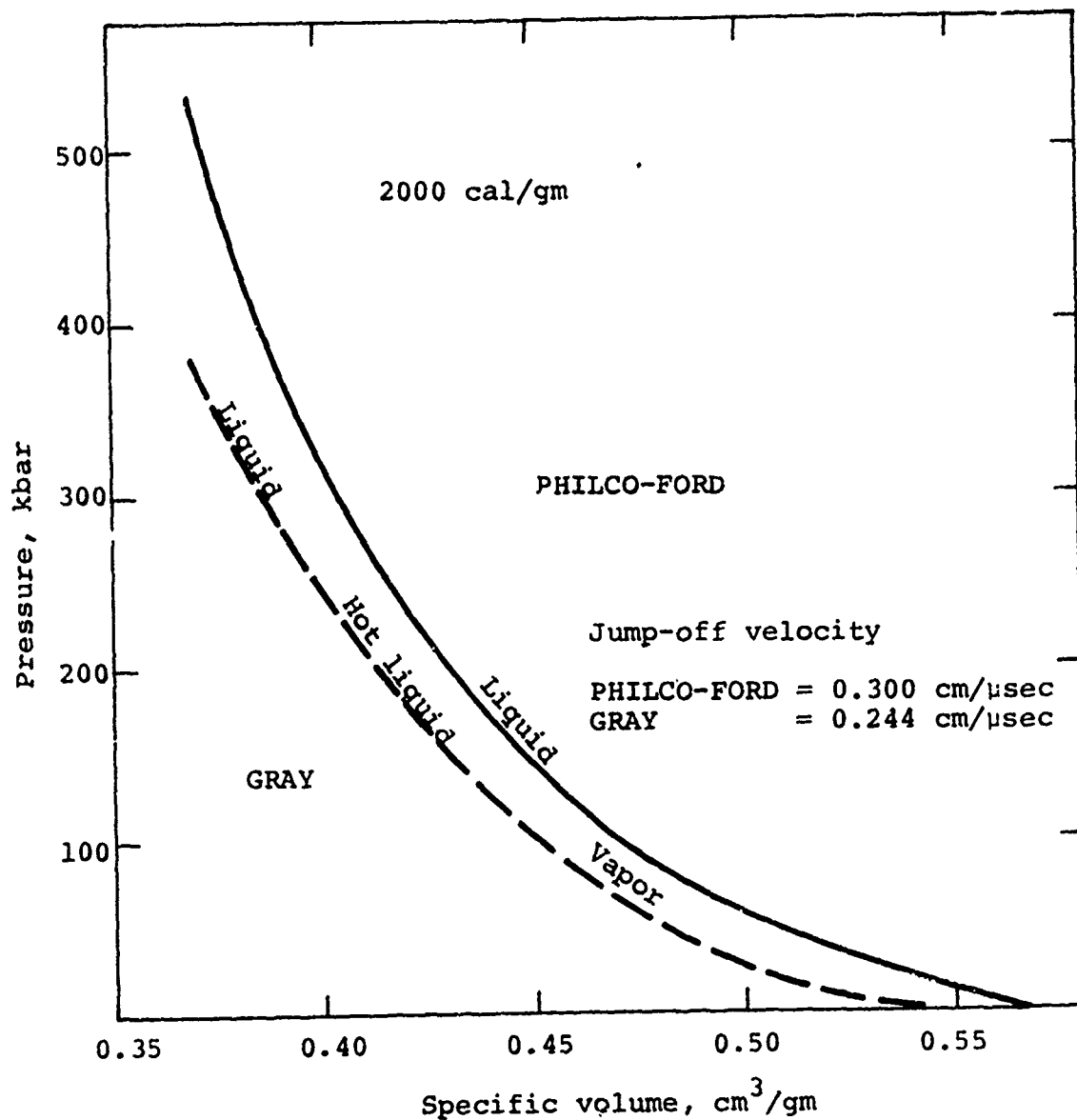reference density and an initial energy density of
1000 cal/gm.

Figure 30   Comparison of release adiabat of aluminum from reference density and an initial energy density of 2000 cal/gm.

The PUFF-V EOS model predicts lower values of impulse than the PHILCO-FORD model for all the conditions considered. For the energy loading conditions obtained in this program the PUFF-V EOS model predicts lower values of impulse than the GRAY EOS model for fluences less than 155 cal/cm^2. For fluences above 155 cal/cm^2 GRAY predicts lower values of impulse than PUFF-V.

The agreement of the predicted impulse for the LINEAR-FLUID and PUFF-V EOS models for all the data considered was the first indication that the impulse is not dominated by liquid-vapor or vapor effects for deposited energies up to 3800 cal/gm. Another indication was that for all the cases considered numerically, impulse production ceased when the material spalled. This was independent of the EOS which was used when the nominally recommended input values for the EOS models were used (Table 2 through 5).

The largest impulse delivery time, according to the numerical calculations, was 117 nanoseconds (approximately three times the deposition time) and was obtained with the PHILCO-FORD model for the 211 cal/cm^2 (peak dose 3800 cal/gm) data condition. The impulse delivery time for materials such as SC-1008 which have vapor-dominated impulse for comparable energy loading conditions is on the order of a few microseconds (Reference 14).

In order to investigate which region of the phase dominates the material response behavior, the 211 cal/cm^2 data condition was examined in more detail with the PHILCO-FORD EOS model. The peak deposited energy for this condition is approximately 3800 cal/gm. Figure 31 shows the release adiabat from reference density for aluminum with an initial energy density of 4000 cal/gm using the PHILCO-FORD model. As the material expands it does

91
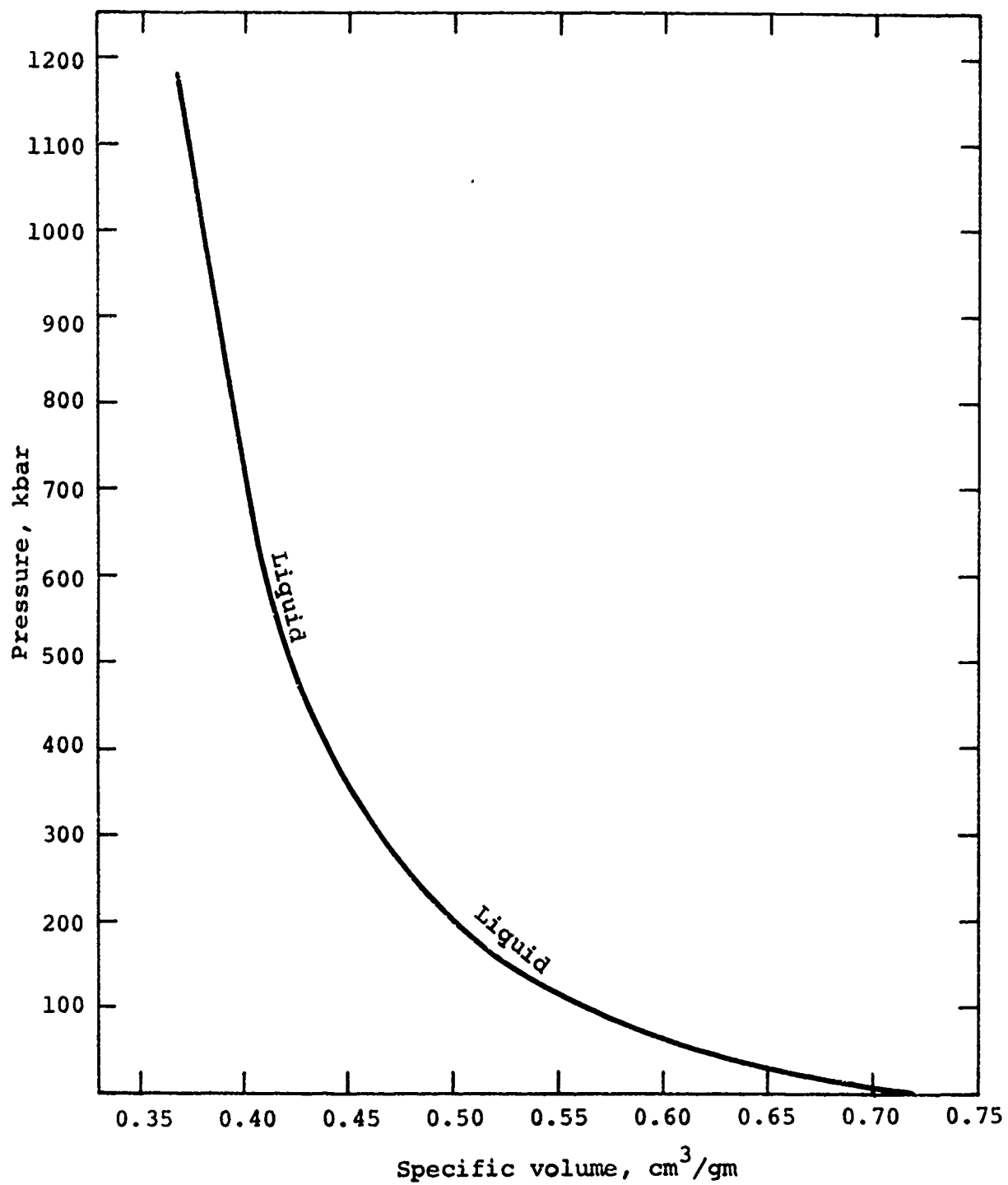
Figure 31 Release adiabat of aluminum from reference density and an initial energy density of 4000 cal/gm using the Philco-Ford EOS model.

enter the liquid-vapor state but at an energy density of approximately 2000 cal/gm and a pressure of 1.3 kbar. Thus we see that the liquid-vapor region of the phase plane does not dominate the release adiabat behavior. Instead the release adiabat behavior is dominated by the behavior of the material in the liquid phase. As used in this report the term liquid phase denotes the region of the phase plane denoted as liquid in Figure 16. At the extreme pressures and energy densities in which we are interested, the terms liquid and vapor lose their significance. It is more appropriate to refer to a region of the phase plane.

The hydrodynamic code calculation for the 211 cal/cm^2 condition using the PHILCO-FORD model provides additional information on the importance of the liquid-vapor state. According to the calculation at a time of 51 nanoseconds after irradiation begins (deposition time is 46 nanoseconds) all the material except for the first zone in the calculation is in the liquid, liquid-solid, or solid state. The delivered impulse is 7.63 kilotaps. This is to be compared with the total impulse of 9.29 kilotaps for an infinite time. Thus we see that at least 82 percent of the impulse is delivered while the material is in the liquid, liquid-solid, or solid state. The maximum internal energy density from the calculation is approximately 3100 cal/gm since the material near the front surface expands significantly during the deposition time. Thus we see that, according to the PHILCO-FORD model, the impulse production seems to be dominated by the behavior of the EOS of aluminum in the liquid region of the phase plane (Figure 16).

The GRAY EOS model contains a parameter a_y, the coefficient of attractive potential for the vapor, which can be adjusted to evaluate the importance of the vapor and of having a good equation of state in critical region.* As suggested by Royce, a_y in GRAY was reduced by a factor of 3. The reduced a_y was used to calculate the response of the 211 cal/cm^2 condition. The total impulse increased from 7.59 kilotaps to 11.6 kilotaps which represents an increase of 53 percent in impulse by decreasing a_y by a factor of three. This seems to indicate that a good equation is required in the critical region. However, it must be kept in mind that the definition of a vapor in GRAY is the condition that the specific volume $V > 1.32 \ V_o$. Also GRAY with the nominal value of a_y predicts much lower pressures than the other models (Figures 14, 18, and 21). Another interesting phenomenon occurs for the 211 cal/cm^2 condition when a_y is reduced by a factor of three in the GRAY EOS. A double wave structure develops in the propagated stress pulse. The development of the double wave structure is shown in Figure 32. The upper portion of Figure 32 is for a time of 51 nanoseconds after the start of irradiation. The normal compressive pulse is followed by a strong rarefaction which is followed by another compression-rarefaction wave. The first strong rarefaction moves into the body and causes a spall to develop in the liquid-solid phase; (note that the spall strength was set equal to zero for material in the liquid-solid phase). The second compressive pulse recompresses the spalled material and then propagates into the sample (lower portion of Figure 32).

The question which immediately arises is the following: Is there any experimental evidence of the existence of the double wave structure discussed above? Several laser interferometer measurements were made with thin aluminum samples (30 to 50 mils) bonded to a 1-inch thick buffer of GE type 151 fused silica. A

---

*This is suggested by Royce in Reference 10.

94
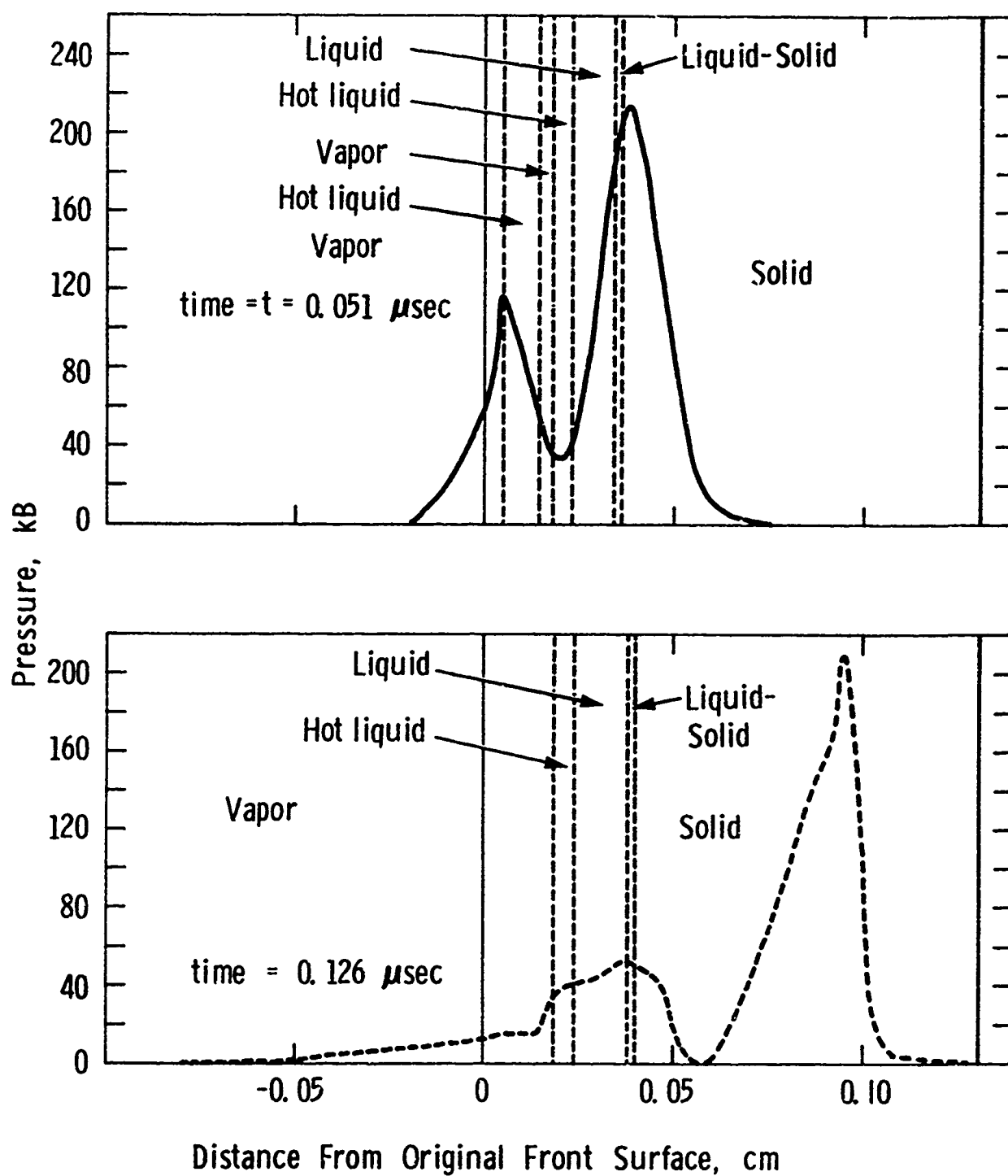
Figure 32   Development of the double wave structure, GRAY EOS.

reflecting surface was put on the fused silica by vapor depositing aluminum on the front surface of the fused silica which was then bonded to the aluminum. The interface velocity was then monitored with the laser interferometer. The electron beam machine diagnostics were not complete enough to allow a detailed reduction of the data. However, the laser interferometer data are interesting. One of the reduced traces is shown in Figure 33. There are two distinct peaks in the stress-time profile. All of the interferometer data taken at the high fluences show evidence of the second peak in stress time. The second peak was generally of larger relative amplitude than shown in Figure 33 and occurred at a time such that the second pulse could not be explained by the reverberation of the initial stress pulse within the sample. The separation in time of the two peaks was approximately the same as predicted by the numerical calculations. While the experiments are not definitive, they do provide some supporting evidence of the existence of the double wave structure.

The Chart D Analytic Equation of State, Reference 15 has not been included in the comparisons. This EOS model is a multi-constituent model which may provide a reasonable alternative to the EOS models considered in this report.
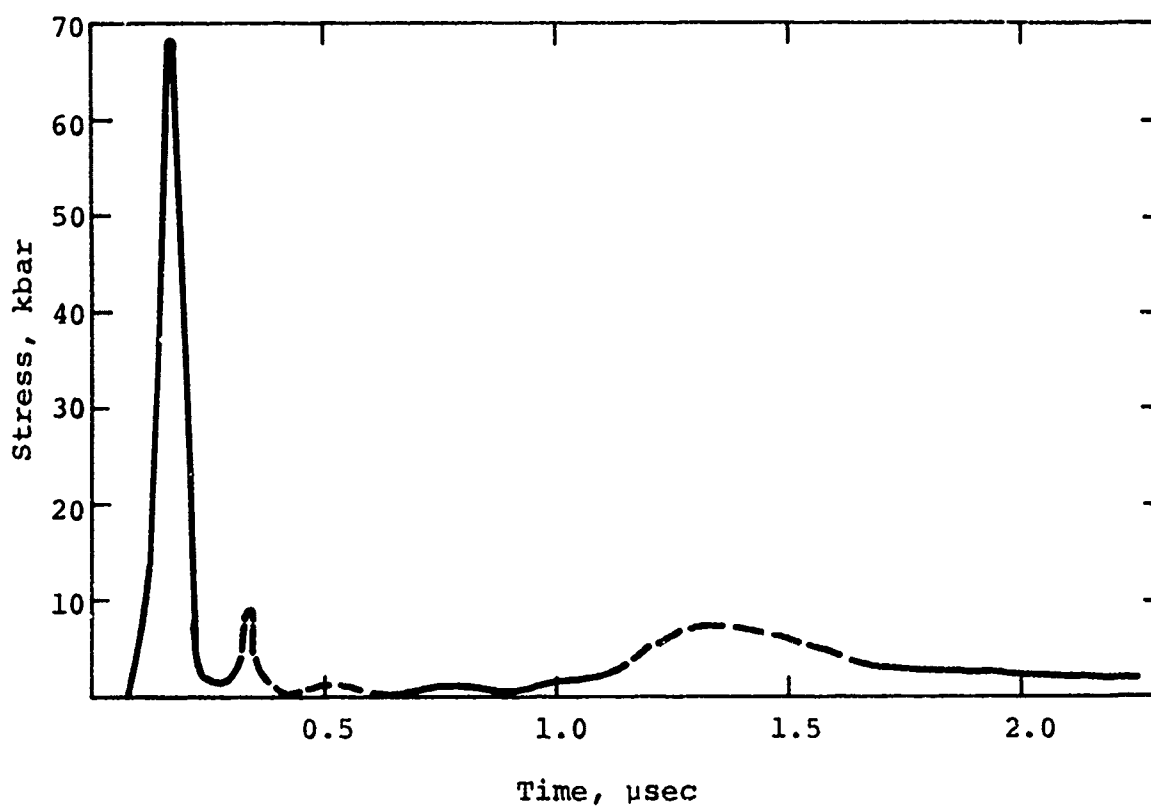
Figure 33   Stress-time profile in aluminum obtained with a
laser interferometer.

SECTION 6
CONCLUSIONS

The objective of this program was to experimentally and
theoretically investigate the radiation-induced impulse and
stress generation characteristics of aluminum for cases where a
significant portion of the blowoff material was in the liquid-
vapor state.

Experimental data were obtained in the laboratory for con-
ditions in which significant amounts of the blowoff material
were in the liquid-vapor state. Impulse measurements were
obtained with a ballistic pendulum for peak doses up to
3800 cal/gm. Manganin gauges and the laser interferometer were
used to obtain stress time records adjacent to the region of
energy deposition.

The PUFF V, GRAY, and PHILCO-FORD equation-of-state models
were compared for aluminum. The experimental data were compared
with the predictions of these equation-of-state models plus the
LINEAR-FLUID model. The PHILCO-FORD equation-of-state model
gave the best data representation. The PUFF V model and the
LINEAR FLUID model were found to give approximately the same
results for the same input conditions.

Examination of the comparisons of the data with the
equation-of-state models provided evidence that the material
response of aluminum for the energy loading conditions obtained

in this program, in which a significant portion of the blowoff was in the liquid-vapor state at relatively low pressures, was not dominated by mixed phase (liquid-vapor) effects. This was because the maximum pressure of the liquid-vapor state is only a few percent of the maximum pressure due to energy deposition. The impulse in aluminum for the experimental conditions obtained in the program seems to be dominated by the behavior of the equation-of-state of aluminum in the liquid region (see Figure 16 for definition of liquid region) of the phase plane.

The laser interferometer data for the high-fluence conditions and the predictions of the GRAY equation-of-state model suggest the possible existence of a double wave structure in the propagated stress pulse. This phenomenon was attributed to the recompression of the liquid layer by the overlying vapor layer after the initial drop to zero pressure in the liquid.

With the installation of an external-magnetic-field beam-control technique on the pulsed electron beam accelerators larger areas and higher peak deposited energies have become available. The larger areas will lead to smaller error bars on the data (Figure 26) and longer one-dimensional read times. Specially designed experiments could be used to investigate the questions which remain unanswered after this program. Some of these remaining questions are

a. Is the pressure-energy coupling coefficient of reference density aluminum at internal energy densities above 2500 cal/gm 0.67 as predicted by GRAY or ~2.5 as predicted by the PHILCO-FORD model?

b. Does the double wave structure really exist for high enough fluences?

c. Can the melting and vaporization phase transformations really occur on the tens of nanosecond time scale and what is their effect on the material response?

d. What is the equation of state of aluminum around the critical region?

This program has concluded that the material response obtained on solid aluminum was not dominated by liquid-vapor effects. However, this is not expected to be the case for porous metals. In the case of porous metals the material response may be dominated by the behavior of the material in the liquid-vapor regime. The importance of this mixed phase region will increase as the porosity increases. Thus, if the material response of porous metals is to be understood, a well planned theoretical and experimental investigation to determine the equation of state of metals around the critical region must be carried out.

REFERENCES

1. A. Lutze and G. Yonas, _Techniques Used in Impulse Experiments_, PIQR-144-2, Physics International Company, San Leandro, California, December 1969.

2. J. Reaugh, A. Lutze and G. Yonas, _Melt-Dominated Impulse Experiments and Calculations_, DASA-2475, Physics International Company, San Leandro, California, September 1970.

3. G. Yonas, P. Spence, B. Ecker and J. Rander, _Dynamic Effects of High ν/γ Beam Plasma Interactions_, DASA 2426, Physics International Company, San Leandro, California, August 1969.

4. A. Lutze, _Preheated Aluminum Impulse Generation and Dynamic Response of Rings_, PIFR-235, UCLRL 13488, Physics International Company, San Leandro, California, November 1970.

5. L. K. Goodwin, L. A. Johnson, and R. S. Wright, _An Equation of State for Metals_, DASA-2286, Aeronutronic Division of Philco-Ford Corporation, Newport Beach, California, April 1969.

6. J. O. Hirschfelder, R. J. Buehler, H. A. McGee, Jr., and J. R. Sutton, "Generalized Equation of State for Gases and Liquids," Ind. and Eng. Chem., 50, p. 375 (1958).

7. J. O. Hirschfelder, R. J. Buehler, H. A. McGee, Jr., and J. R. Sutton, "Generalized Thermodynamic Excess Functions for Gases and Liquids," Ind. and Eng. Chem., 50, p. 386 (1958).

8. J. O. Hirschfelder, et al., "Corrections to Generalized Equation of State and Generalized Thermodynamic Excess Functions," I & EC Fundamentals, 1, p. 224 (1962).

REFERENCES (cont.)

9. R. Grover, "Liquid Metal Equation of State Based on Scaling," J. Chem. Phys., 55, 3 35 (1971).

10. E. B. Royce, Implementation of GRAY, a Three-Phase Equation of State for Metals, Lawrence Livermore Laboratory, Rept. UCID-15871 (1971).

11. E. B. Royce, GRAY, A Three-Phase Equation of State for Metals, Lawrence Livermore Laboratory, Rept. UCRL-51121 (1971).

12. D. A. Young and B. J. Alder, "Critical Point of Metals from the van der Waals Model," Phys. Rev. A3, 364 (1971).

13. A. Mazzella and J. Shea, Dynamic Response of Porous Materials to Electron Beam Deposition, AFWL-TR-71-146, Air Force Weapons Laboratory, New Mexico, June 1972.

14. M. Rosen, V. Bailey, and C. Felts, Experimental Determination of Blowoff and Sublimation Energy (U), PIFR-321, Physics International Company, San Leandro, California, July 1972.

15. S. L. Thompson and H. S. Lauson, Improvements in the Chart D Radiation-Hydrodynamic Code 111: Revised Analytic Equations of State, SC-RR-710714, Sandia Laboratories, Albuquerque, New Mexico, March 1972.

APPENDIX A

APPLICATION OF CALORIMETERS AND FARADAY CUPS

AS FLUENCE DIAGNOSTICS

The two most commonly used devices to diagnose the total energy deposited in targets by electron beams are the total absorbing carbon calorimeter and the Faraday cup charge collector. The topic of this discussion is not to discuss their designs but to point out benefits and disadvantages of both devices.

Segmented calorimeters provide the experimenter with the most reliable existing gauge of fluence uniformity. The segments have been made small enough to fit many into irradiation areas which are typical of today's electron beams. Assuming that all the incident beam energy is deposited in the calorimeter, this device becomes a useful tool in measuring the incident fluence and its spatial distribution provided the deposited energy stays in the calorimeter long enough to communicate the accompanying temperature rise to the attached thermocouples. Since the thermocouples must be attached outside the energy deposition region, the calorimeter is usually slow to react. Thus, if a fraction of the deposited energy is suddenly removed before its temperature rise is "sensed" by the thermocouple, the resulting fluence map will be misleading.

Open-shutter photographs of attempted high-fluence measure-meants using segmented graphite calorimeters (Figure A-1) as well as active area erosion suggest that (hot) material is removed during fluence measurements for which the graphite sublimation energy and/or spall strength is exceeded.

Neglecting removal by spallation (which may be aggravated by moisture absorbed in the porous graphite), vapor blowoff from the active area of a calorimeter is capable of carrying away substantial energy which cannot be communicated to the thermo-couples monitoring temperature changes in the calorimeter array.

105
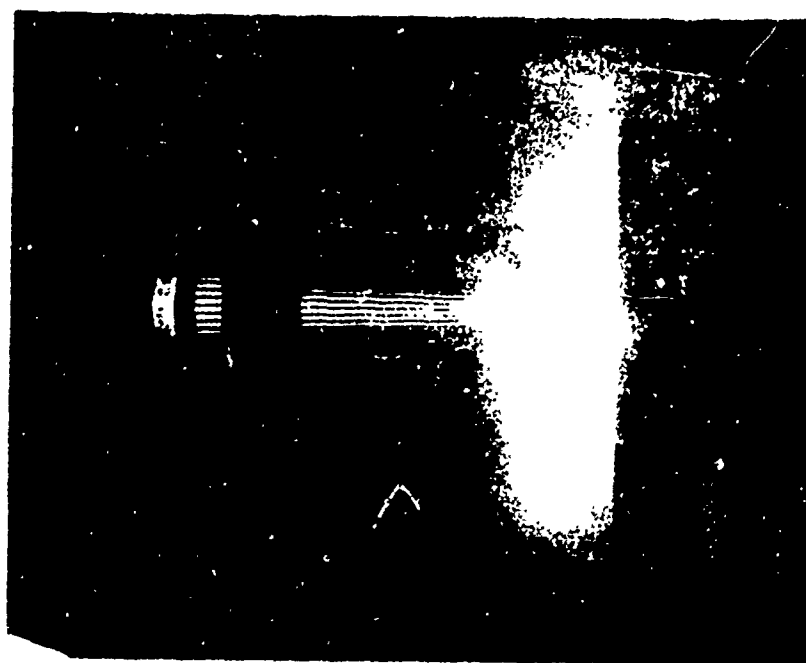
Figure A-1   Before and after photographs of high-flux measurements using graphite calorimetry.

Graphite sublimation energy appears to be approximately 1500 cal/gm. Whenever graphite calorimeters are used to measure fluences in excess of that dose, the measured fluence is likely to be less than the deposited. The following example illustrates the extent of the under measurement for doses in excess of 1500 cal/gm.

The typical normalized peak dose, E_o^{max}, for beams with mean electron energy of 260 keV is 26 cal/gm/(cal/cm^2). With a graphite sublimation energy, E_{sub}, of 1500 cal/gm, the deposited fluence, ϕ_{Dep}, for which graphite just begins to vaporize is

$$\phi_{Dep} = \frac{E_{sub}}{E_o^{max}} = \frac{1500}{26} = 58 \text{ cal/cm}^2$$

Thus, for deposited fluences less than 58 cal/gm^2 (at 260 keV) the graphite calorimeter can be expected to measure all of the deposited fluence.

Figure A-2 illustrates the situation for deposited fluences above 58 cal/cm^2.

In this case, graphite will be removed by vaporization to a depth, r, at which the dose is 1500 cal/gm--i.e.,

$$E_{Sub} = \phi_{Dep} E_o(r)$$

The area under the non-normalized deposition profile is the deposited fluence. The deposited energy corresponding to the unshaded area in Figure A-2 is carried away by the vaporized material. The remaining energy (shaded area) is communicated to thermocouples which monitor each block of the array (Reference 1).

107
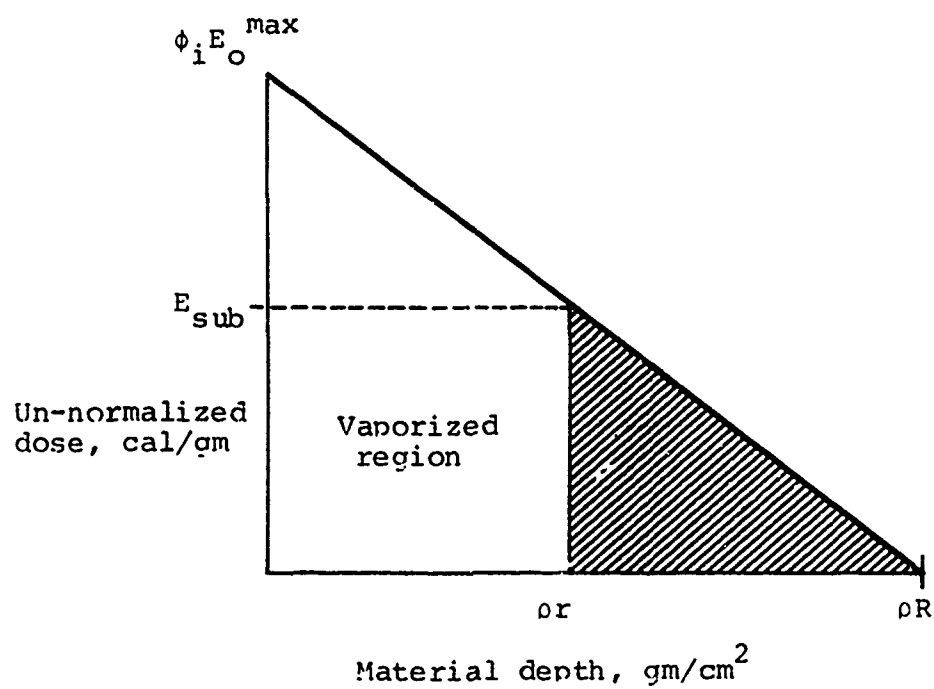
Figure A-2   Deposition profile with peak dose greater than E_{sub} (graphite sublimation energy).

From the geometry in Figure A-2,

$$\frac{E_{Sub}}{\rho(R-r)} = \frac{\phi_{Dep} E_o^{Max}}{\rho R}$$

so that the apparent fluence measured in the calorimeter is

$$\phi_{Meas} = \frac{1}{2} \rho(R-r)E_{Sub} = \frac{\rho R(E_{Sub})^2}{2\phi_{Dep} E_o^{Max}} \text{ for } \phi_{Dep} > 58 \text{ cal/cm}^2$$

In general, graphite calorimeter fluence measurements performed with beams typified by a 260 keV mean electron energy will results in measured fluence.

$$\phi_{Dep}, \text{ for } \phi_{Dep} \leqslant 58 \text{ cal/cm}^2$$

$$\phi_{Meas} = \frac{\rho R(E_{Sub})^2}{2\phi_{Dep} E_o^{Max}}, \text{ for } \phi_{Dep} > 58 \text{ cal/cm}^2$$

The measured fluence is plotted against deposited fluence in Figure A-3 for mean electron energies of 220, 260, and 300 keV. The maximum in each of the three curves identifies the critical deposited fluence beyond which calorimeter graphite is removed by vaporization. Thereafter, measured fluence decreases with increasing deposited fluence.

109
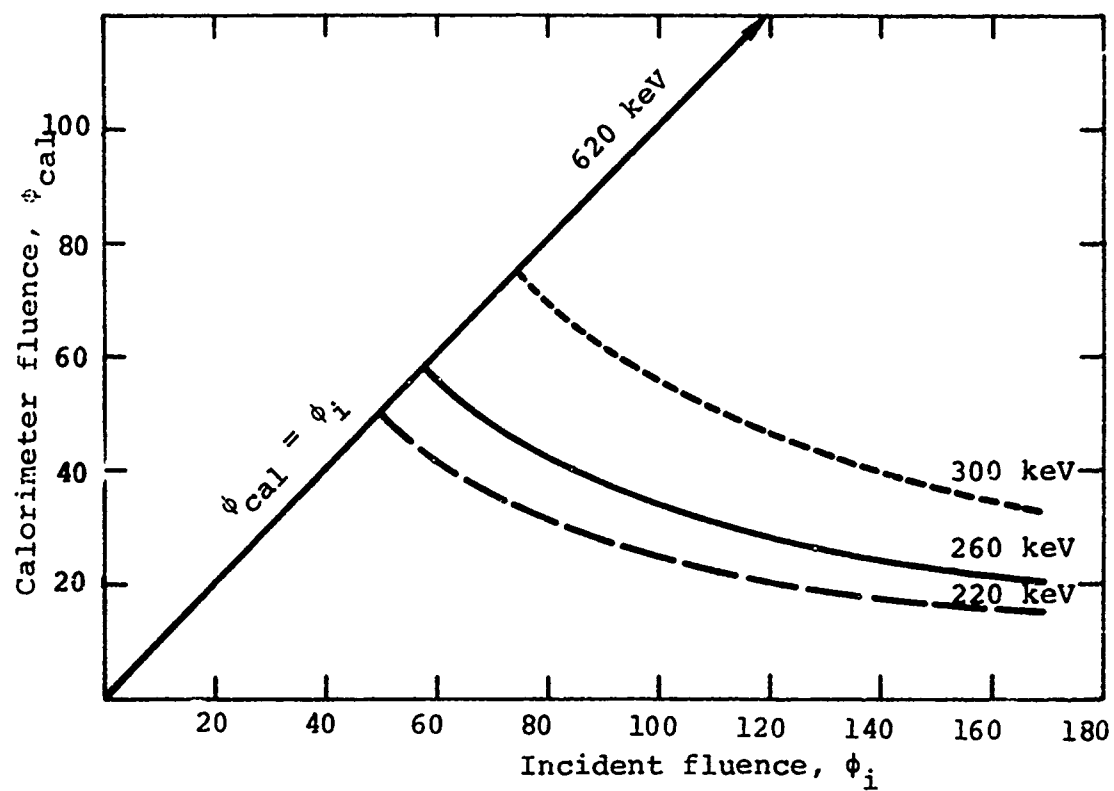
Figure A-3 Graphite calorimeter fluence versus incident fluence.

As mentioned earlier, the 1500 cal/gm limit is an upper
bound beyond which graphite calorimetry should not be used.
Front-surface spall and the eruptive effect when moisture within
the graphite pores changes phase suggest that graphite calori-
meters may not be accurate above 1000 cal/gm.

Although this limitation is disappointing, the graphite
calorimeter is none the less a useful tool for low-dose work.
It is still the only diagnostic capable of quantitative spatial
resolution of the deposited energy. Furthermore, since calori-
metry data is fast to reduce, it provides on-the-spot fluence
data during the course of an experiment.

Measurements of the total beam energy under high-dose con-
ditions are performed using the outputs of the diode voltage
monitor and a Faraday cup as detailed in Reference 1. Integra-
tion under the power curve yields the total beam calories de-
posited in the Faraday cup

$$H = \frac{1}{4.186} \int V(t) \, I_{FC}(t) \, dt$$

Because the Faraday cup measures current, it is insensitive
to vaporization or front-surface spall of its collector. The
penalty, in this case, is the lengthy and tedious process of
converting oscilloscope traces into power curve integrals.

The disadvantage of both the carbon calorimeter and the
Faraday cup techniques is that neither accounts for the energy
back-scattered out of the measurement device. The remainder of
this section will be devoted to methods of accounting for the
back-scattered energy, at least, to a reasonable approximation.

111

It will be argued later that the waveform (shape) of the incident current is similar to the current absorbed by the Faraday cup. This circumstance makes the input to the Monte Carlo electron deposition code not an unreasonable one even in view of backscatter. The input requires only the current time dependence, not its absolute magnitude, in addition to the accelerating voltage waveform and the mean incidence angle of the beam electrons. In short, the code "sees" a primary current waveform (from the Faraday cup) not unlike the (unmeasured) incident primary current, together with the voltage history which accelerated the (unmeasured) incident primary current. In addition to its main function of calculating the energy deposition profile, the code calculates the fraction of incident energy back-scattered, $\langle \beta \rangle_\tau$, as well as the percent of incident electrons back-scattered, $\langle \alpha \rangle_\tau$. Both $\langle \alpha \rangle_\tau$ and $\langle \beta \rangle_\tau$ are given as averages over the entire beam pulse. Figure A-4 demonstrates that both quantities have weak dependence on mean electron energy but strong dependence on the mean incidence angle of the beam electrons in the range of interest for this program.

Since calorimeters measure the absorbed energy over the entire pulse, the pulse-averaged $\langle \beta \rangle_\tau$ is appropriate and the back-scatter correction is trivial once the mean incidence angle is known. If H_{inc} is the energy incident on a calorimeter, H_{cal}, the absorbed and H_{ref} the back-scattered energy, then

$$H_{inc} = H_{cal} + H_{ref}$$

$$\langle \beta \rangle_\tau \equiv \frac{H_{ref}}{H_{inc}}$$

112
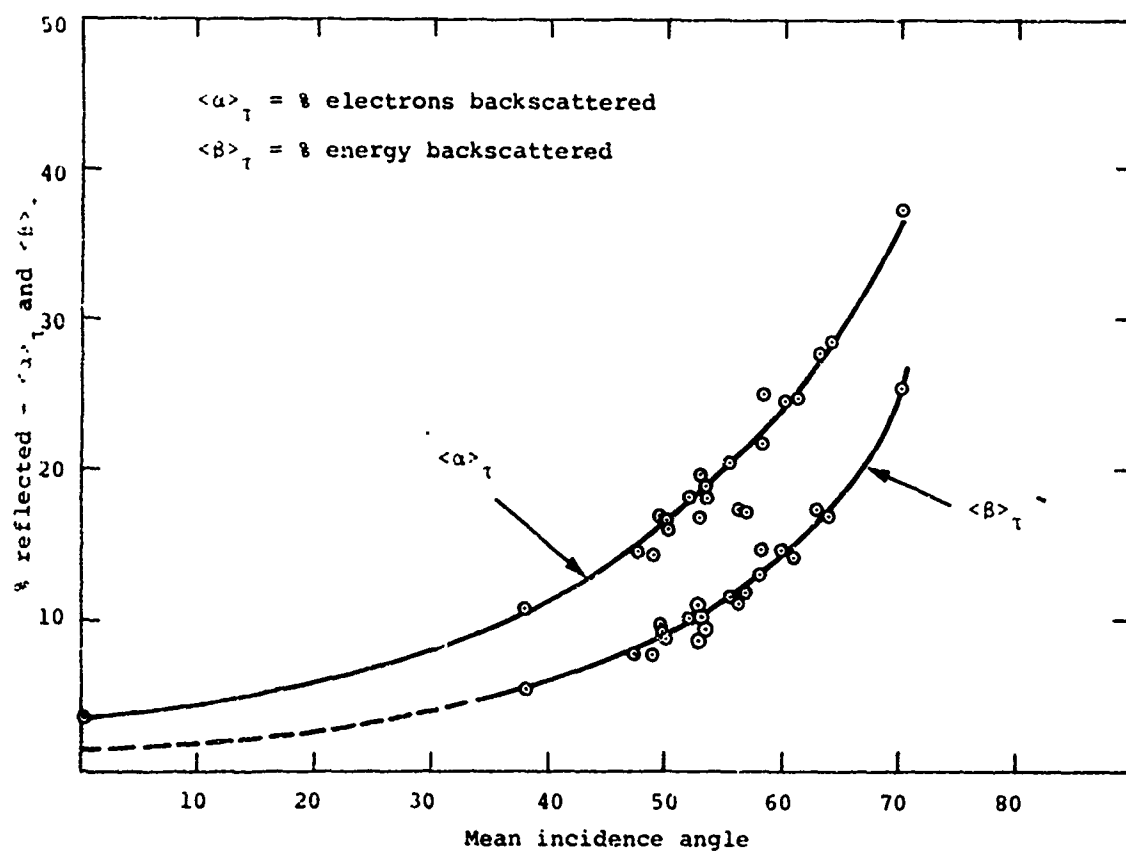
Figure A-4 Backscatter in graphite, 205 ≤ <E> ≤ 434.

Figure A-4 Backscatter in graphite, 205 ≤ <E> ≤ 434.

so that

$$H_{inc} = \frac{H_{cal}}{1-\langle\beta\rangle_\tau} \ .$$

Knowledge of the mean incidence angle defines $\langle\beta\rangle_\tau$ (see Figure A-4) and the back-scatter correction is completed.

Since the voltage time history of the back-scattered electrons is unknown, a $\langle\beta\rangle_\tau$ -correction cannot be applied to the power curve integral. However, an attempt can be made to account for backscatter using the fraction of electrons back-scattered.

V(t) in the power curve integral needs no correction since it already describes the accelerating voltage of the (unmeasured) incident primary current. The inadequacy arises when the primary current absorbed in the Faraday cup, $I_{FC}(t)$, is used in lieu of the unmeasured incident primary current, $I_{inc}(t)$. If $I_{ref}(t)$ represents the current associated with the back-scattered electrons, then

$$I_{inc}(t) = I_{FC}(t) + I_{ref}(t)$$

where each of the three currents could have a different time dependence. If $\alpha(t)$ is the fraction of incident electrons

reflected at any time, t, in the beam pulse, then

$$\alpha(t) = \frac{I_{ref}(t) \, dt}{I_{inc}(t) \, dt}$$

and

$$I_{inc}(t) = I_{FC}(t) + \alpha(t) \, I_{inc}(t)$$

where

$$I_{inc}(t) = \frac{I_{FC}(t)}{1-\alpha(t)}$$

This general statement is still not useful since only $I_{FC}(t)$ is known from the Faraday cup measurement.

If it can be shown that $\alpha(t)$ is reasonably constant over the beam pulse, the backscatter correction is made possible by using

$$\alpha(t) = \text{constant} = <\alpha>_{\tau}$$

$$H_{inc} = \frac{1}{4.186} \int V(t) I_{inc}(t) \, dt = \frac{1}{4.186} \int V(t) \, \frac{I_{FC}(t)}{1-<\alpha>_{\tau}} \, dt$$

$$I_{inc} = \frac{1}{4.186 \, (1-<\alpha>_{\tau})} \int V(t) I_{FC}(t) \, dt$$

115

A constant $\alpha(t)$ requires that the three currents $I_{inc}(t)$, $I_{FC}(t)$, and $I_{ref}(t)$ all have the same waveform and differ only in amplitude. The similarity of time dependence (shape) cannot be directly verified since $I_{inc}(t)$ is not measured at the Faraday cup location. However, the unmeasured incident primary current, $I_{inc}(t)$, is generated in the diode where the diode current is monitored by a B-probe (Reference 1). Figure A-5 illustrates that the current absorbed in the Faraday cup, $I_{FC}(t)$, has a shape similar to that of the diode currents which is the initial shape of the incident primary current, $I_{inc}(t)$. Since even the oscillatory structure is the same in the two waveforms, it is reasonable to assume that (to a good approximation) the diode current changes only in amplitude and beam front erosion as it propagates toward the Faraday cup to become the unmeasured $I_{inc}(t)$. Thus, $\alpha(t)$ appears to be very nearly constant over the beam pulse and

$$H_{inc} = \frac{1}{4.186} \frac{1}{(1-<\alpha>_\tau)} \int V(t) I_{FC}(t) \, dt$$

becomes a reasonable backscatter correction provided the mean incidence angle of the beam electrons, $<\theta>$, is known in order to define the appropriate $<\alpha>_\tau$ in Figure A-4.

Reference 3 gives an expression of $<\theta>$ in terms of the primary beam current, I_{PR}, its relativistic $\beta\gamma$ and the current neutralization factor, $(1-fm)$, defined as the ratio of net to primary current amplitudes. The equation, derived from magnetic
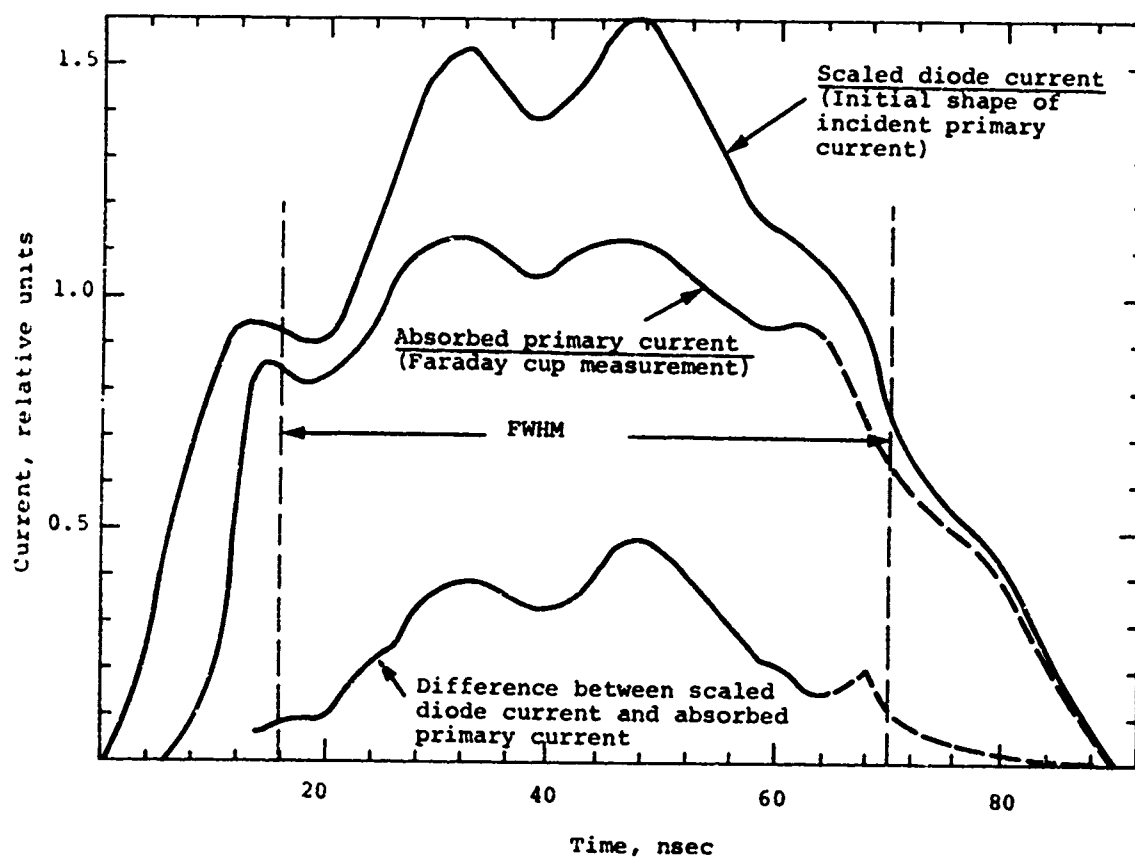
Figure A-5   Comparison of current waveforms.

117

pressure balance, is

$$\tan^2 \langle\theta\rangle = \frac{2}{\sqrt{\left[\dfrac{34 \, \beta\gamma}{I_{PR}(1-fm)^2}\right]^2 + 1} - 1}$$

The backscatter correction given above complicates matters since now

$$I_{PR} = I_{inc} = \frac{I_{FC}}{1-\langle\alpha\rangle_\tau}$$

whereby the $\tan^2 \langle\theta\rangle$ expression becomes one equation in two unknowns--i.e., $\langle\theta\rangle$ is needed to define $\langle\alpha\rangle_\tau$ and $\langle\alpha\rangle_\tau$ is needed to calculate $\langle\theta\rangle$.

The only recourse is to adopt an iterative procedure taking advantage of the fact that $\tan^2 \langle\theta\rangle$ is a slow-varying function of $\langle\alpha\rangle_\tau$.

The backscatter corrections described in this appendix were applied to the data taken as part of this program.

118

APPENDIX B

LASER INTERFEROMETER SYSTEM

118A

SECTION B-1
LASER VELOCIMETER

The Physics International laser interferometer system is designed to measure the response of materials to electron beam deposition or mechanical shock loading. Basically, it records the time-velocity and time-position profile of the rear surface of a sample under test. This surface may be either free or in contact with a suitable buffer material such as fused silica or lucite. To date, measurements have been made on aluminum, sparesyl, fused silica, Comrad I fiber bundles, and several phenolics with excellent results. Electron beam conditions range from front surface deposition to uniform deposition throughout the thickness of the sample. Measured velocities have ranged between 5 m/sec and 650 m/sec with accuracies on the order of 0.1 percent.

An outline of the optical configuration used in this system is shown in Figure B-1. The beam from an argon ion laser is reflected from the rear surface of the sample. As the surface accelerates under shock loading conditions, the reflected beam is given a phase shift and a Doppler shift due to the surface displacement and velocity, respectively. Optical interference is used to measure the size of these shifts. Part of the return beam is combined with a static reference beam for displacement information and the remainder of the beam is split; part of it is delayed prior to recombination to measure velocity. Upon recombination, the relative intensity of each beam is proportional to the cosine of the relative phase angle. The intensities

119
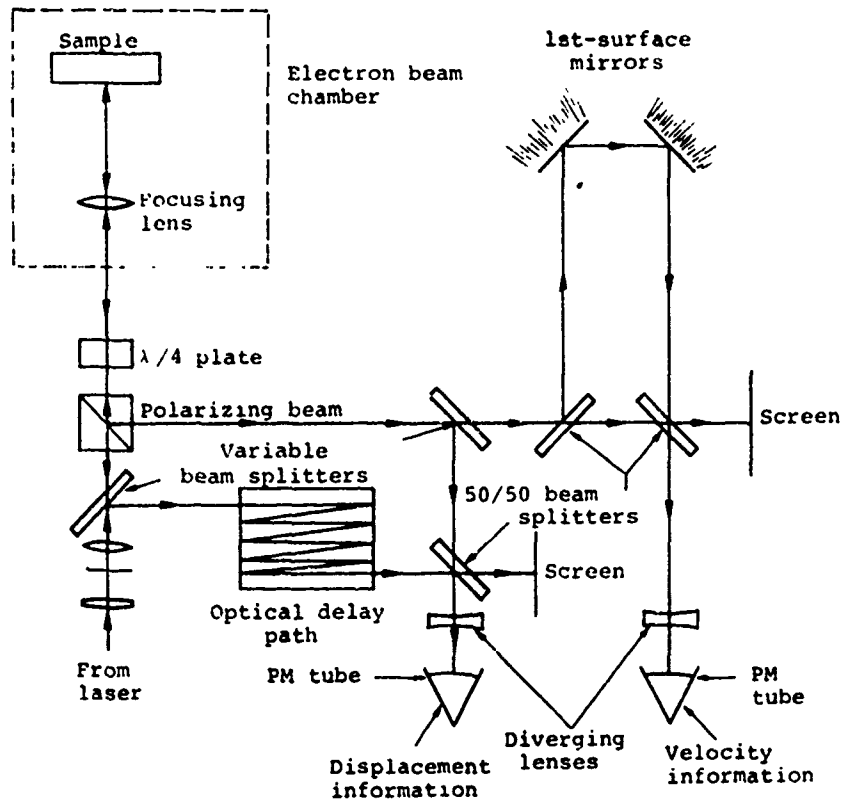
Figure B-1   Tandem mode interferometer system offering simultaneous
              displacement, velocity, and acceleration information.

are monitored by two photomultiplier tubes and data appear as a
series of fringes (360 degrees phase shifts).

In the displacement mode, each fringe indicates a change
in the sample's rear surface position of 2.44×10^{-5} centimeters
along an axis normal to that surface.   In the velocity mode, each
fringe corresponds to a change in surface velocity of 18 m/sec.
This correspondence between fringes and change in velocity in the
latter mode can be altered for any given experiment depending
upon the anticipated rear surface behavior.   By changing the
length of the delay leg the correspondence may be varied from
10 m/sec/fringe to over 1000 m/sec/fringe.

1.1 TECHNICAL DISCUSSION

The laser system in Figure B-1 can be broken down into three basic components--transmission-reception unit, displacement interferometer, and velocity interferometer. The transmission-reception unit (Figure B-2) consists of the laser, a spatial filter, a variable beam splitter, a polarizing beam splitter, and a quarter-wave plate. A 1.2 watt light output is supplied by the laser at a wavelength of 4880 Å. To increase the signal-to-noise ratio the beam is first put through a spatial filter

Expanded view OS spatial
filter (beam diameter exaggerated)
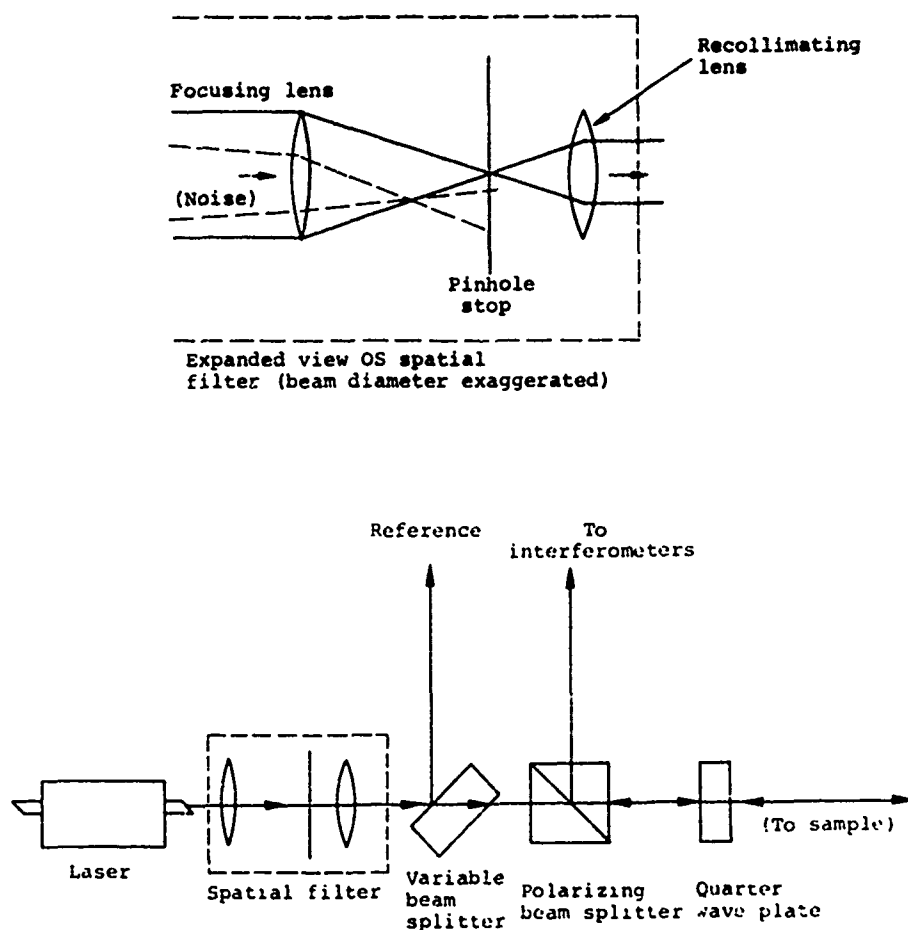
Figure B-2   Transmission-reception unit

121

consisting of two biconvex lenses with a pinhole stop placed
between them (Figure B-2). Since the output of the laser is mono-
chromatic and collimated, the beam is focused to a point by the
first lens. The pinhole stop is placed at the focal point of
the lens where the beam passes through to be recollimated by the
second lens. Noise light generated in the laser tube is not well
collimated, does not become focused, and is blocked by the pinhole
stop. The focal lengths of the two lenses are in the approximate
ratio of 2:1 which affects a similar reduction in beam diameter.
This diameter reduction was deemed necessary due to the long
path lengths over which the beam must be transmitted in the
experimental configuration. An increase in signal-to-noise
ratio of approximately 3:1 was noted due to the spatial filter.
Alignment of the detection system was also simplified since it
was no longer necessary to search for a non-noisy spatial position
of the return beam to interrogate the photomultiplier tube.

From the spatial filter, the beam passes through a variable
beam splitter, a polarizing beam splitter, a quarter wave plate,
and is then transmitted to the sample. The variable beam
splitter diverts a small portion of the light energy to be used
as a reference beam for displacement mode information. The output
of the laser is polarized and, due to the orientation of its
plane of polarization relative to the polarizing beam splitter,
all of the light energy is transmitted at this point.

In the electron beam chamber the laser beam is focussed
to a 10 micron spot on the sample's surface with a long focal
length lens. Since the surface is at the focal point of the
lens, the reflected laser beam returns along its incident path.
This technique simplifies alignment and reduces the sensitivity
to sample tilt. Slight tilt on the part of the sample will result

in only a small lateral displacement of the return beam. On re-
turning to the polarizing beam splitter, the beam is reflected
instead of being transmitted since its plane of polarization has
been rotated 90 degrees by a double transit through the quarter
wave plate. Thus, the return beam is prevented from re-entering
the laser cavity to cause instability. From here the return beam
is passed through the two interferometers and its information
content is converted to the outputs of the two photomultiplier
tubes.

Displacement information is obtained by diverting part of
the energy of the return beam with a second variable beam splitter
and combining it with the reference beam as shown in Figure B-1.
The path length of the reference beam is adjusted with a double
mirror bank to be approximately equal to twice the distance from
the laser to the sample under inspection; this ensures that the
path length remains within the coherence length of the system.
Since the laser has a coherence length of 10 meters, this require-
ment is not singularly critical. From the displacement interfero-
meter, the beam passes through a diverging lens and into the
photomultiplier tube. The diverging lens allows only one fringe
to be interrogated, eliminating spatial integration effects.
Also, it allows the input light intensity to be adjusted for
maximum signal and signal-to-noise ratio. A typical displacement
mode trace along with the velocity-time profile is shown in
Figure B-3.

The portion of the return beam not used in the displacement
mode is interrogated by the velocity interferometer. Here the
Doppler shift is detected by comparing the phase of the light at
one instant of time with phase at an earlier instant. The rela-
tive phase is then directly proportional to the rear surface

velocity. A velocity interferometer (Figure B-4) is used to affect this phase comparison. The return beam is split at the first beam splitter and half of the light is directed around a delay leg to be recombined with the direct beam at the second splitter. A double concave lens diverges the recombined beam that is then detected by the photomultiplier tube. As the rear surface velocity changes, so does the relative phase of the re- combined beam. For a shift of one full fringe, a minimum change in surface velocity of 10 m/sec is required. This relationship may be altered where very high rear surface velocities and accelerations are anticipated by shortening the length of the delay leg. The relationship between the number of fringes observed and the rear surface velocity is given by the following formula:

$$u = \frac{\lambda C}{4D} N$$

where u is the free-surface velocity, λ is the wavelength of the laser light, C is the speed of light, D is the length of the delay leg, and N is the number of fringes observed up to that point in time. Figure B-5 shows a typical example of the photo- multiplier tube output and associated data reduction for a test on reference Sparesyl.
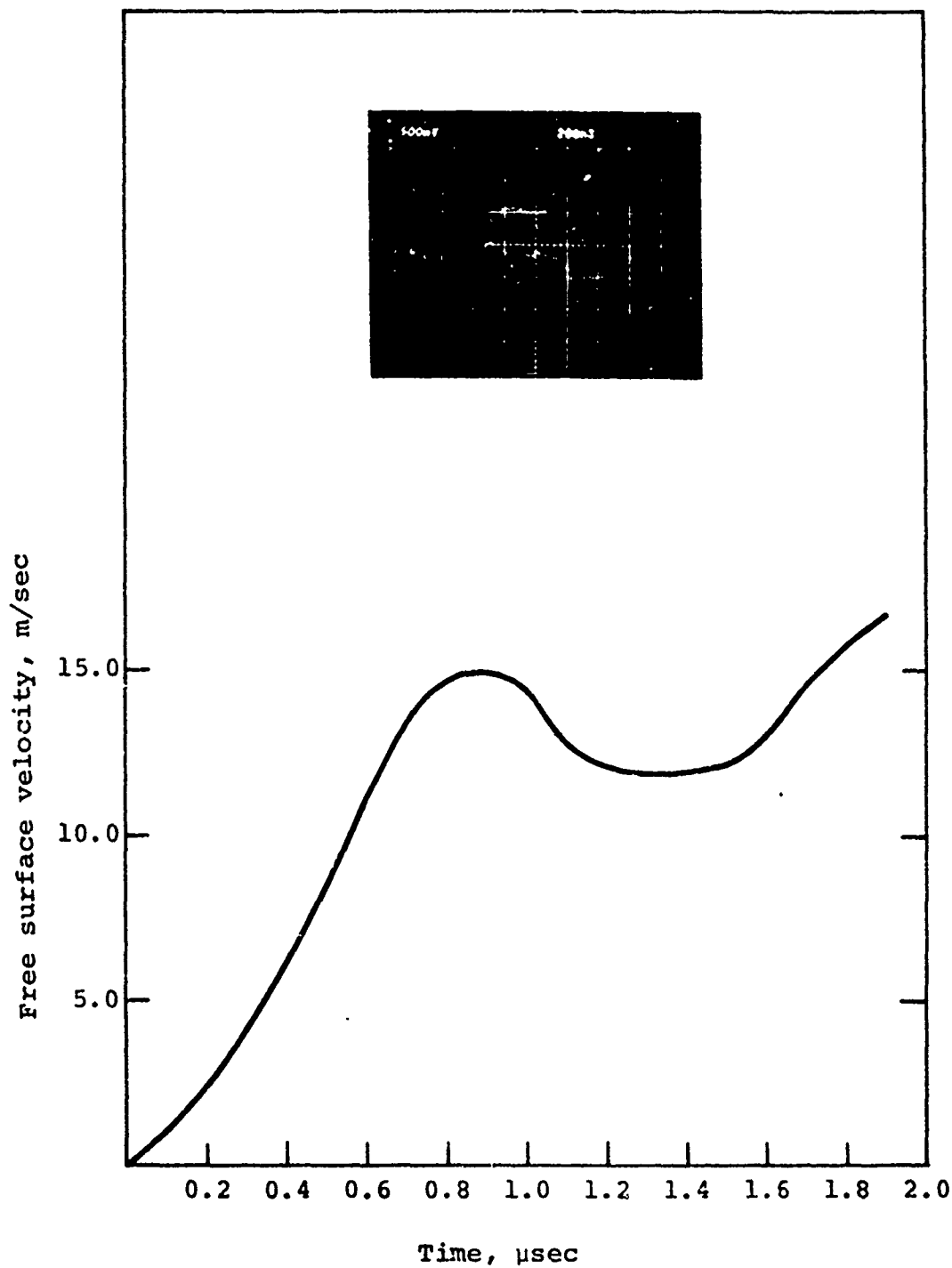
Figure B-3   Typical displacement-mode shot on reference
            Sparesyl sample.
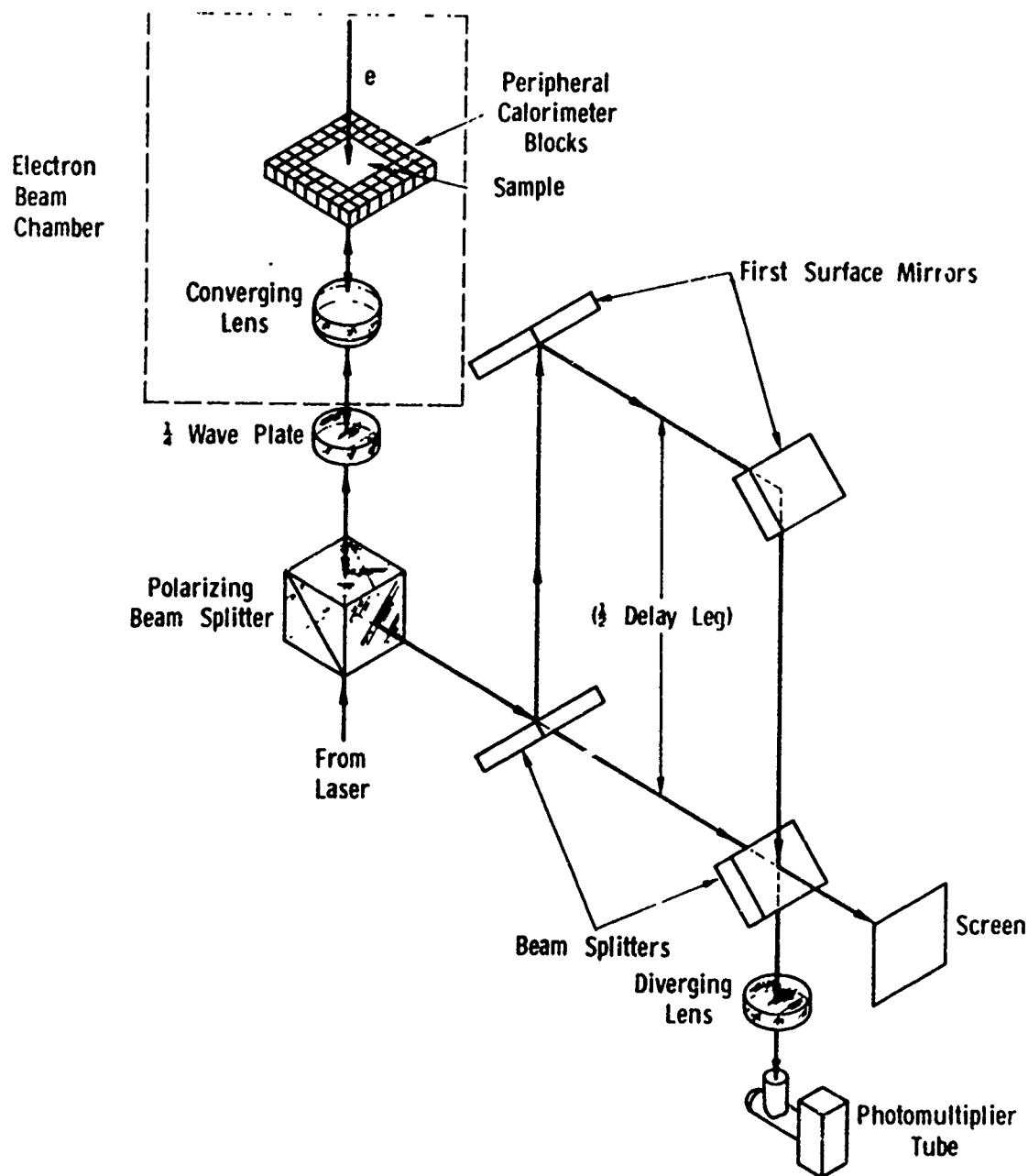
Figure B-4   Velocity interferometer.

SECTION B-2
OPTICAL DETECTORS

Photomultiplier tubes have been used as a light sensor to detect destructive and constructive fringes of the interfering laser beams and to convert these changes in light intensity to electrical signals. Three RCA PM tubes have been tested in the course of developing the Physics International laser interferometer into an effective diagnostic tool for the study of dynamic behavior in materials. They are models 1P28, 6810A, and C-70045C. Due to its high gain, tube model 6810A was found to be overly sensitive and hard to stabilize. For this reason, the other two tubes were chiefly used. The 1P28A model was used for bench testing and experiments requiring frequency response under 100 MHz; model C-70045C was used for light signals of higher than 100 MHz frequency. While Model 1P28 was used regularly in both CW and gated-modes, the C-70045C tube was mainly incorporated in a pulsed scheme with optional CW operation. A brief description of the system employing the fast RCA photomultiplier tube is given below.

B.2.1 PM TUBE AND ELECTRICAL CIRCUIT

The C-70045C tube is an experimental PM tube design from RCA. It is a side-on device having an S-20 response (Figure B-6).
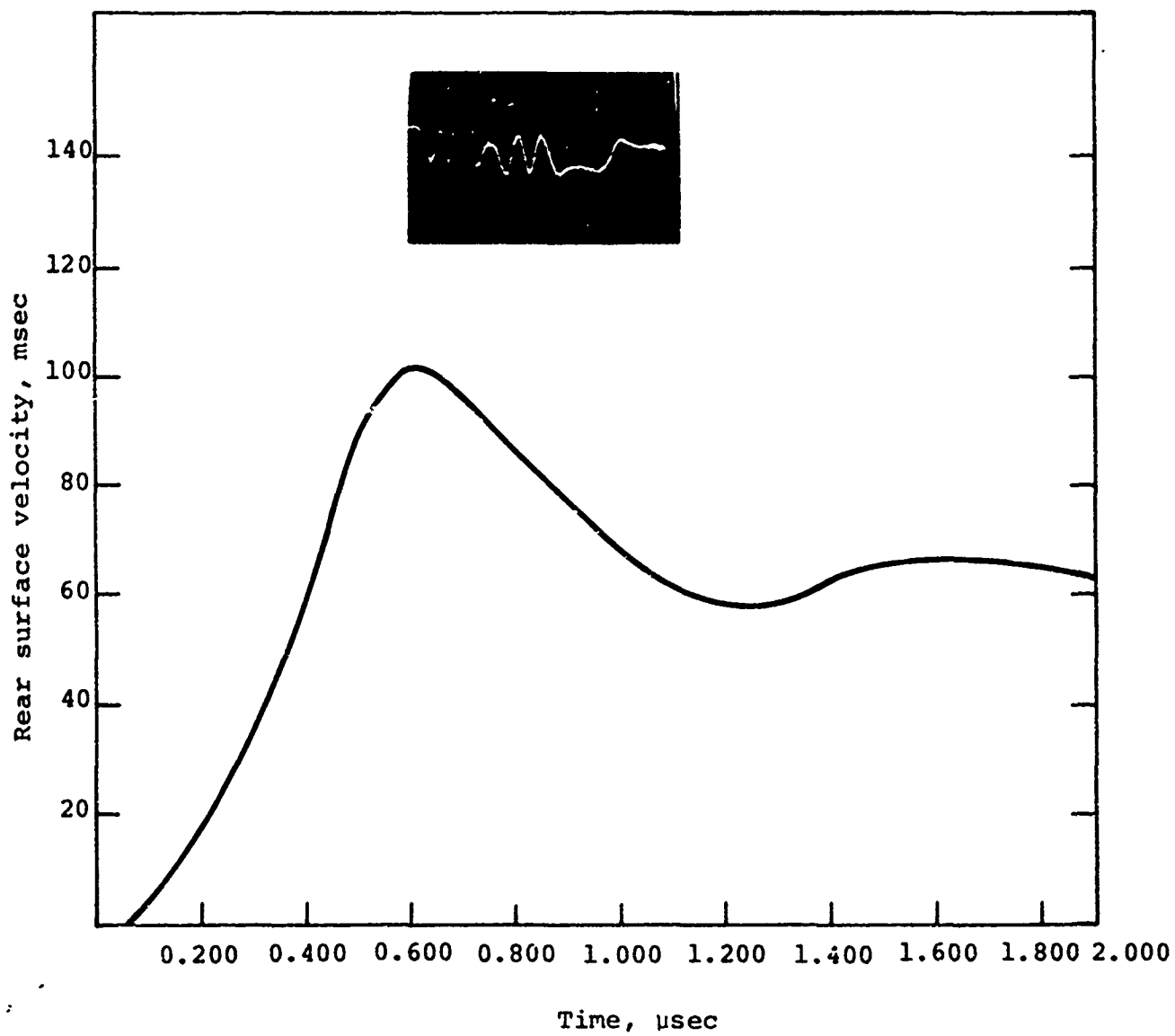
Figure B-5   Typical velocity-mode data on reference
             Sparesyl.
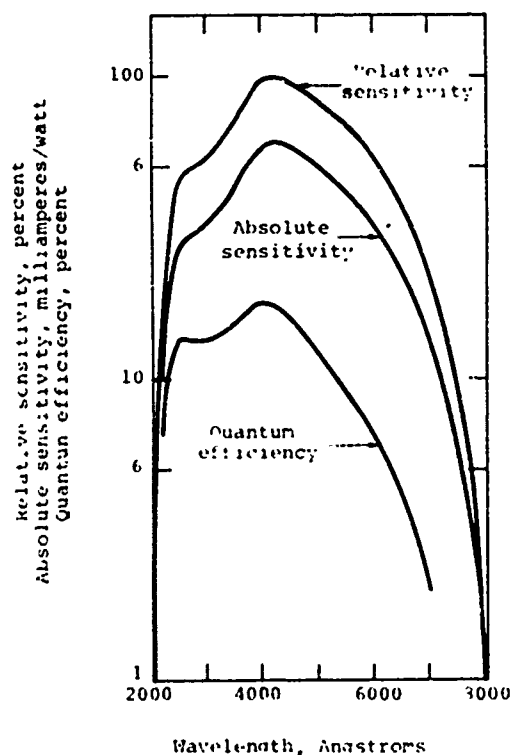
Figure B-6   Typical spectral response characteristics
of RCA-C70045 photomultiplier tube.

Fourteen dynodes alternate with 14 accelerating electrodes and
a 50-ohm coaxial output. The factory objective sheet gives a
risetime of 0.5 nsec and a gain of 10^6. Displaying the anode
response of an occulted tube to cosmic ray pulses with a
Tektronix 7074 oscilloscope (7A16 plug-in) has reflected the rise-
time limitation of the scope (T_r = 2.4 nsec) rather than that
of the tube (Figure B-7). The frequency response of the C-70045C
in laser interferometry appears to be limited by the pulse fall-
time which was found to be 1.5 to 2.0 nsec.

129
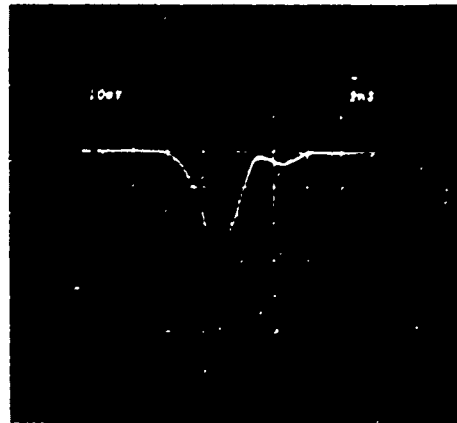
Note: The risetime is typical of the oscilloscope used
(Tektronix 7704).

Figure B-7   Anode output pulse of an occulted RCA C-70045C
PM tube (V_{C-A} = 5000 V)

In developing electrical circuits for the PM tube, the
findings of similar experimental programs* have been studied
and adapted where they were found applicable. Consequently,
several modifications to the manufacturer's suggested circuit
have been made to avoid overload or "run-away" of the tube at
dc light levels expected to be attained within the interferometer.
The most important modification was designed of a gating circuit
to operate the PM tube under its optimum conditions, that is,
to detect low-level light pulses of short duration. The circuit
turns on the tube by applying a voltage pulse between the photo-
cathode and dynode number 3, both floating normally at the same
potential in a turned-off condition. The circuit is a simple
SCR design (Figure B-8) which discharges a 0.05 μF capacitor,
thereby adding 1200 to 1600 volts for a period of 25 μsec to the
aforementioned divider section.

---

*
Sandia Corporation Report SC-DR-66-2689.

R9120

130

Minibox
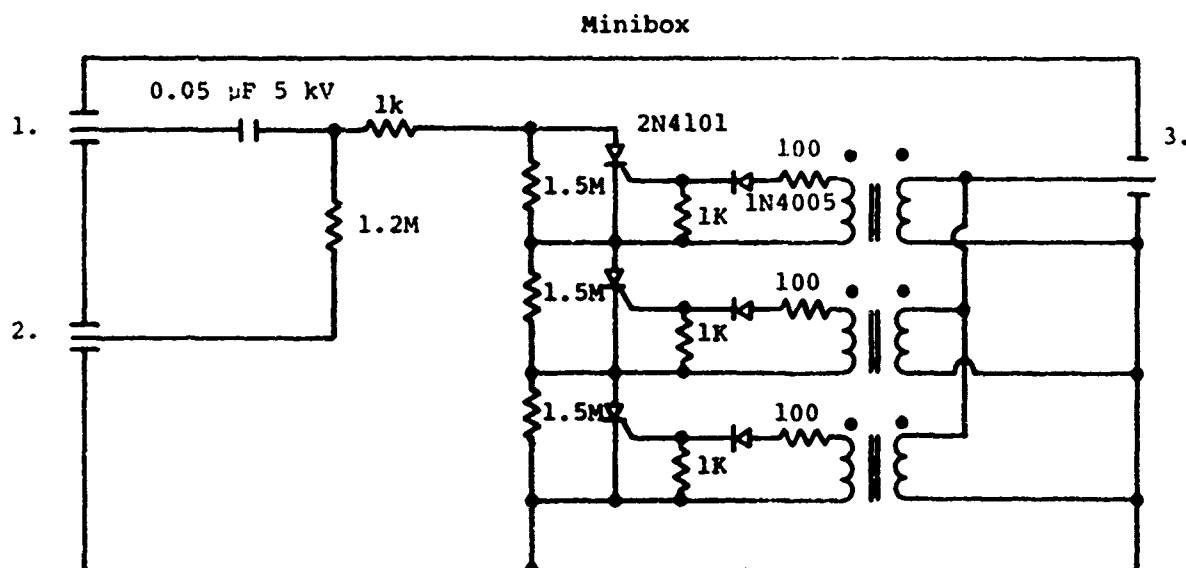
1. Gate output: ~ - U/5 V_2, for PMT cathode
2. + V_2: typically 2000 volts for RCA C-70045C
3. Trigger pulse: gate pulse from Tektronix 555

Figure B-8   Gating circuit used with PM tubes on the
             laser interferometer.

The gating and voltage divider-circuits are designed to
operate each of the 32 elements at the factory recommended voltage.
The voltage divider circuit (Figure B-9) is a 4 mA resistor
divider with interdynode capacitors mounted on the socket. The
large capacitors are used to maintain constant voltage and gain
per stage when the tube is gated-on in the presence of high light
levels while the smaller capacitors are necessary to stabilize
the gain during high frequency light transients.
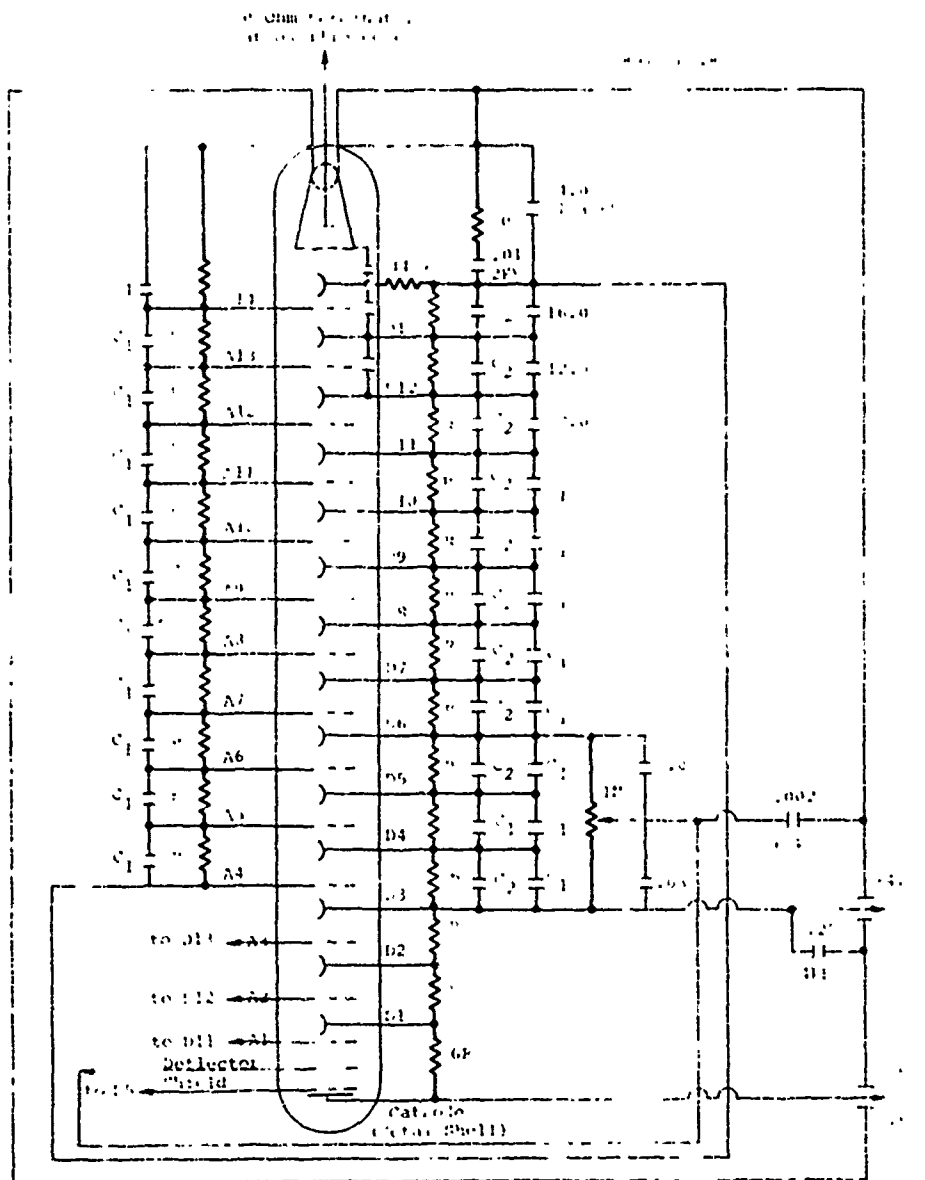
Figure B-9 Voltage divider for the RCA C-70045C PM tube.

The maximum signal currents obtained while gating without overloading the tube were 70 to 80 mA through the 50-ohm load resistor. It was decided that biasing the anode of the PM tube (thus further increasing the gain at the expense of possible decreased frequency response) would not be used.

B.2.1 EXPERIMENTAL SETUP

A typical arrangement for displaying interferometer detector signals is shown in Figure B-10. The photomultiplier tube with a cylindrical light channel incorporating a 1-inch-diameter aperture is facing the laser beam and is turned on by the gating circuit. Via a 555 oscilloscope, the Pulserad control panel triggers the tube 7 μsec in advance of the electron beam pulse.
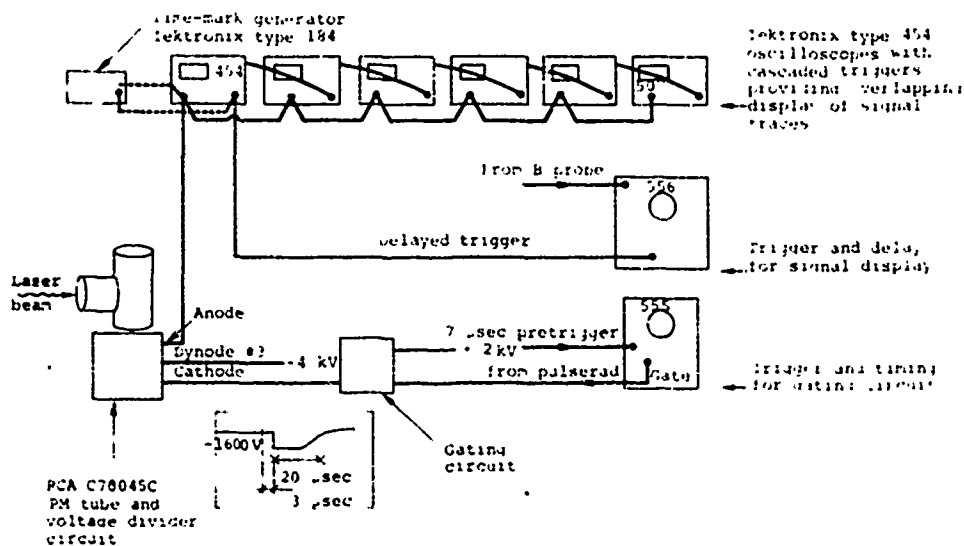
Figure B-10   Block diagram of a typical experimental setup.

The photomultiplier anode circuit was completed through an external 50-ohm load resistor; due to the signal current the voltage drop across the load was displayed by several 454 type Tektronix oscilloscopes. In order to show the temporal history of the signal, the sweeps of the scopes were cascaded by using the delayed gate output of a scope to trigger the succeeding one. The first oscilloscope in the chain was triggered typically by the B probe signal of the Pulserad after selection of sweep speeds. A type 184 time mark generator was used to synchronize the participating oscilloscopes. Normally, a two division overlap was maintained between two displays to utilize only the most linear, central, 8-centimeter section of each oscillograph.

During the pre-shot alignment of the interferometer, the photomultiplier tube was repetitively gated (60 Hz) to continuously view the laser beam modulated by an oscillating mirror of the system. For this quasi CW test, 4,000 volts were maintained between dynode number 3 and the anode, with 1,200 volts switched onto the divider section, thus turning on the photocathode. Light intensity was adjusted to slightly overload the PM tube with maximum ac to dc signal ratio. Finally, the detector system was readied for the data shot by switching to the single gate scheme with the expected voltage pulse between dynode number 3 and the photocathode increased from 1,200 to 1,600 volts. Typical signal levels of 2 to 3 volts were obtained with signal-to-noise ratios in excess of 20:1 using this system.

SECTION B-3

RESULTS AND CONCLUSIONS

The advantages of the laser interferometer as a diagnostics tool are several. An optical probe applies no loading to the surface under test for free rear surface measurements. In contrast to quartz gauges, there is no averaging of the stress over an area because of the small spot size used (approximately 10 μ diameter). There is also no intrinsic readtime limitation as with quartz gauges; (time windows of up to 25 μsec have been used). Alignment of the system has been simplified and turn-around time of as low as 20 minutes between shots has been achieved. Presently the laser interferometer is being used in conjunction with a ballistic pendulum for making simultaneous measurements of impulse and stress.

APPENDIX C

MANGANIN PIEZORESISTIVE GAUGE MEASUREMENTS

136

Etched manganin-foil gauges (3/4-mil thickness) and
manganin wire gauges have been used in the past at PI. The foil
gauges (1.5-ohm impedance) are proposed for the tests since they
offer the advantage of being sandwiched between two pieces of
test material and are readily available in large quantity. Use
of the wire gauges (about 7-ohm impedance) potted in C-7 epoxy
necessitates a correction for differences in shock impedance
between the epoxy and the sample material. If the shock imped-
ances of any test materials are well known, this correction is,
of course, not a problem. Signal-to-noise ratios are suf-
ficiently large to enable recording of a 1-kbar stress pulse
in the foil gauges (shown in the following section). In prac-
tice we have seen very little difference in signal-to-noise
ratio between the foil and wire gauges.

C.1   MANGANIN GAUGE PRESSURE RECORDING SYSTEM--EXPERIMENTAL SETUP

Figure C-1 is a schematic diagram of the manganin recording
system, similar to that used by Stanford Research Institute.
The power supply, which provides a nearly constant current of
1 to 5 amps to the gauge, is triggered approximately 70 μsec
prior to beam firing by the delay trigger generator. The "turn
on" voltage, V, produced across the active gauge resistance,
R, is monitored on one trace (channel A) of a Tektronix 555
oscilloscope (Figure C-2). Arrival of a plane shock wave at
the active gauge element causes a change in its resistance,
ΔR, which results in a change in the voltage, ΔV, monitored on
channel A. The relative voltage change, $\Delta V/V$, is typically < 1
percent under low-stress conditions and precludes accurate
measurement of ΔV on the channel A oscilloscope trace. Record-
ing of ΔV is accomplished by subtraction of the turn-on voltage

Preceding page blank

137
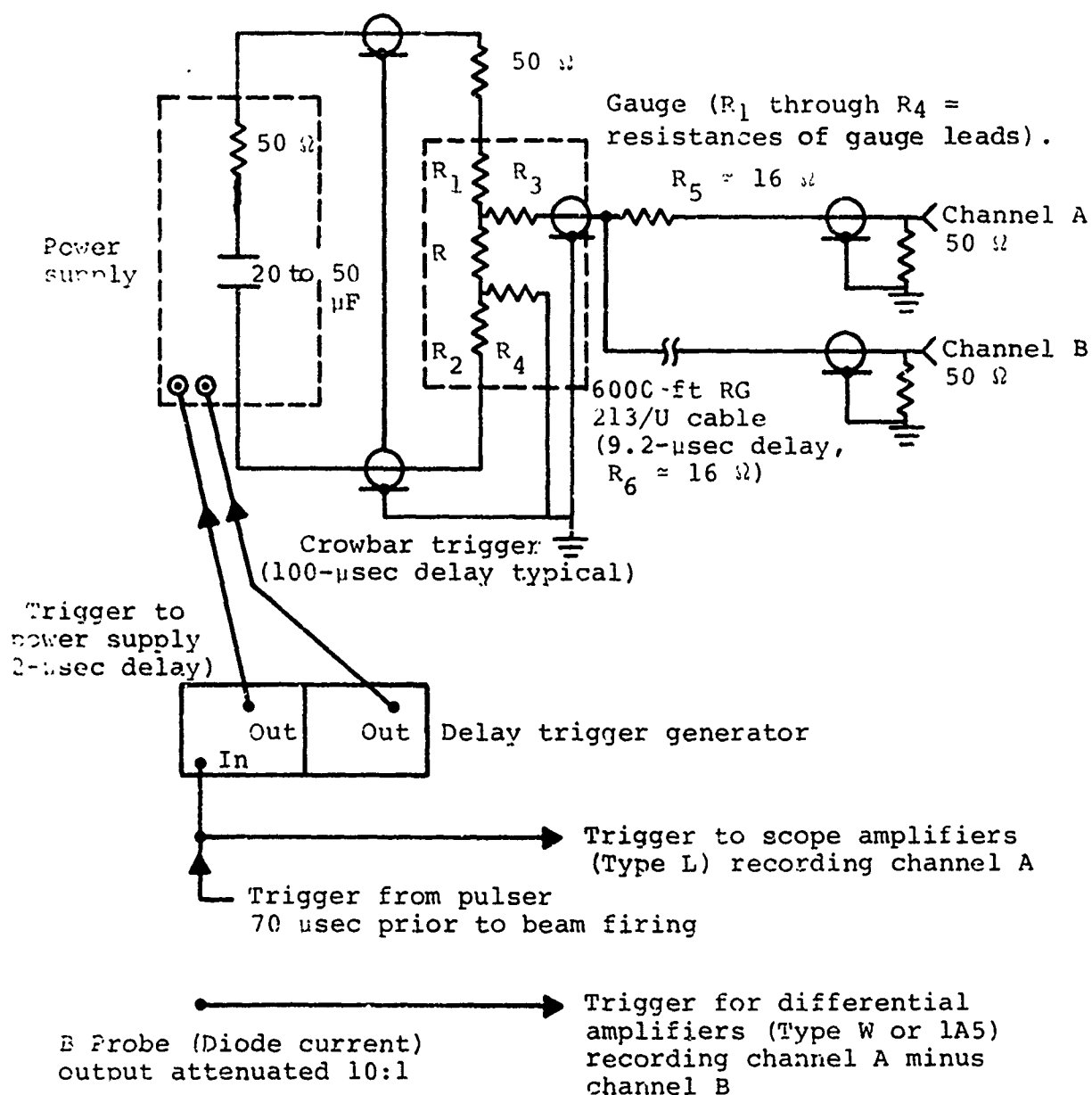
Figure C-1 Schematic of manganin measuring system.
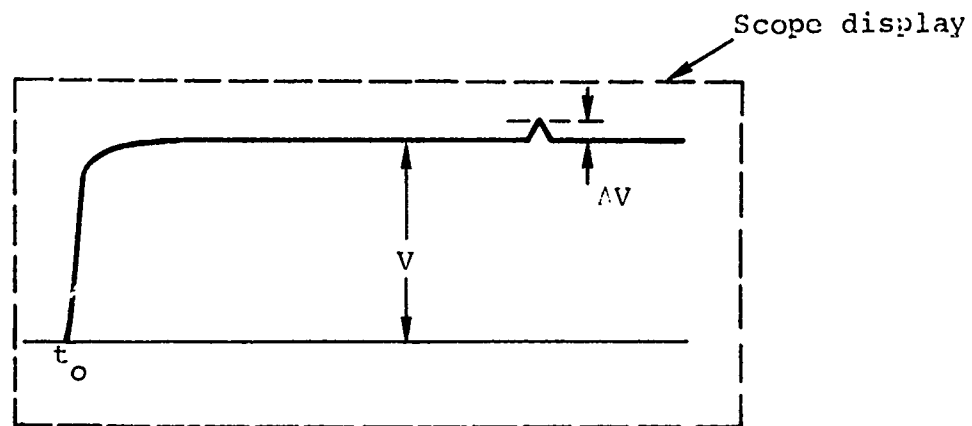
Figure C-2   Channel A, voltage-time profile.
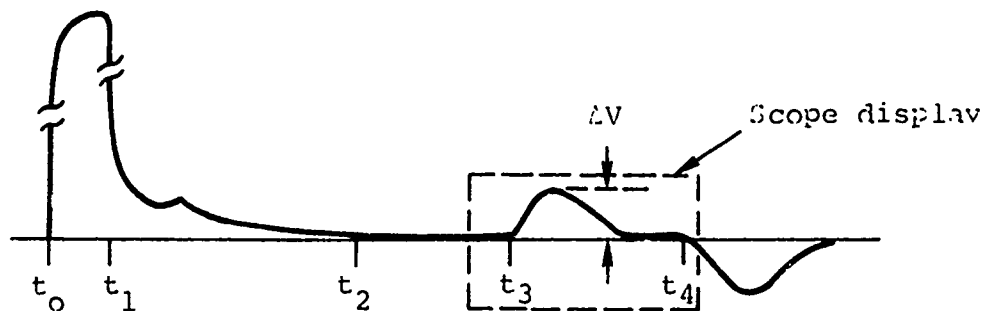
Figure C-3   Channel A minus Channel B, voltage-time profile.

(V) from the gauge output (V + ΔV) using a differential amplifier (a Type W plug-in unit) by splitting the gauge output into two channels, with channel A going directly to the scope. The difference A-B is monitored on the other trace of the 555 oscilloscope, and this trace is triggered at the time of beam firing. Figure C-3 shows the time history of this A-B signal and indicates the portion displayed on the oscilloscope. The term t_o is the time at which the power supply is turned on. The term t_1 corresponds to the time for the initial signal to travel through the delay line (t_1 = 9.2 μsec for 6000 ft of RG 213/U cable). The term t_2 is the time it takes for the system to stabilize (t_2 = 60 μsec for 6000 ft of cable); t_3 is the time of the signal arrival of channel A at the scope. This recording system reads ΔV(t) until time t_4 = t_3 + 9.2 μsec for a 6000 ft delay cable. After t_4 the signal becomes s(t) = ΔV(t) - ΔV (t = 9.2 μsec). Note that the dc resistances of channels A and B must be equal (a variable resistor was used, R_5, to balance out the dc resistance of the delay cable). With the present system, V is measured on one trace and ΔV on another. A dc circuit analysis gives the relationship between ΔV/V and ΔR/R (Figure C-4) from which the stress can be calculated.

In order to operate the manganin gauge in the electron-beam environment, it must be electrically shielded. This was done by placing the gauge, target, and cables inside a 4-inch-id variable-length copper cylinder with 1/16-inch-thick walls that bolts to the aluminum drift-chamber door (Figure C-5). The front face is a 1/2-inch-thick aluminum plate with an orifice just large enough to admit the end of the guide cone. The target is held against the orifice by a brace. In the case of nonmetallic targets it is necessary to place a grounded piece of 0.001-inch-thick aluminum foil between the target and the gauge to shield the gauge element from noise.

140
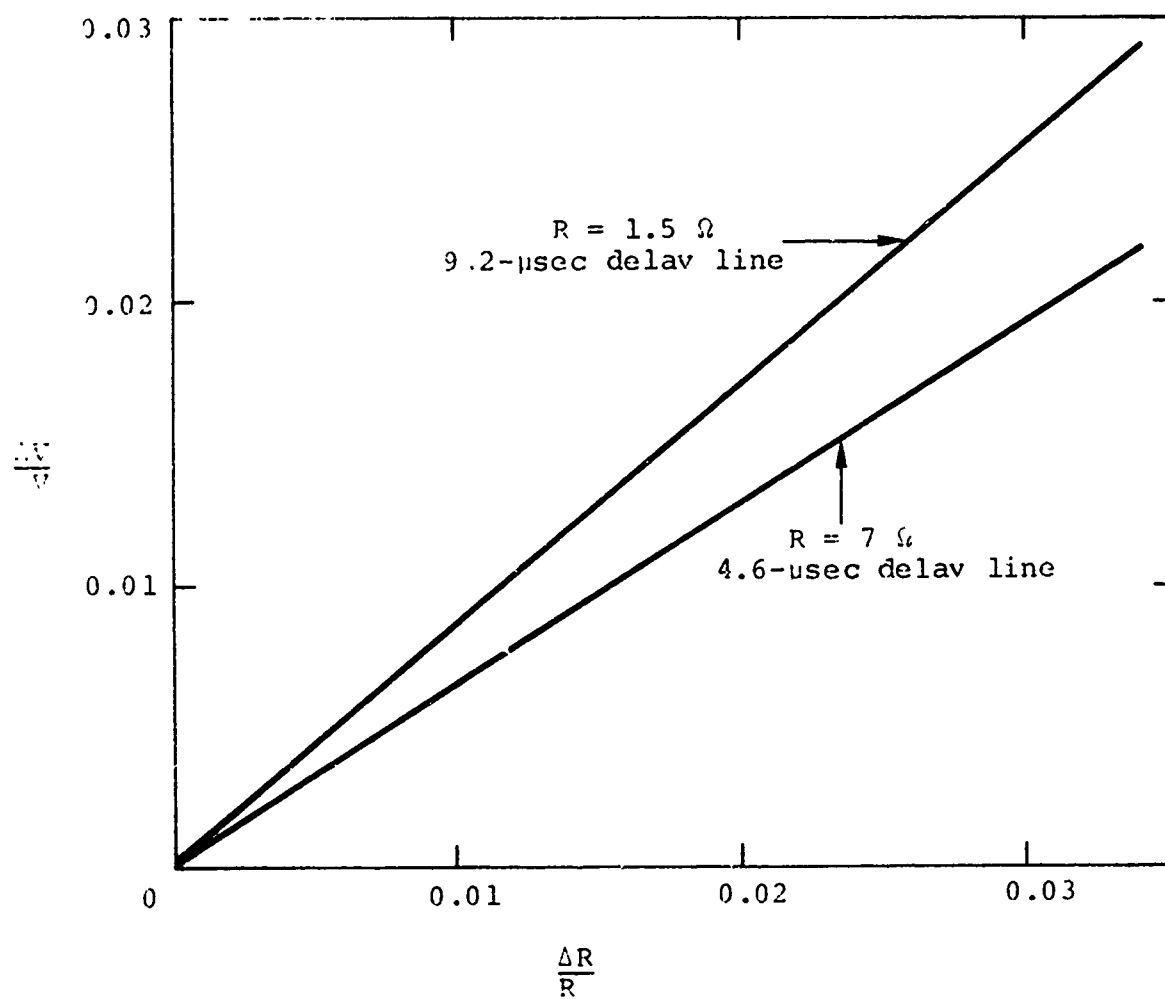
Figure C-4 $\Delta V/V$ at the scope versus $\Delta R/R$ at the gauge.

141
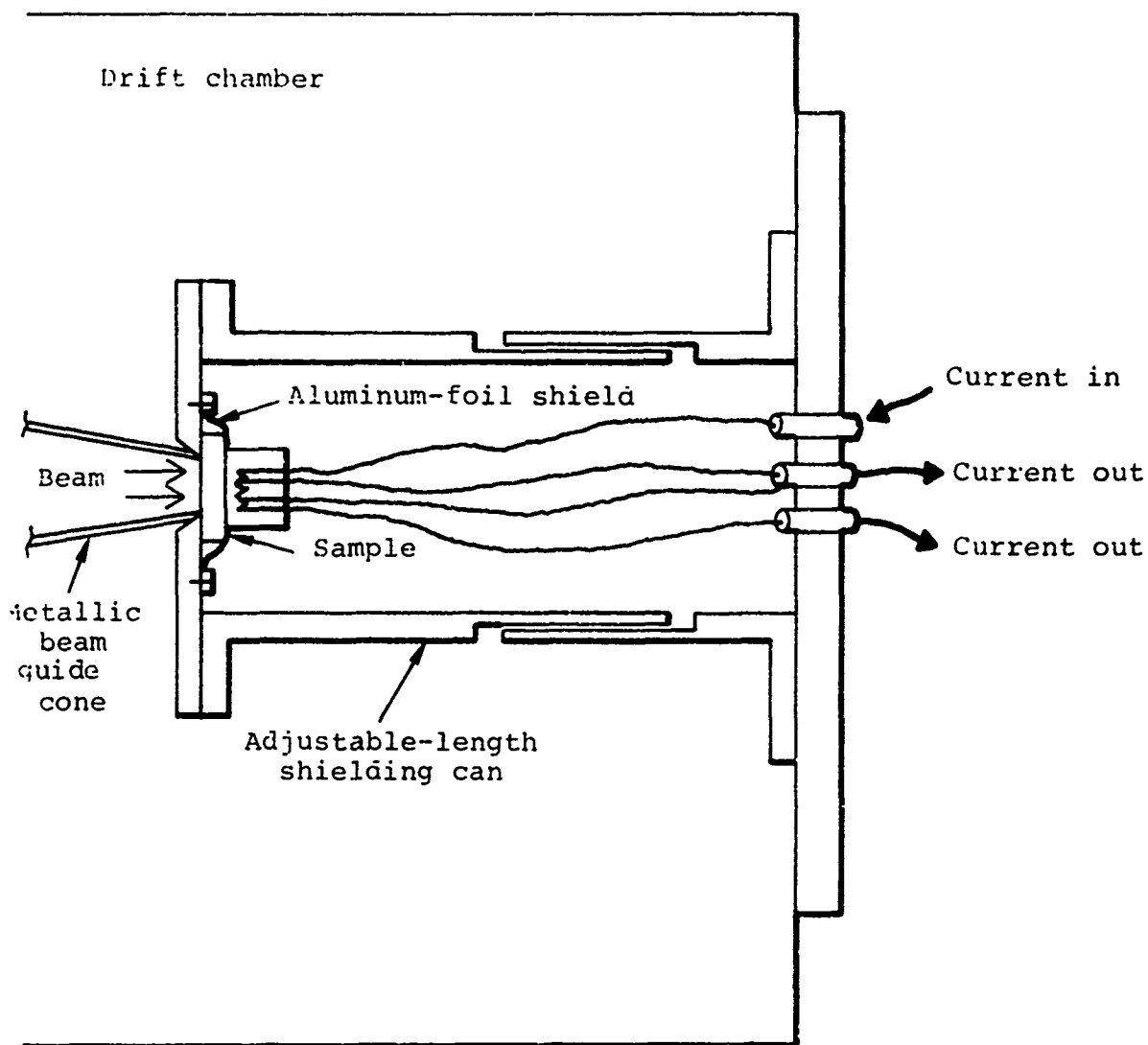
Figure C-5 Detail of shielding configurations.

142

2. Results

Results of manganin tests in a two-dimensional weave
material are presented here to exhibit signal-to-noise ratio
versus time, recording time, and gauge sensitivity under actual
operating conditions. Some 1.5-ohm foil gauges were used with a
1-mil aluminum shielding foil placed between the front sample
section and the gauge element. One-half-mil Mylar was used as
electrical insulation on each side of the gauge. The gauge was
sandwiched between a 1/4-inch piece of the test material (which
was irradiated with 250 keV electrons at about 45 cal/cm^2 uniform
over 2.5 cm^2) and a 1/2-inch-thick piece of test material. The
shielding canister was also used.

Figure C-6 shows the recorded gauge output. Noise level is
seen to decay to about 10 mV in 0.5 µsec, and drops to < 5 mV
after 1.5 µsec. Noise level remains at this level until 9 µsec
at which time noise arrives through to delay line, giving an
effective reading time of about 8 nsec.

The stress pulses shown in Figure C-6 are from the same
shot. Figure C-6a shows the shock pulse, on scale, followed by
a low-stress, long-duration pulse which is more clearly visible
in Figure C-6b (higher scope sensitivity scale). Peak pressure
of the shock pulse is approximately 8 kbar, while the following
pulse peaks at approximately 2 kbar. Signal-to-noise ratios
for the whole stress record are seen to be about 10 to 1.

Integration of pressure versus time gives an impulse of
5.0 ± 1.0 ktap (the uncertainty arises from a possible baseline
drift at late times). Independent measurement of total impulse

under conditions similar to the shot illustrated in Figure C-6 show an impulse of 4.2 ± 0.3 ktap. The conclusion of this work was that impulse was delivered to the material by the initial shock pulse (short duration) and by a long-duration pulse caused by front-surface blowoff.

Other examples of manganin results are shown in Figures C-7 and C-8. These data were collected, as part of a program for AVCO, with manganin wire gauges. The spike visible in Figure C-7 at about 9 μsec is the arrival of noise through the delay cable. As explained in the preceding section the pressure time profile can be reconstructed from the gauge output for times longer than 9 μsec. In this particular material no double-pulse structure was evident.

3. Simultaneous Impulse and Stress-Time Measurements

The manganin-gauge technique described above was combined with the ballistic pendulum measurement of impulse. The gauge was positioned in the pendulum bob. The gauge power and signal leads were run out of the bob, through the pendulum rod and axle to a terminal board on the axle (Figure C-9). Damping of the pendulum motion was avoided by continuing the connections from there by way of loosely draped, thin wires to a stationary terminal board on the pendulum support. RG 58 cables were used to complete the circuit.

The gauge leads were shielded from the RF environment in the drift chamber. The pendulum bob, rod and axle provided shielding up to the decoupler (Figure C-10). The decoupler and the cables up to the beam chamber wall were shielded by a flexible, copper pipe (see foreground of Figure C-10).

144
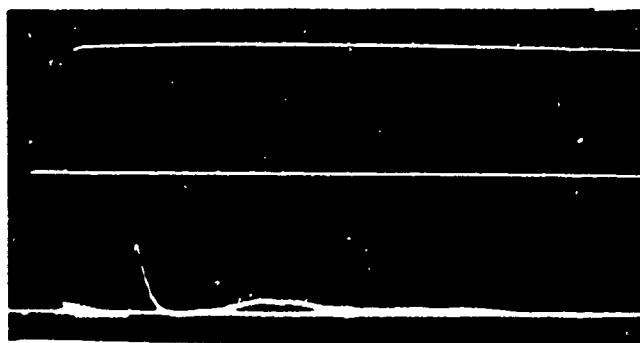
2 V/cm
10 µsec/cm
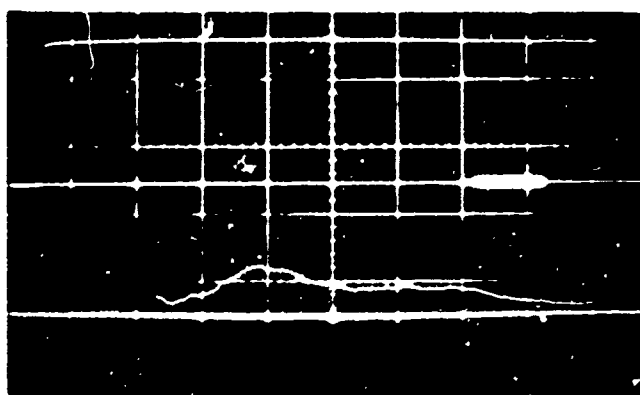
50 MV/cm
1 µsec/cm

2 V/cm
10 µsec/cm

20 MV/cm
1 µsec/cm

Figure C-6   Manganin gauge records for two-dimensional-weave
material.

2 V/cm

10 μsec/cm

20 mV/cm

1 μsec/cm

5 V/cm

10 μsec/cm

50 mV/cm

2 μsec/cm
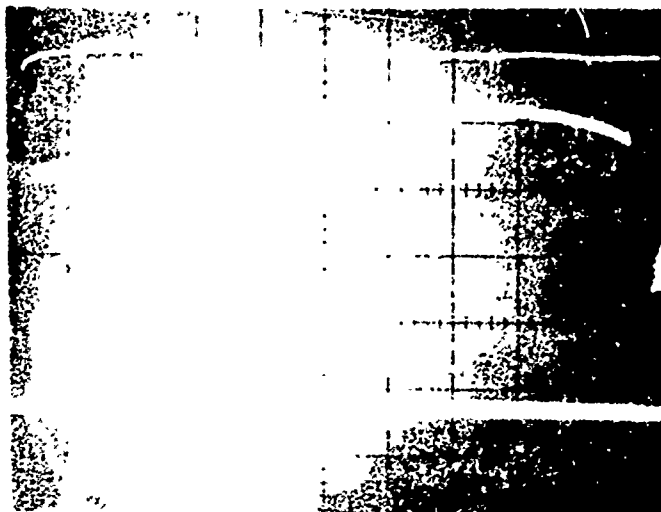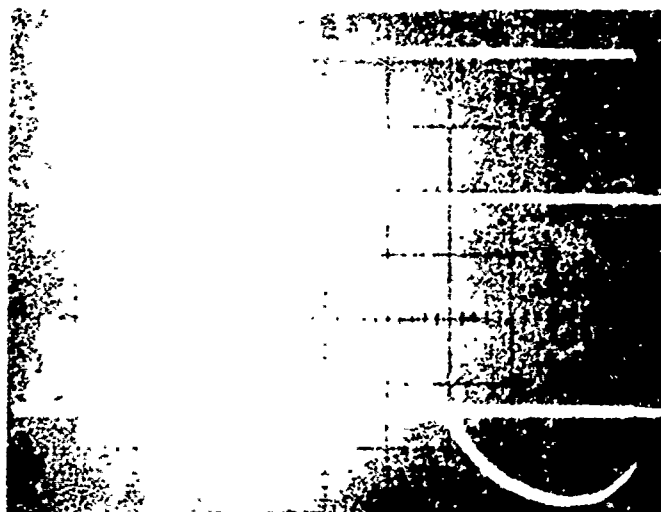
Ceramic gage data (Shot No. 12871).

0.5 V/cm

2 μsec/cm

5 V/cm

10 μsec/cm

0.1 V/cm

1 μsec/cm
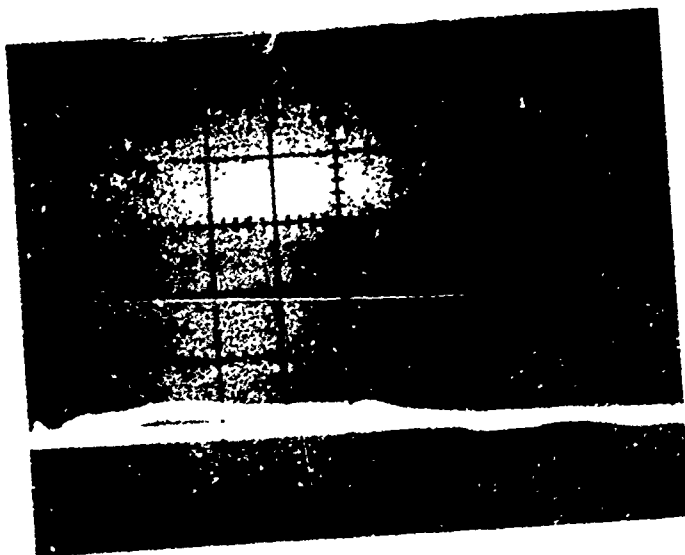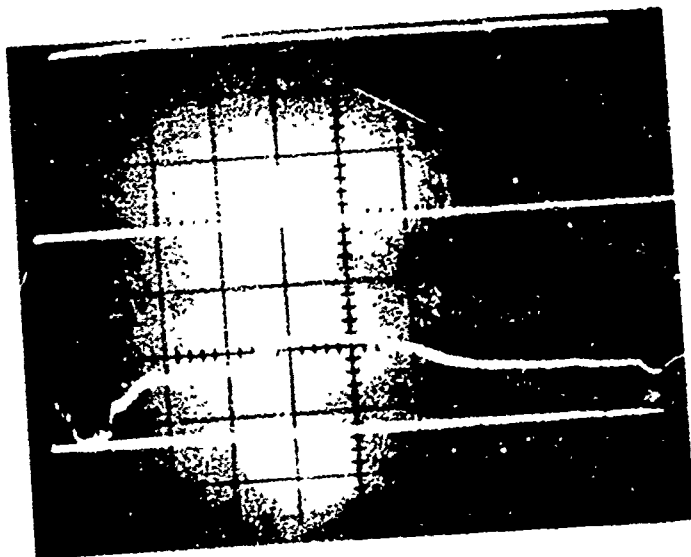
Figure C-8   Manganin gauge data (Shot No. 12872).

147

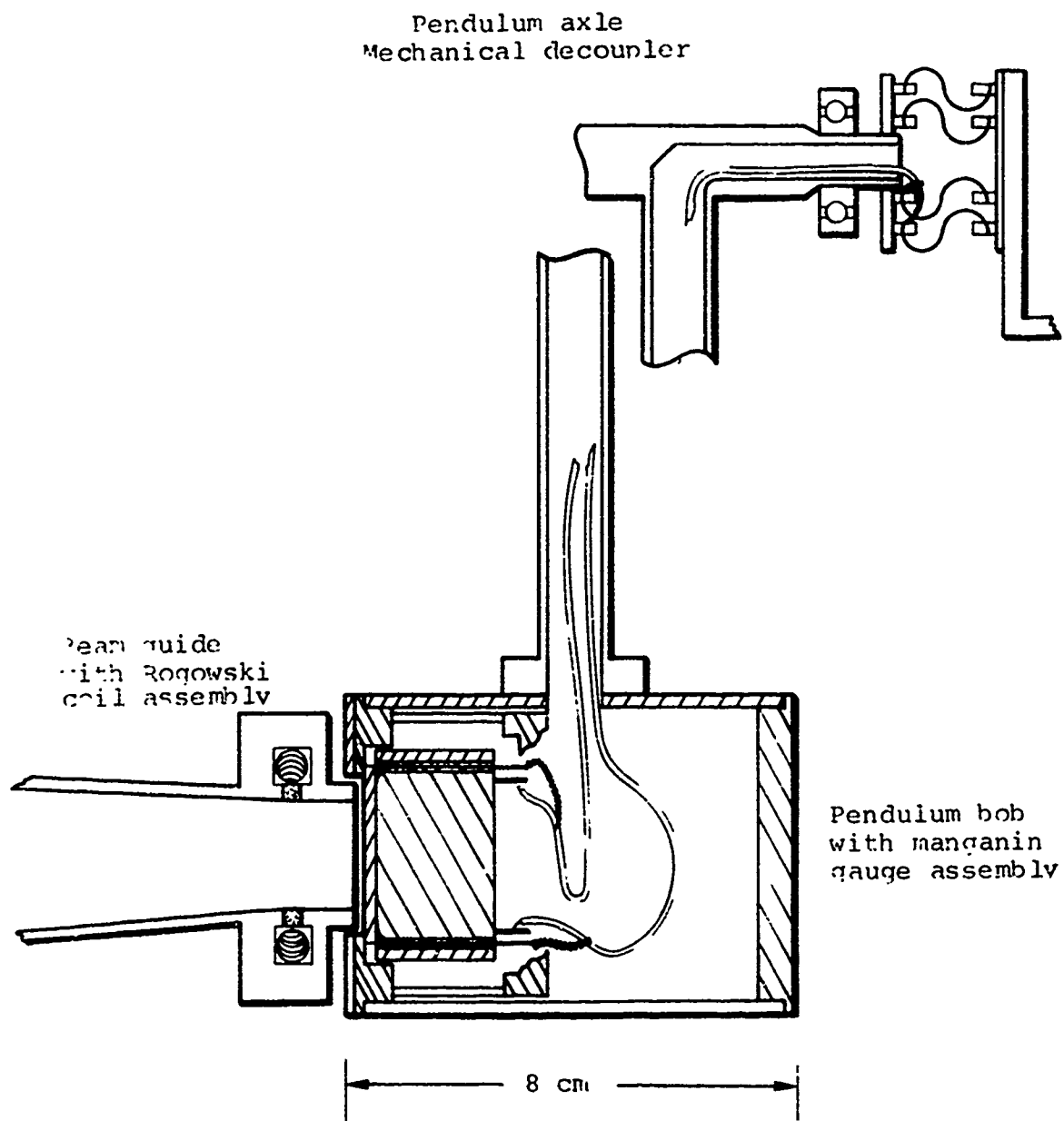Pendulum axle
Mechanical decoupler

Beam guide
with Rogowski
coil assembly

Pendulum bob
with manganin
gauge assembly

|← 8 cm →|

Figure C-9   Manganin gauge assembly in the bob of a ballistic
            pendulum.

Figure C-10   Experimental setup of simultaneous impulse stress-
time measurement.

149

APPENDIX D
FRONT SURFACE MASS REMOVAL

150

When the aluminum samples are examined after irradiation by
the pulsed electron beam, the characteristic appearance of the
craters is observed to change rather dramatically as a function
of the mean electron energy and beam intensity. For low (200 to
300 keV) electron energy beams, the craters at low fluence are
clean and the floor exhibits a granular texture similar in appear-
ance to rear surface spalls, but somewhat smoother (Figure D-1
(a)). As the fluence is increased, the crater depth increases
and droplets of solidified melt are observed on the crater floor
(Figure D-1 (b)). As the fluence is increased further, more
and more solidified melt is found in the crater, until, at the
highest fluence, the crater is obscured by the solidified melt
which exhibits evidence of extensive radial flow (Figure D-1
(c)). Using higher energy beams (> 600 keV) the craters are
deep and clean, even at high fluences.

The observed variation in crater appearance and the extent
of mass removal can be qualitatively explained by considering
the basic physical processes that produce front-surface mass
loss. To simplify the following discussion, effects due to the
source duration and nonlinear material properties will not be
considered. Their inclusion is straightforward and does not
alter the conclusions presented.

(a)
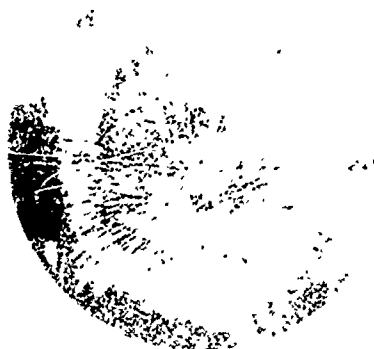
(b)

(c)

Figure D-1   Aluminum samples: (a) low, (b) medium, (c) high
fluence at mean electron energies of 200 to 300 keV.

Consider an energy deposition profile as shown in Figure D-2. For instantaneous deposition, the initial pressure (determined by the Gruneisen coefficient) will have a similar form, while the initial particle velocity is zero everywhere. The heated material will expand both at the free surface and against cooler material, sending a compressive stress pulse into the cold region. The subsequent deceleration of the material expanding toward the free surface produces a tensile pulse, if no spall occurs.

The details of the stress-wave interactions that produce the tensile state can be illustrated by considering the initial pressure to be the superposition of two compressive stress pulses propagating in opposite directions, each with the same width and half the amplitude of the initial pressure distribution. The tensile pulse is thus the result of the reflection of the left-going compressive pulse from the free surface. The reflected pulse can be treated as a right-going virtual tensile pulse. These waves are shown schematically in Figure D-3.

The tension develops as the virtual pulse propagates into the material (and becomes real). Since the tensile pulse follows behind the right-going compressive pulse, it is superimposed only with the left-going compressive pulse (which passes out of the material and becomes virtual).

First, examine the case where the spall strength of the material is larger than the peak tension. The development of the stress pulse in this case is illustrated sequentially in Figure D-4. There it may be seen that the peak tension at each instant occurs at the location of the leading edge of the tensile pulse and with a magnitude determined by the sum of the maximum tensile pulse amplitude and the magnitude of the left-going
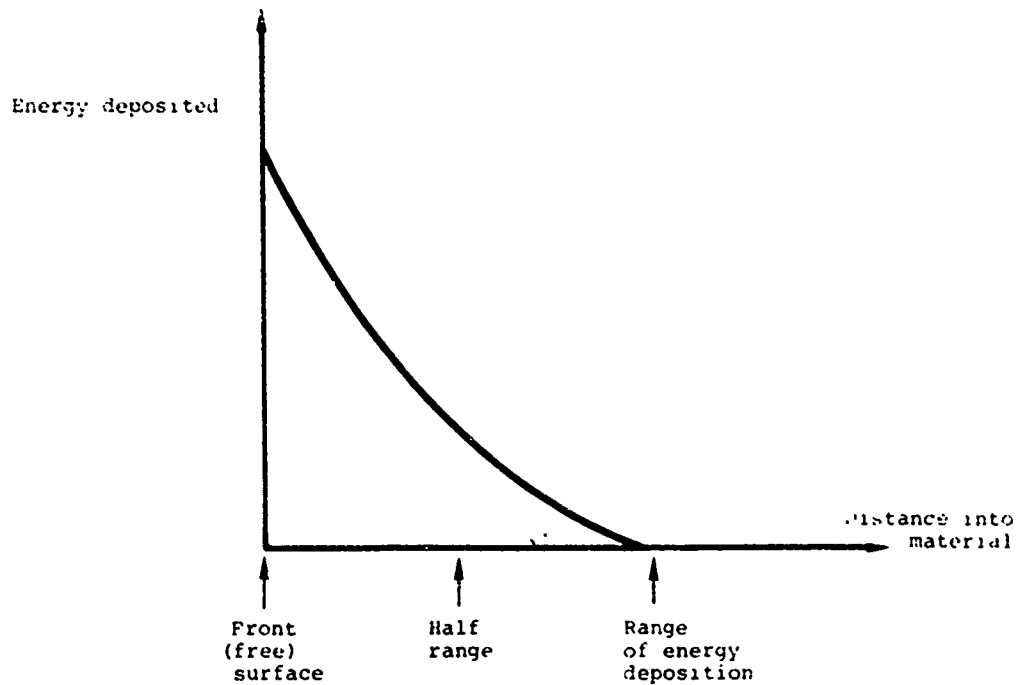
Figure D-2   Energy deposition profile.
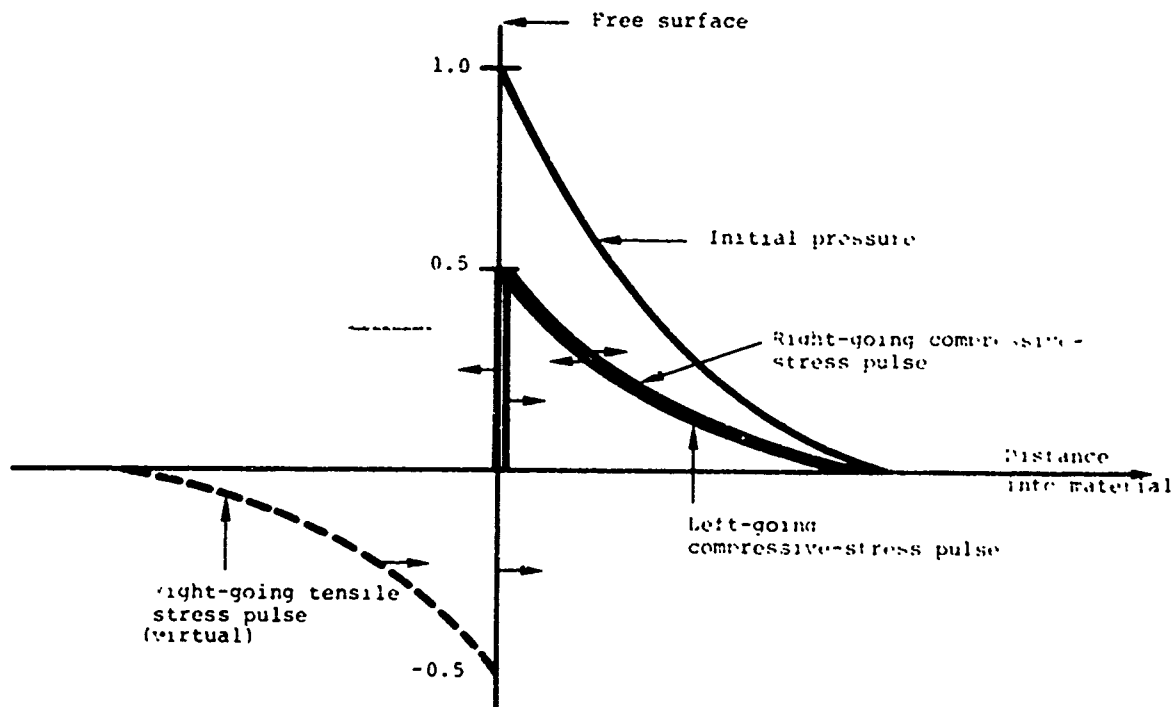
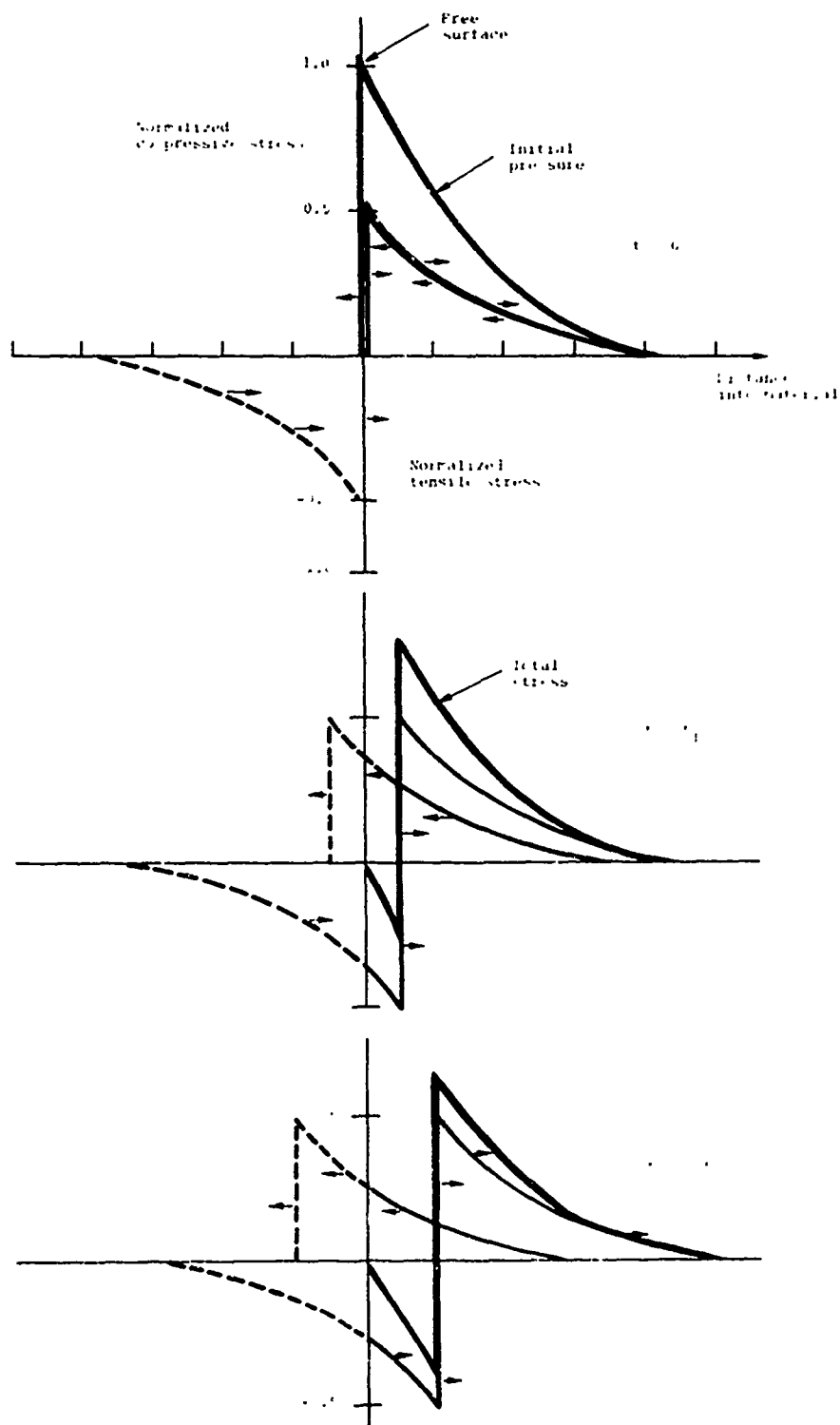Figure D-3   Decomposition of initial pressure into running
waves.

154

Figure D-4a   Development of stress waves produced by sudden energy deposition, without spall.
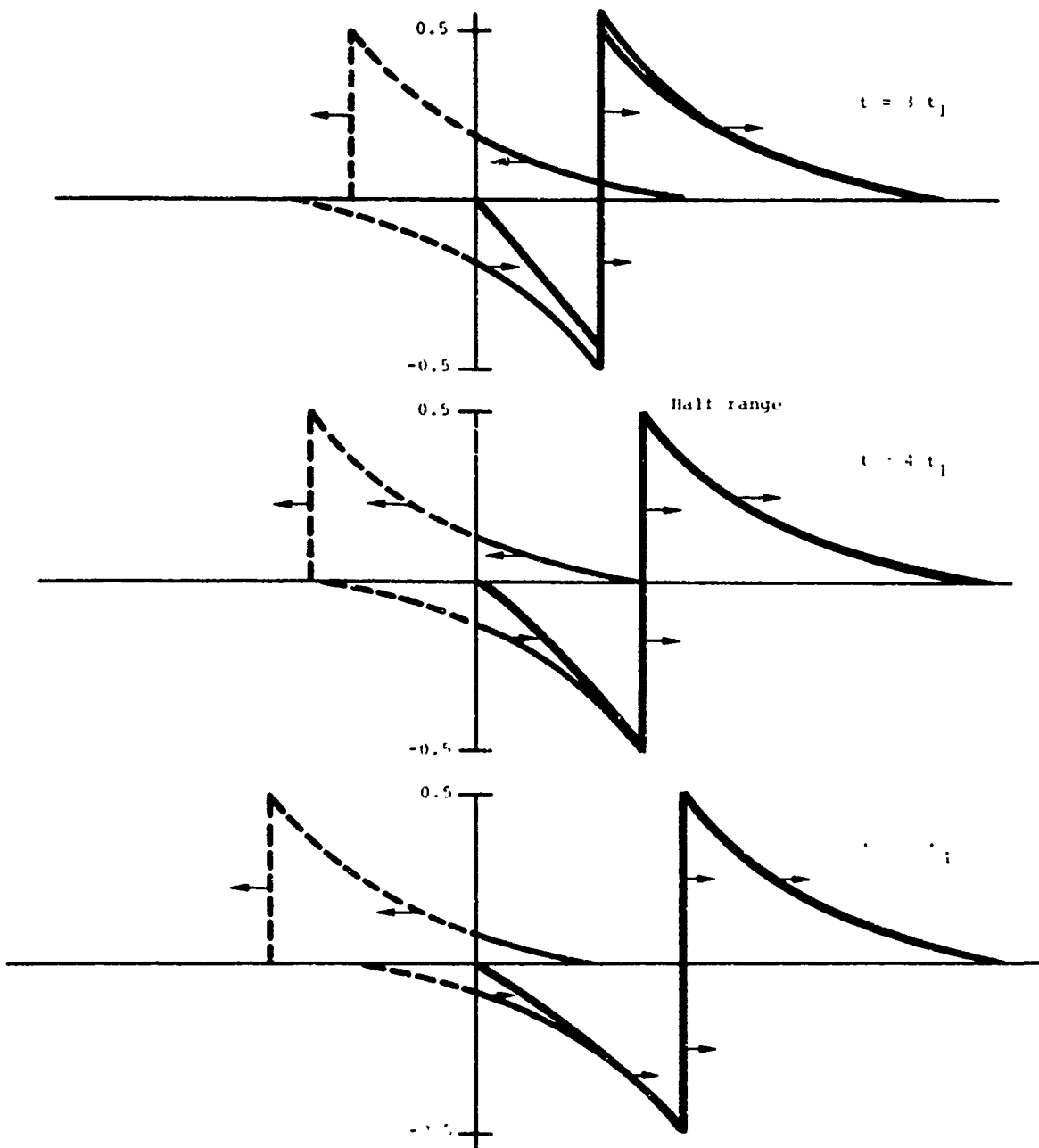
155

Figure D-4b Development of stress waves produced by sudden energy deposition, without spall.

compressive pulse at that point. Thus, the envelope of peak tension is formed as the maximum amplitude of the tensile pulse is superimposed successively with various points along the left-going compressive pulse. Hence, this envelope will have the same shape as the left-going compressive pulse, except that the scale of the abscissa will be reduced in half because the waves are moving toward each other (Figure D-5). Once the leading edge of the tensile pulse has reached the end of the left-going compressive pulse, there can be no further increase in the peak value of the tension. This occurs at the point midway between the front surface and the end of the region of energy deposition, i.e., half-range.

Next, consider the case where the peak tension exceeds the spall strength. For instance, if spall occurs before the tensile stress reaches its maximum value, as shown in Figure D-6, a new free surface is suddenly created,[*] requiring a zero-stress boundary condition. At this point the situation is similar to the initial condition. Additional tension results from reflection of the left-going compressive pulse remaining in the un-spalled material. The envelope of peak tension for this pulse may be constructed as in the first case; the shape of the curve is unaltered from the form obtained when no spall was allowed, except that it is translated upwards by an amount equal to the spall strength (Figure D-7).

If the magnitude of the tensile stress pulse is more than twice the spall strength, multiple spalls will result. The envelope of peak tension can be constructed as before, and the last

----

[*] In reality, solid spall occurs over a period of time and is more complex than the above discussion might imply.
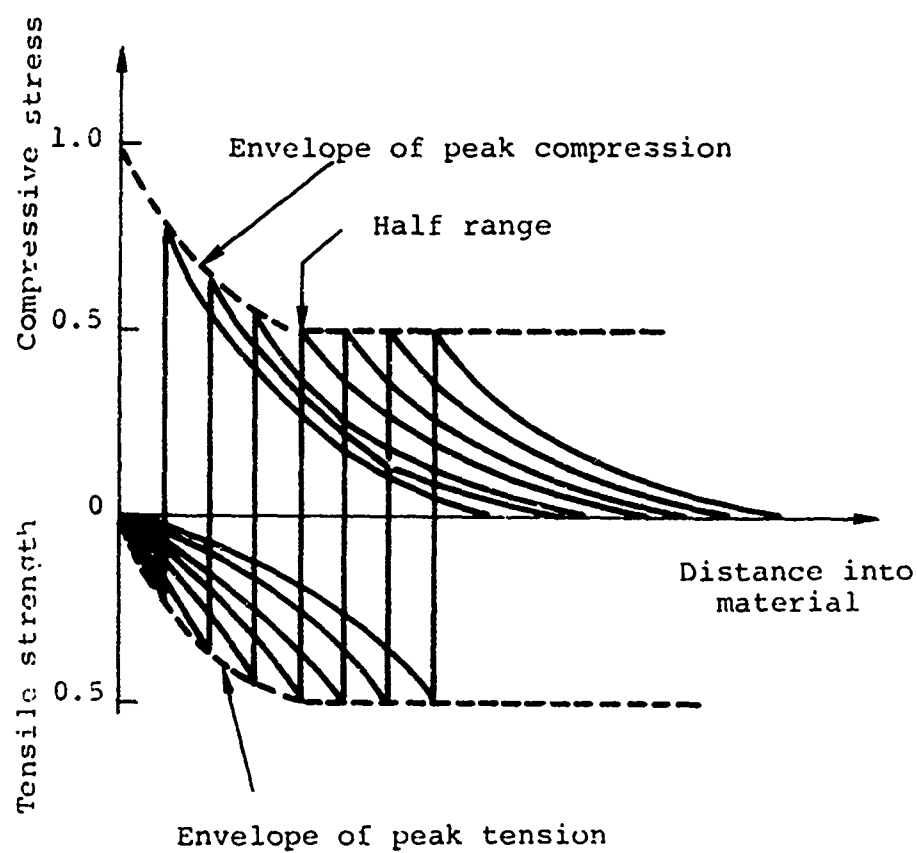
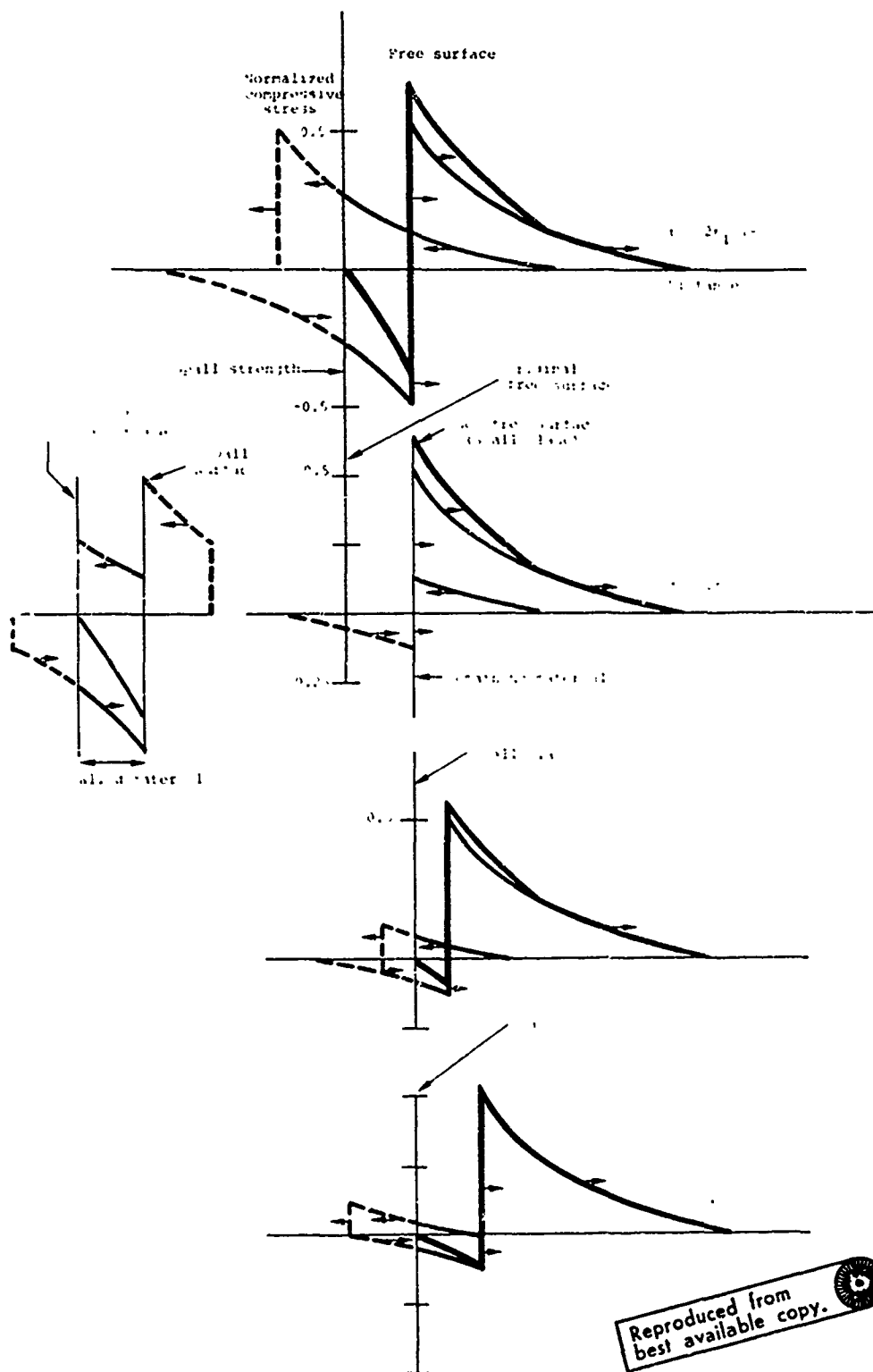Figure D-5 Stress-wave envelopes without spall.

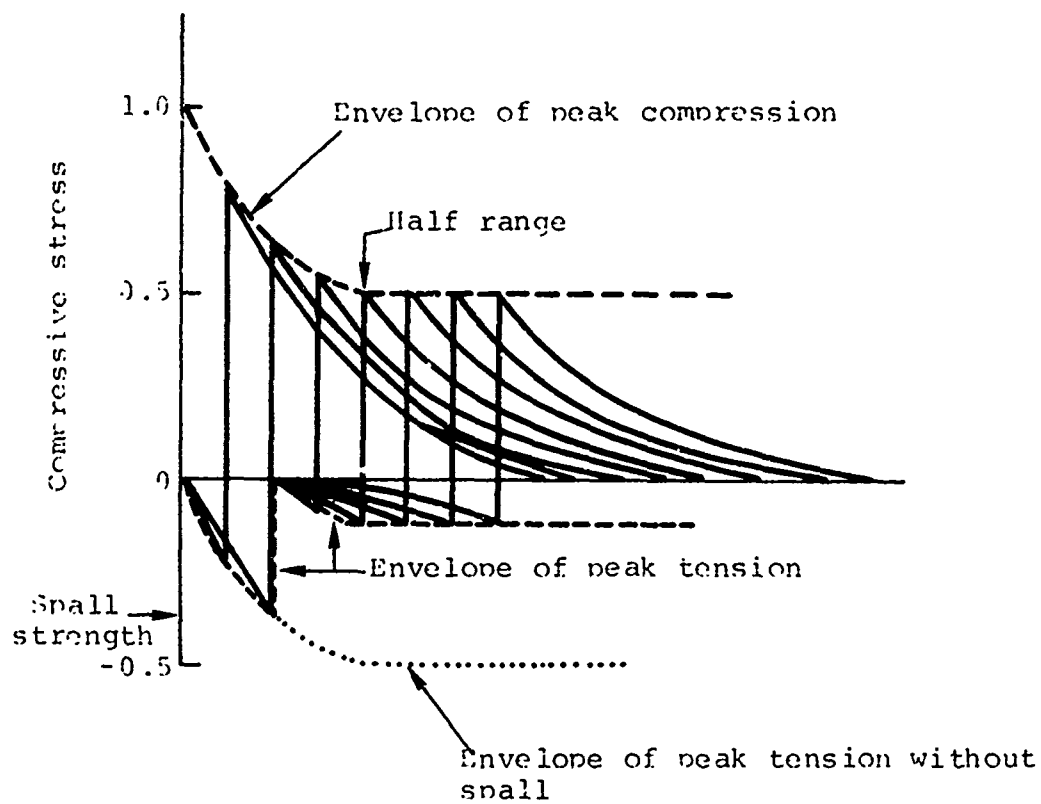Figure D-6   Stress-wave development when spall occurs.

Figure D-7   Stress-wave envelope when spall occurs.

spall occurs when the remaining left-going compressive pulse after reflection is not large enough to exceed the spall strength (Figure D-8). Thus, even if a zero spall strength is assumed, no front-surface spall occurs beyond half range[*] since there is no more left-going compressive stress pulse remaining to reflect and produce tension.

These observations apply specifically to front-surface-spall phenomena. In making comparisons to experimental data, it should be borne in mind that the right-going compressive pulse may reflect off a free rear surface and return to the front surface as a left-going tensile wave. Thus, unless precautions (such as the use of momentum traps) are taken to prevent this complication, additional material loss may occur.

Including a finite source time reduces the amplitude of the peak propagating compressive stress and peak propagating tensile stress but does not change the locations of the maxima.

At this point, an explanation of the appearance of the craters becomes possible. At low electron energies and low fluence, the material loss is due to either solid spall or a combination of liquid spall at the surface and solid spall deeper into the material. In all such cases, the crater depth is less than or equal to the half range of the energy deposition. Since a substantial gradient in temperature is obtained between the front surface and the half range point, the spall strength would increase with increasing depth into the material. Hence, it is

---

[*] In performing computations using finite-difference material-response codes, care must be taken to ensure that computational noise does not cause spall indications when low values for the threshold are used.
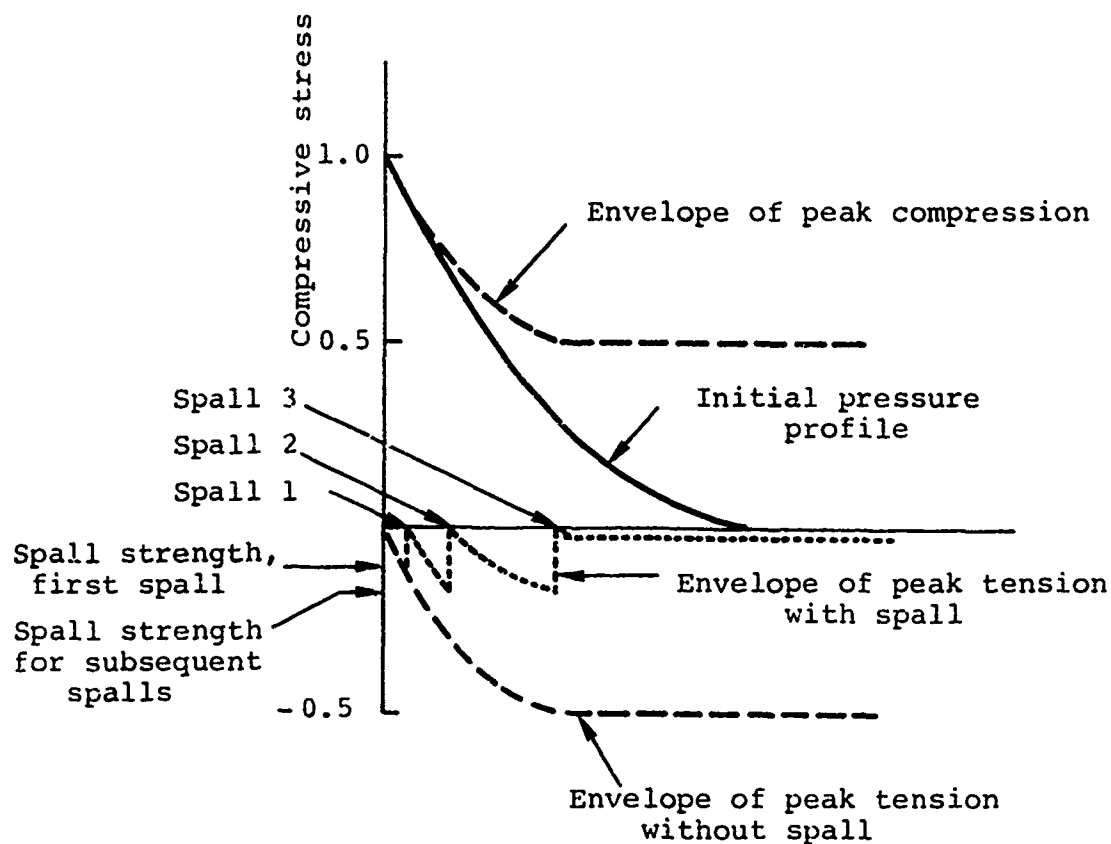
161

Figure D-8   Stress-wave envelope for multiple spall.

not surprising that at low fluences, the spall depths are less than half range, since the material at the half range depth may be able to sustain considerable tension.

As the fluence increases, the solid-partial melt interface moves deeper into the material. As it passes the half range point, liquid spall occurs only up to the half range and melted material is left on the sample.

Further increases in fluence lead to larger thicknesses of melt remaining. The radial flow patterns observed in such cases are the combination of radial stress relief at the edge of the irradiated area and small variations in beam intensity across the diameter of the sample.

When the higher-energy beam was used, melt was not achieved to depths near half range. Hence, the last spall was a solid spall, leaving a clean crater.

The above discussion provides a consistent explanation of the observed effect. The physical phenomena are somewhat different when vaporization occurs. If extensive vaporization is produced at the surface, the high-pressure vapor changes the boundary condition at the liquid-vapor interface. As a result, the tensile pulse may be suppressed, and little or no liquid (or solid) spall will occur.

The situation is more complex when a substantial portion of the irradiated material is in the liquid-vapor mixed phase region. In such cases, it appears that a liquid spall might occur, while a low-pressure vapor remains in front of the spall region, in which case breakup of the liquid spall could allow late-time communication between the vapor and the sample surface.

Finally, it should be noted that the total impulse is comparatively insensitive to the exact quantity of mass removed by liquid spall. The final stages of liquid spall occur in material with low particle velocity so that the impulse associated with this mass is small.
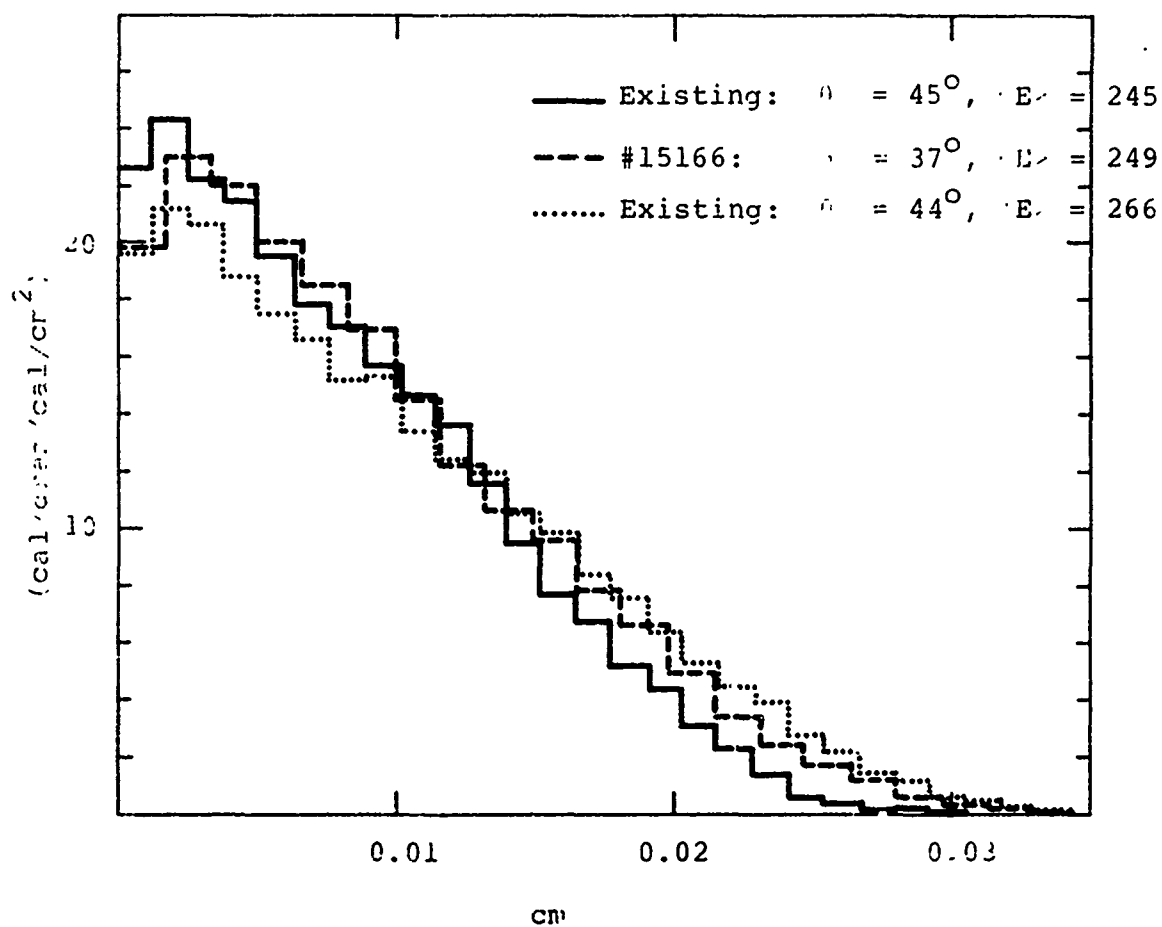
APPENDIX E

ELECTRON DEPOSITION PROFILES IN ALUMINUM
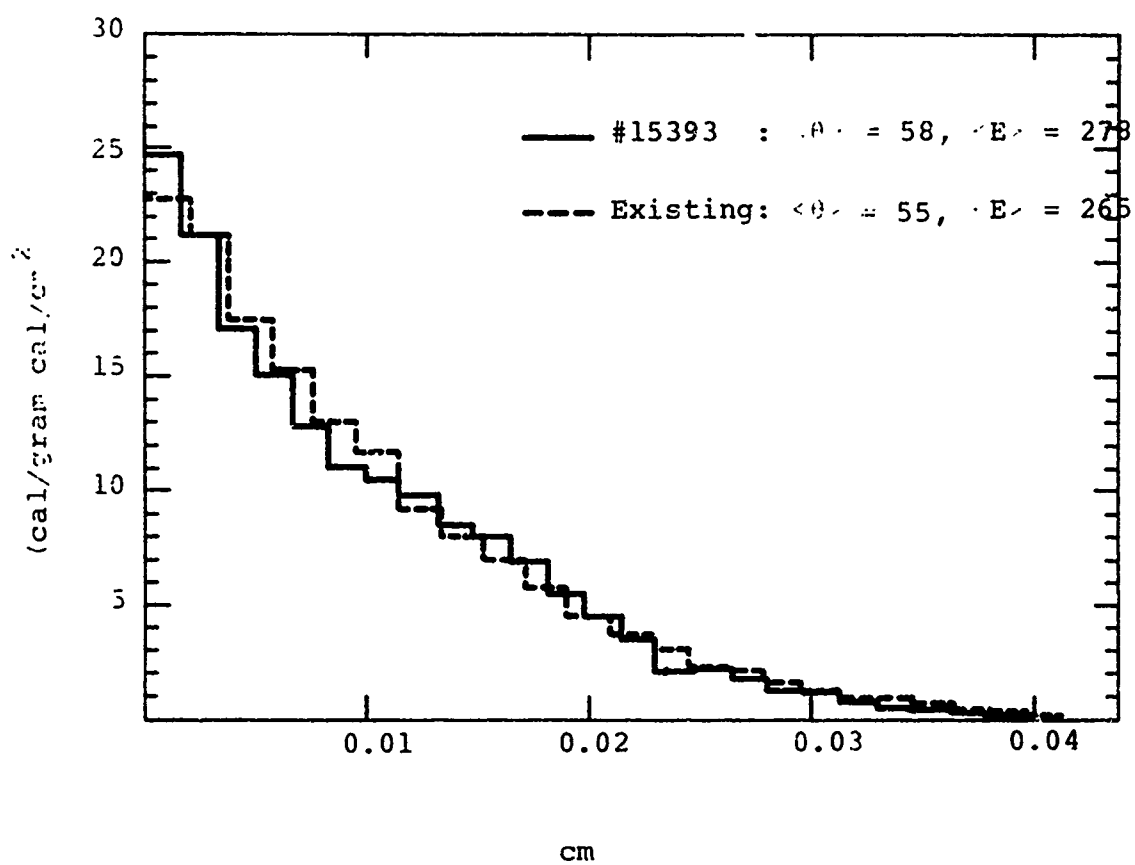
Figure E-1 Normalized deposition profile in aluminum.
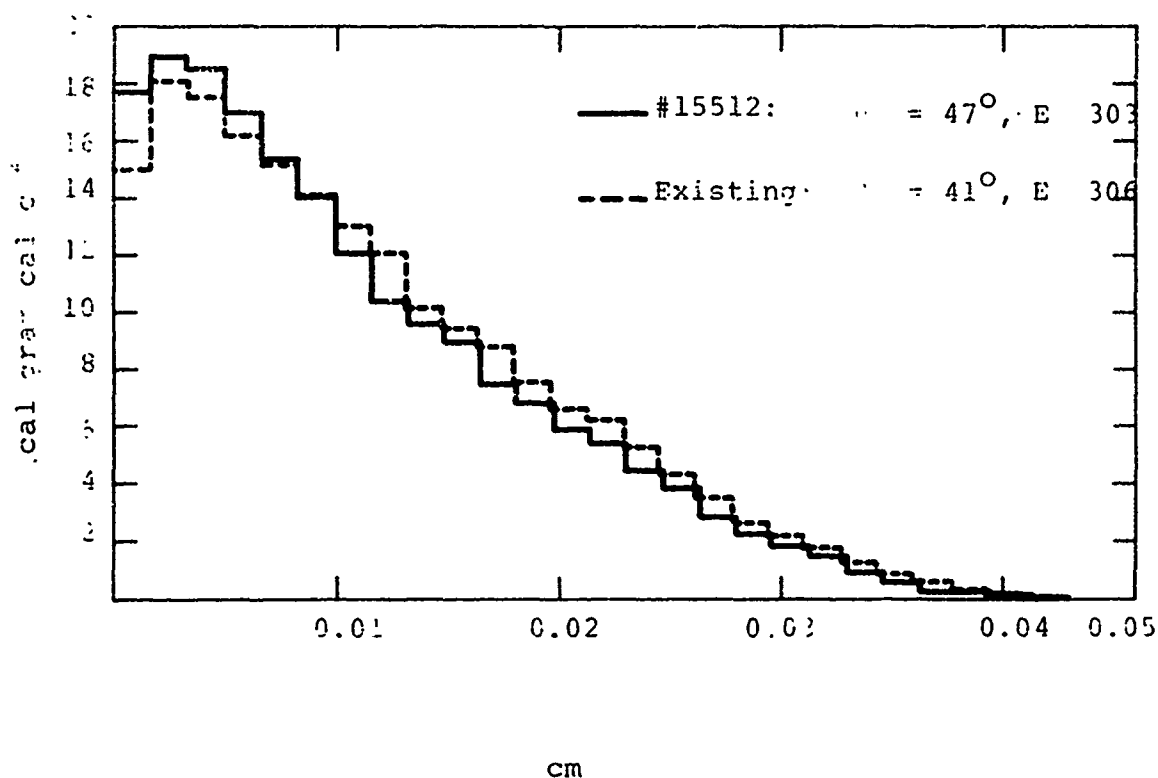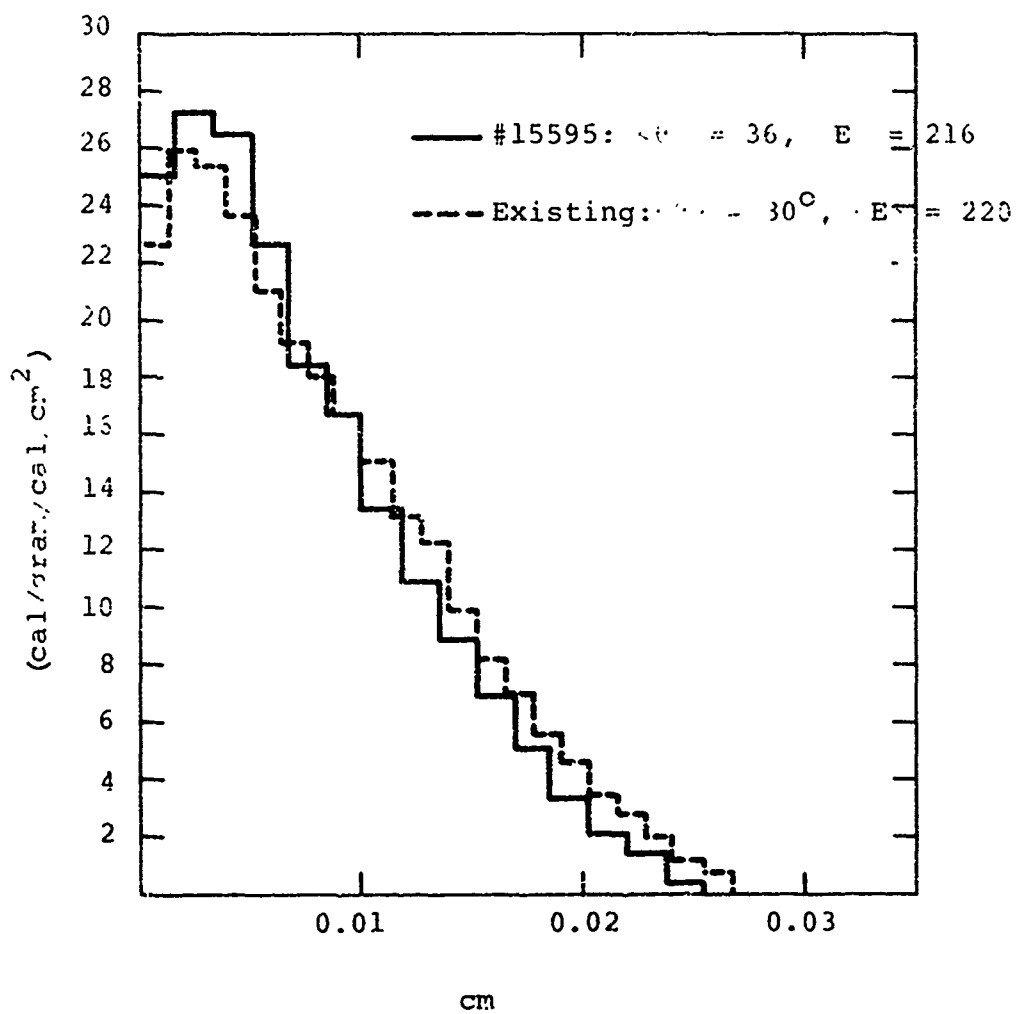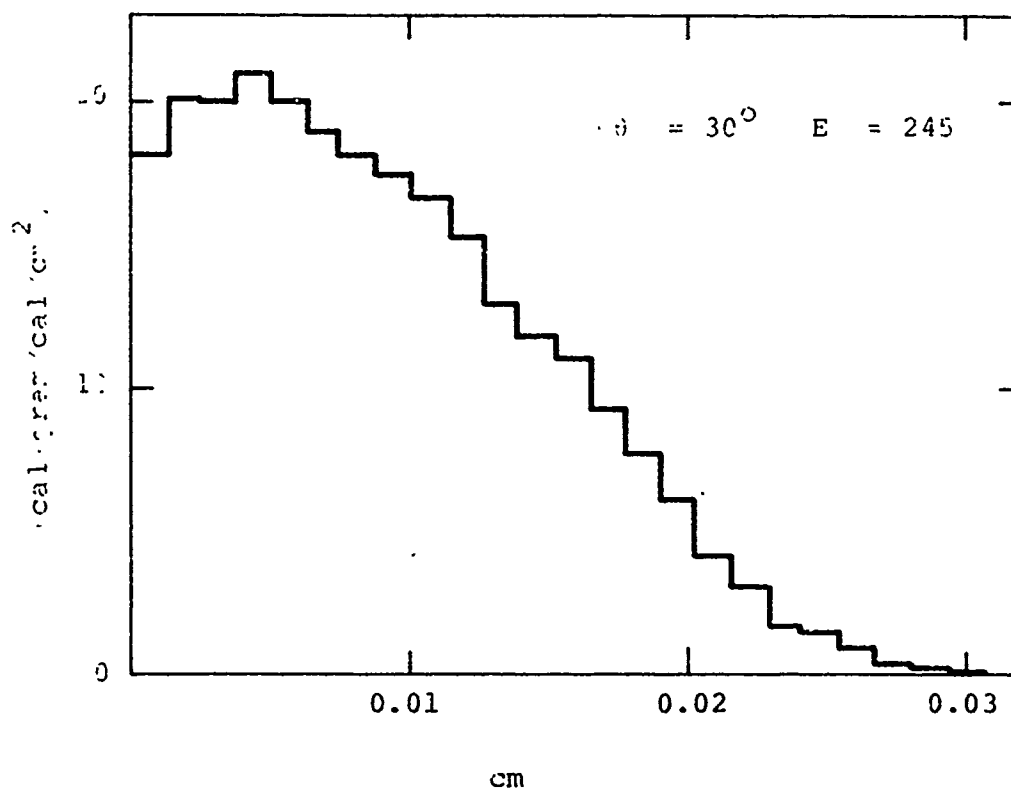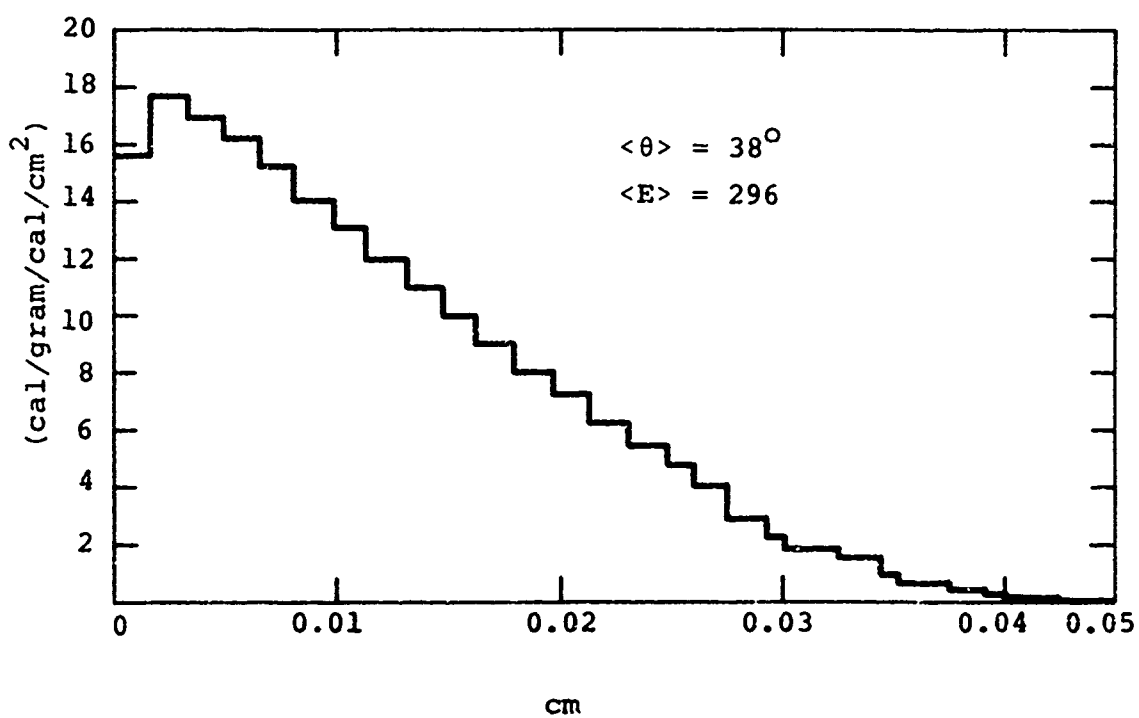
Figure E-2   Normalized deposition profile in aluminum.

Figure E-3 Normalized deposition profile in aluminum.

Figure E-4 Normalized deposition profile in aluminum.

Figure E-5   Normalized deposition profile in aluminum.

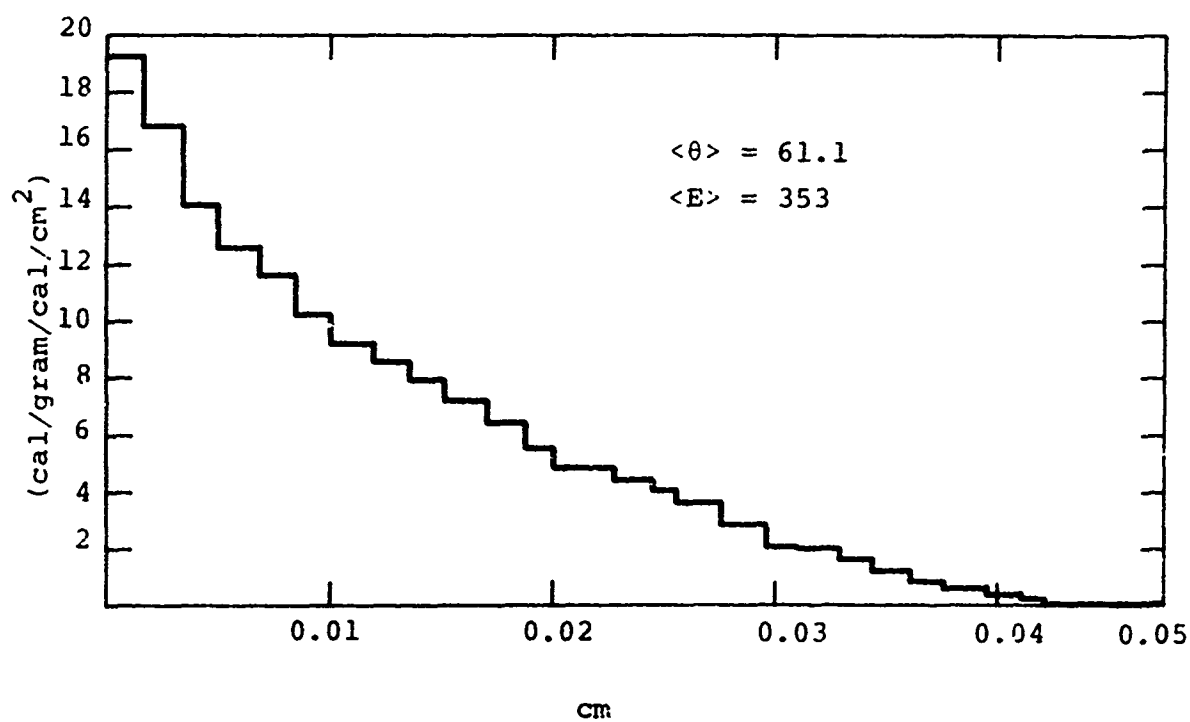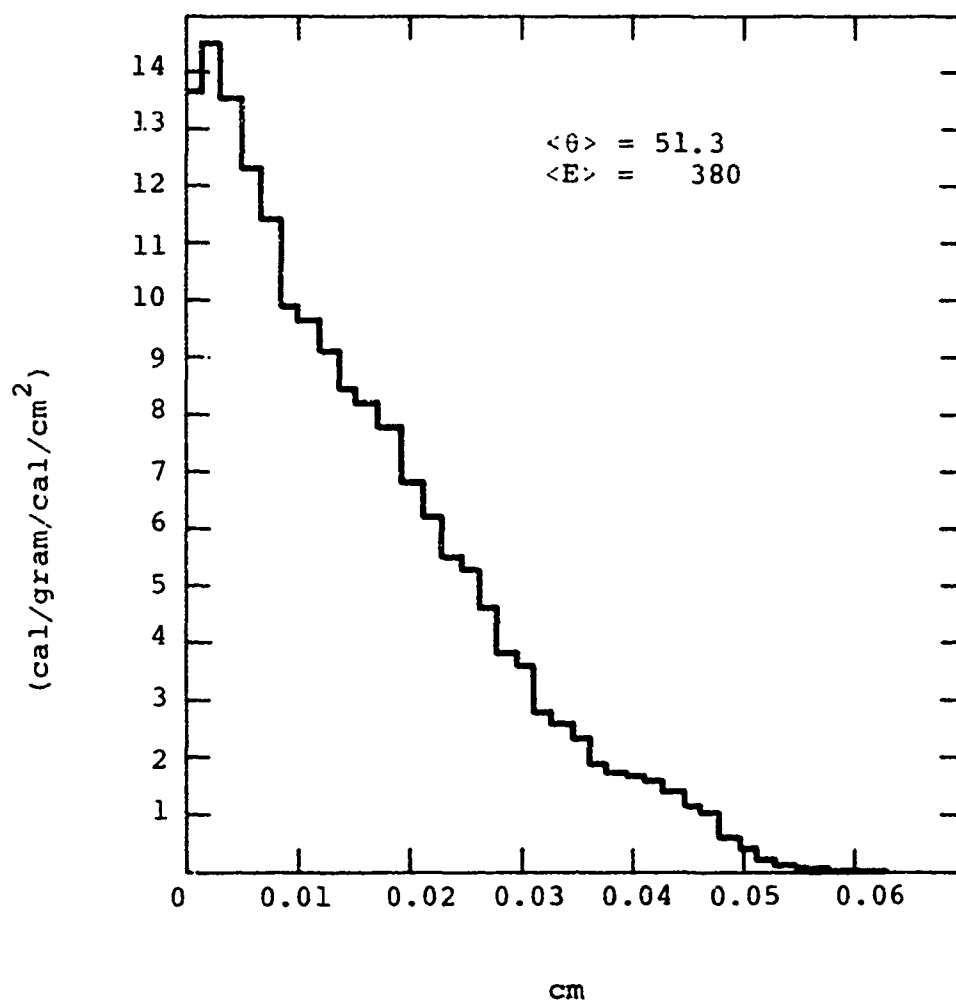Figure E-6   Normalized deposition profile in aluminum.

Figure E-7   Normalized deposition profile in aluminum.

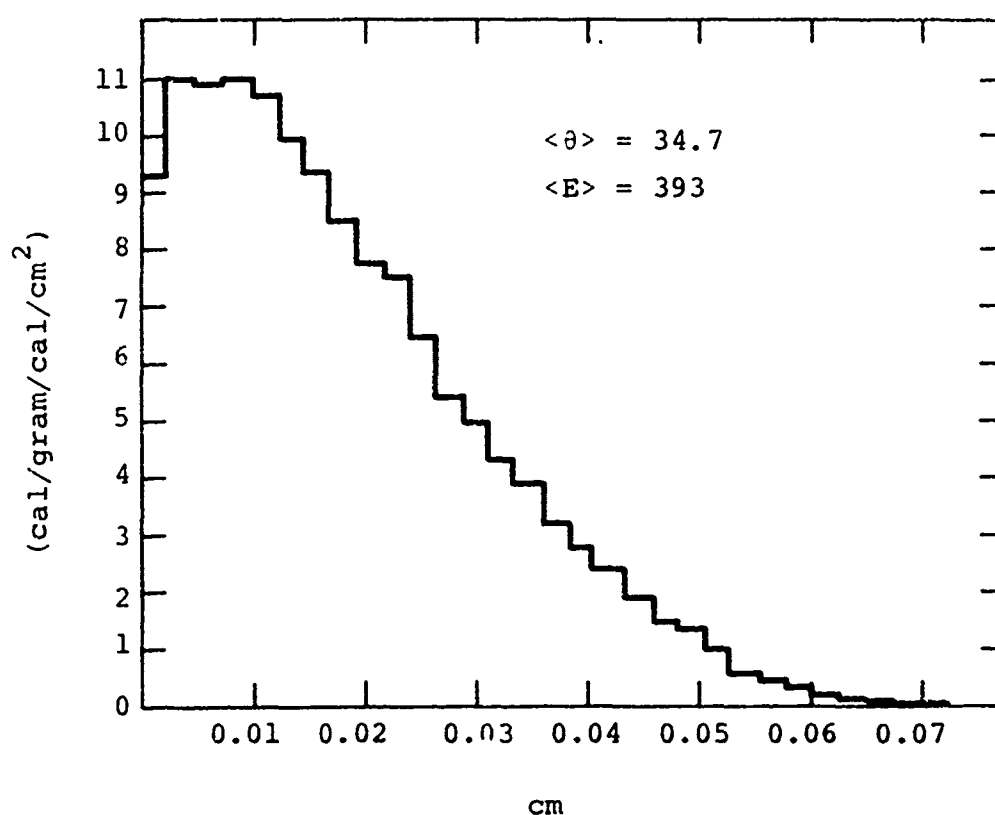Figure E-8   Normalized deposition profile in aluminum.
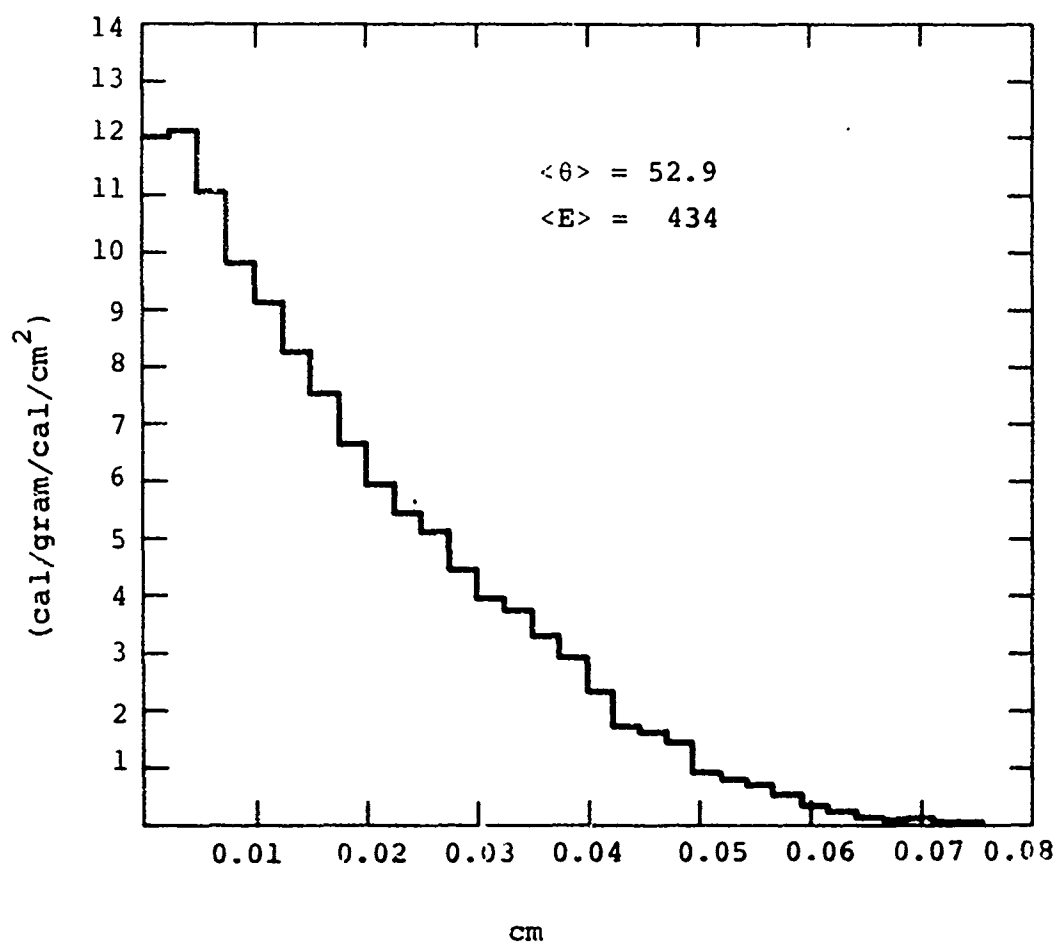
Figure E-9 Normalized deposition profile in aluminum.

Figure E-10 Normalized deposition profile in aluminum.